Mississippi State University

Scholars Junction

1-1-2012

Quantitative Analysis and 3D Visualization of Nwp Data Using Quasi-Geostrophic Equations

Joseph Michael Battalio

Recommended Citation

QUANTITATIVE ANALYSIS AND 3D VISUALIZATION OF NWP DATA USING

QUASI-GEOSTROPHIC EQUATIONS

By

Joseph Michael Battalio

A Master's Thesis
Submitted to the Faculty of
Mississippi State University
in Partial Fulfillment of the Requirements
for the Degree of Master of Science
in Geosciences
in the Department of Geosciences

Mississippi State, Mississippi

May 2012

QUANTITATIVE ANALYSIS AND 3D VISUALIZATION OF NWP DATA USING

QUASI-GEOSTROPHIC EQUATIONS

By

Joseph Michael Battalio

Approved:

_____
Jamie L. Dyer
Associate Professor of Geosciences
(Major Professor)

_____
Philip Amburn
Research Associate Professor
(Committee Member)

_____
Michael E. Brown
Associate Professor of Geosciences
(Committee Member)

_____
P. Grady Dixon
Associate Professor of Geosciences
(Committee Member)

_____
Michael E. Brown
Associate Professor of Geosciences
(Graduate Coordinator)

_____
Gary L. Myers
Professor and Dean
College of Arts & Sciences

Name: Joseph Michael Battalio

Date of Degree: May 12, 2012

Institution: Mississippi State University

Major Field: Geosciences

Major Professor: Dr. Jamie L. Dyer

Title of Study: QUANTITATIVE ANALYSIS AND 3D VISUALIZATION OF NWP
DATA USING QUASI-GEOSTROPHIC EQUATIONS

Pages in Study: 147

Candidate for Degree of Master of Science

Quasi-geostrophic (QG) analysis of the atmosphere utilizes predefined isobaric surfaces to ascertain vertical motion. One equation of the QG system is the omega equation that states that vertical forcing results from differential vorticity advection and thickness advection. Two problems arise when using the QG omega equation: the forcing terms are not independent and must be analyzed simultaneously, and vertical forcing is visually noisy. Both issues are resolved using a smoothing and quantification technique that applies the QG omega equation. The analysis fields from a selection of events were chosen from the North American Mesoscale model. Using a finite differencing methodology dependent on the wavelength of synoptic features, values of vertical forcing were calculated using the omega equation. The calculated omega field correlated well with model omega while also quantifying and visualizing large perturbations in vertical forcing. The method allows for quick diagnosis of forcing type and strength within the atmosphere.

DEDICATION

To my family for always believing in me. I love all of you.

Most importantly I must thank my family, friends, and in particular Rebecca. I would not be the young, humble scientist today if not for them believing in me and for their willingness to knock me down a peg or two when I get too cocky.

TABLE OF CONTENTS

LIST OF TABLES

LIST OF FIGURES

LIST OF SYMBOLS

a radius of the Earth (m)

f coriolis

f_0 Coriolis parameter = 1.0×10^{-4}

g gravitational acceleration (ms^{-2})

P pressure (Pascal)

q quasi-geostrophic potential vorticity (s^{-1})

R universal gas constant

s the offset between grid cells

t time (s)

T temperature (K)

z absolute vorticity (s^{-1})

α specific volume = ρ^{-1}

β Beta-plane approximation = $2\Omega cos\phi/a$

Δ distance between grid cells in the NAM (m)

χ geopotential tendency (gMs^{-1})

ϕ latitude (degrees)

Φ geopotential height (gM)

σ static stability parameter

θ potential temperature (K)

ω vertical wind (Pas^{-1})

ζ relative vorticity (s^{-1})

$\vec{V_g}$ Geostrophic Wind (ms^{-1})

∇ del operator = $(\frac{\partial}{\partial_x}, \frac{\partial}{\partial_y})$

CHAPTER 1

INTRODUCTION

Meteorologists have relied upon quasi-geostrophic (QG) equations to diagnose and forecast for decades, beginning with Charney [11], continuing with Charney and Stern [13], then to Phillips [34], and progressing to Pedlosky's [33] description of the equations that are presently cited. Quasi-geostrophic theory uses the primitive equations of meteorology and replaces horizontal velocity and acceleration values for winds by geostrophic counterparts, where geostrophic winds are those caused by the balance of the horizontal Coriolis force and the pressure gradient force [11]. Additionally, QG theory uses the hydrostatic approximation (that gravity is balanced by the vertical pressure gradient force) to describe the static stability parameter [41].

The necessity of computation methods is demanded by the fact that vertical motion is many orders of magnitude smaller than horizontal motion on the synoptic scale, and, as there are relatively few sounding sites across the country, there is a lack of upper-level observations to directly measure vertical motion. Numerical atmospheric analysis instead uses a set of mathematical and physics based equations to calculate the vertical motion using easily measured variables. The primary reason QG theory is used is that QG theory yields similar values for the diagnosis of synoptic-scale vertical motion while being much simpler than the primitive equations of meteorology [9] [4]. QG theory primarily

1

uses two variables to determine vertical motion, the advection of temperature, as a proxy for atmospheric thickness, and vorticity, a quantification of the rotation of a fluid [46]. Simplistically, the advection of warm air and the advection of positive (cyclonicly spinning or counterclockwise spinning) vorticity lead to rising air while the advection of cold air and negative vorticity lead to sinking air. Consequently, upward vertical motion in the atmosphere is caused by increasing positive vorticity advection with height and warm air advection at the lower levels [50].

However, as a result of the simplification of the primitive equations, QG theory introduces several assumptions on the nature of the atmosphere that cause mesoscale noise in the model fields that limit the ability to properly diagnose atmospheric motions. This study aims to reduce the small scale noise and remove several assumptions in QG theory by independently calculating the QG system of equations on a set of model data and then using three-dimensional visualization methods to conceptualize terms of the QG omega and QG geopotential tendency equations.

A brief overview of QG theory is presented followed by the enumeration of several assumptions inherent in QG theory then the description of a method of calculating and visualizing the omega and geopotential tendency equations to achieve dynamical smoothing of the vertical motion field.

1.1   Quasi-Geostrophic Theory

The geostrophic approximation was first made by R. C. Sutcliffe in 1939 [45]. Sutcliffe determined that since a geostrophic wind has no divergence, it must be the ageostrophic

component of the wind that causes the development of cyclones. Sutcliffe was also the first to determine the pattern of generation of cyclonic vorticity and rising air ahead of a trough and anticyclonic vorticity and sinking motion behind the trough.

In 1947 Sutcliffe [46] produced his famous theory of development. In that theory he derived an equation for the difference in horizontal divergence at two levels, which in turn describes vertical motion. Following Sutcliffe's theory, Charney [11] and Eady [17] first developed the theory of cyclogenesis where the creation of circulations is a result of harmonic waves caused by baroclinic instability.

Quasi-geostrophic theory was first introduced as it is known today by Charney [12] and independently by Eliassen [18]. Charney introduced the geostrophic approximation into the potential vorticity and potential temperature equations. Using isobaric coordinates, this yielded an expression for the continuity equation, eq. 1.1 and the thermodynamic energy equation, eq. 1.2. These equations are the basis of QG theory.

$$\nabla^2 \left(\frac{\partial \Phi}{\partial t} \right) - f^2 \left(\frac{\partial \omega}{\partial p} \right) = -\nabla \cdot \left(\vec{V_g} \cdot \nabla \nabla \Phi \right) - f\beta \vec{V_g} \tag{1.1}$$

$$\frac{\partial}{\partial p}\frac{\partial \Phi}{\partial t} - \frac{\alpha}{\theta}\frac{\partial \theta}{\partial p}\omega = \vec{V_g} \cdot \nabla \alpha \tag{1.2}$$

Mathematically, quasi-geostrophic theory is a system of two equations: the quasi-geostrophic potential vorticity equation and the omega equation. These two equations form the foundation of diagnosis and forecasting that occur within numerical models. Forms of these equations will be used in this study to quantify the vertical motion fields using three-dimensional visualization methods, thus a brief historical overview and qualitative description of each follows.

1.2 Potential Vorticity

Circulation was recognized as a prime factor in the development of atmospheric processes ever since Bjerknes. It was Rossby [40] that first determined that the vertical component of absolute vorticity $z = f + \vec{k}(\nabla \times v)$ is the most important to atmospheric flow. A year later Rossby [41] first described the concept of potential vorticity. He noted that if h is the depth of a fluid column then $z/h = constant$. Vorticity must be conserved, and thus can only be horizontally advected. However, potential vorticity can be affected by stretching the atmospheric column. Once this revelation was reached, potential vorticity maps gained adoption as a diagnostic tool. Reed and Sanders [36] began analyzing the structure of potential vorticity features, while computer generated maps were first made by Obukhov [30].

Charney and Stearn [13] further defined the quasi-geostrophic potential vorticity, denoted as q, through the use of the invertability principle. In pressure coordinates it can be written as:

$$q = f + \vec{k}\nabla_p \times \vec{v} + f_0 \frac{\partial}{\partial p}\left(\frac{\theta'}{\frac{d\theta_{ref}}{dp}}\right) \tag{1.3}$$

where θ_{ref} is a reference potential temperature function, θ' is the deviation from the reference, and f_0 is the value of the Coriolis parameter. Charney and Stearn [13] further defined the streamfunction

$$\Psi' = f_0^{-1}[\phi - \phi_{ref}(p)] \tag{1.4}$$

where ϕ_{ref} is a reference geopotential. Thus if q is known then the stream function can be calculated. Equation 1.3 is the QG form of the potential vorticity conservation equation.

It was Hoskins [25] that solidified the use of potential vorticity as a forecast tool; Hoskins affirmed two principles involving the use of potential vorticity. The first is that potential vorticity and potential temperature are conserved when compared to advection if friction and diabatic process are negligible. The second is the invertibility principle which states that if the mass beneath each isentropic surface is known, then a known potential vorticity field is sufficient to diagnose all other dynamic variables. For these reasons, potential vorticity is great importance to atmospheric analysis.

1.3 Geopotential Tendency

The potential vorticity is closely related to the geopotential tendency, $\chi = \frac{\partial \Phi}{\partial t}$, and Potential vorticity can be considered the conserved quantity in the geopotential vorticity equation. Rearranging the potential vorticity equation, equation 1.3, yields an expression for geopotential tendency.

$$\underbrace{\left[\left(\nabla^2 + \frac{\partial}{\partial p} \quad \frac{f_0^2}{\sigma} \frac{\partial}{\partial p}\right)\right] \chi}_{A} = \underbrace{-f_0 \vec{V_g} \cdot \nabla \quad \frac{1}{f_0} \nabla^2 \Phi + f}_{B} - \underbrace{\frac{\partial}{\partial p}\left[\left(\frac{f_0^2}{\sigma} \vec{V_g} \cdot \nabla \quad -\frac{\partial \Phi}{\partial p}\right)\right]}_{C} \tag{1.5}$$

where Φ is the geopotential height, $\vec{V}$ is the geostrophic wind, σ is the static stability parameter, and f_0 is the Coriolis parameter. Here the left-hand-side of the equation is the local geopotential tendency term, and the right-hand-side of the equation constitutes the forcing functions that influence the geopotential tendency. Term B describes the contribution of vorticity advection to height changes and is the strongest term above 500 hPa. Term C describes the advection of thickness and is the dominant term for forcing below 500 hPa [43]. Assuming Φ is known, the RHS can be easily computed using the meth-

5

ods described in this paper. As term A contains terms with second spacial derivates, it is common practice to to qualitatively consider those terms proportional to minus χ [21] (see section 1.4 for additional explanation).

Since its development, geopotential tendency has been used in model diagnostics. Jusem [27] used height tendency to evaluate the performance of a primitive equation pressure tendency numerical model and complement potential vorticity diagnostic methods. Several case studies over South America were performed, and it was found that upper-tropospheric warm air advection played an important role in the development of mid-latitude depressions.

Geopotential tendency uses the combination of vorticity advection and thickness advection to describe the change of heights over time. Another method of using vorticity and thickness advection to diagnose atmospheric states using QG theory is by employing the omega equation.

1.4 Omega Equation

The second major component of QG theory is that of the analysis of vertical motion. The development theory of Sutcliffe [45],[46] first described the components of the omega equation [23]. Operational analysis of the omega theory began in earnest in the 1960s [14]. It was found that omega, when applied to individual isobaric levels and under certain assumptions of horizontal levels of non-divergence, could reliably predict mid-tropospheric

development. The operational use of the omega equation followed from an interpretation given by Trenberth [50]. Trenberth stated the omega equation as

$$\underbrace{\left[\sigma\nabla^2 + f_0^2\frac{\partial^2}{\partial p^2}\right]\omega}_{A} = \underbrace{\left[f_0\frac{\partial}{\partial p}\vec{V_\Psi}\cdot\nabla(\zeta+f)\right]}_{B} - \underbrace{\left[f_0\nabla^2\ \ \vec{V_\Psi}\cdot\nabla\frac{\partial\Psi}{\partial p}\right]}_{C} \quad (1.6)$$

where ω is the vertical velocity, ψ is the geopotential height, σ is the static stability, ζ is the relative vorticity, p is the pressure, and f_0 is the Coriolis parameter. The left hand side of the equation is similar to the left-hand-side of the geopotential tendency equation, 1.5 and is treated using a similar method. Assuming that ω is sinusoidal in the vertical and horizontal $\omega = C\sin\pi p/p_0\sin kx\sin ly$, then the Laplacian operator, term A of the equation, can be treated as a negative coefficient as

$$\left[\sigma\nabla^2 + f_0^2\frac{\partial^2}{\partial p^2}\right]\omega \approx -\left[k^2 + l^2 + \frac{1}{\sigma}\left(\frac{f_0\pi}{p_0}\right)^2\right]\omega \quad (1.7)$$

thus term A is proportional to $-\omega$. The right-hand-side consists of two parts. Term B is the vertical derivative of absolute vorticity advection. Upward motion occurs where cyclonic vorticity advection increases with height. Term C is the Laplacian of temperature advection. Upward motion occurs in areas of warm air advection.

Qualitatively, the advection of warmer air is associated with upward vertical motion, and the advection of cold air is associated with downward vertical motion. As QG theory assumes that the atmosphere is in hydrostatic equilibrium, that the vertical atmospheric pressure gradient is balanced with gravity, lines of constant temperature align with contours of constant geopotential height. It is the changes in thickness that effect vertical motion. As an area of warm air is advected to an area of cold air, upper level thickness increases and ridges are strengthened due to thermal expansion of the atmospheric

7

column. Consequently, upper level divergence must occur to reduce heights to maintain equilibrium, and air from below must rise to fill in the vacuum. Conversely, as cold air is advected, upper level thickness decreases, and upper level convergence occurs to fill in the shorter column [47].

A physical interpretation of the effect of vorticity advection is as follows: Consider a column of air being advected through an area of positive vorticity. As the parcel exits the area of vorticity, environmental values of vorticity decrease. Conservation of angular momentum demands that the column of air expand to reduce the values of vorticity to match the environment. In the mid-latitudes, winds increase with height, so the column of air has a lower value of positive vorticity advection at the surface than in upper levels. If the mean wind motion is subtracted from the column, the motion of the column is such that the surface experiences negative vorticity advection and hence convergence, and the upper levels experience positive vorticity advection and divergence [52]. Surface convergence and upper level divergence lead to vertical motion following Dines compensation [15]. As vorticity advection plays a large role in the change of the height of a layer, vorticity advection is a major component of both the geopotential tendency equation and the omega equation.

One technique to analyze the omega equation is the Q-vector method [24], where

$$\vec{Q} = (Q_1, Q_2) = \left(- \left[\frac{g}{\theta_0} \frac{\partial \vec{V_g}}{\partial x} \right] \nabla \theta, - \left[\frac{g}{\theta_0} \frac{\partial \vec{V_g}}{\partial y} \right] \nabla \theta \right) \tag{1.8}$$

The Q-vector is a construct proportional to the horizontal shear of the geostrophic wind and the horizontal temperature advection for a given static stability and pressure. The vertical

velocity is forced only by the divergence of the vector, $\vec{Q}$. Hoskins [26] demonstrated the use of Q-vectors fields in forecast charts.

A method of combining the analysis of the omega equation with that of potential vorticity has been the subject of work during the last decade. Vertical velocity is now considered to be determined by a combination of potential vorticity tendency, which is determined by potential vorticity advection and by diabatic heating, and by thermal advection [22]. Further theoretical work into QG theory resides in the increasing order approximations of the Rosby number [31].

These two equations, the geopotential tendency equation, eq. 1.5, and the omega equation, eq. 1.6, provide the quantitative diagnostic tools used in numerical weather prediction and have been employed mostly successfully for the previous four decades. Operationally, though, these equations are not calculated by each individual forecaster. Instead, numerical models use these equations to produce isobaric maps, and it is up to the forecasters to interpret those maps.

1.5   Static Stability

Of importance to the thermodynamics of QG theory is static stability, denoted σ in the QG omega and QG geopotential tendency equations. Static stability describes the thermodynamic tendency of a parcel − the potential of a fluid parcel at rest to become laminar or turbulent due to buoyancy. A parcel may be in one of three states, statically unstable, statically stable, or statically neutral. When a parcel is said to be statically unstable, it tends to become or remain turbulent. A statically stable parcel will become or remain laminar.

A parcel that does not tend to either laminar or turbulent flow but remains in its current state is a statically neutral parcel. Turbulence acts to reduce the instability that caused it and will tend to naturally decay with time as any instability is removed; however, outside forcing factors, such as diabatic heating, can continually destabilize the air [44]. Static stability is defined as:

$$\sigma = -\frac{RT}{P}\frac{d(ln\theta_0)}{dP} \tag{1.9}$$

Where R is the gas constant, T is the parcel temperature, P is the parcel pressure, and θ_0 is the potential temperature of the parcel.

As the stability of a parcel greatly depends on diabatic heating, which is a microscale phenomena, thermodynamic processes are also small scale. As static stability is the sole thermodynamic parameter in the QG equations and is of the same order of magnitude as the vorticity and thickness advection terms within the QG omega and geopotential tendency equations, the distribution of static stability can greatly influence the weight of vorticity and thickness advection terms. It is these small scale processes which contribute to the noisy nature of vertical velocity data.

1.6   Divergence and Convergence

Inherent in QG theory and in all fluid dynamics is the concept of fluid divergence. Assuming that the atmosphere is a compressed fluid, equilibrium of heights and pressure can only be achieved through the movement of mass. Following from the PV and omega equations, changes in thickness, pressure, and circulation affect the amount of mass in the

atmospheric column. The hydrostatic approximation dictates that atmospheric pressures be in balance with gravity according to:

$$\frac{\partial \Phi}{\partial p} = -\frac{RT}{p} \qquad (1.10)$$

Convergence and divergence in horizontal synoptic-scale flow is necessary to maintain balance between gravity and the vertical pressure gradient force. A corollary of those theories is that an occurrence of a process that causes divergence or convergence in one area of the atmosphere affects surrounding areas and is generally referred to as Dines' compensation. The effects of divergence and convergence are non-local in that the movement of air in one area forces the movement of air in another due to the incompressibility of the atmosphere and the hydrostatic approximation. Dines' compensation describes the simplest vertical motion profile the atmosphere may have, the bowstring profile [6]. In the bowstring profile, the sign of divergence changes once, so there must be either convergence aloft and divergence at the surface when air is descending (when $\omega < 0$) or visa versa. As air diverges (converges) at the top of the atmosphere, convergence (divergence) occurs at the surface. Understanding the processes that are affected by divergence and convergence yield an understanding of the patterns of synoptic-scale vertical motion.

Divergence can verify the placement of vertical motion because divergence is the cause of synoptic scale vertical motion. The factors that drive vertical motion, thickness advection and differential vorticity advection, do so not because they directly cause vertical motion but because they create areas of divergence. It is the divergence and convergence

11

of the atmosphere that cause vertical motion [51]. So where there are areas of synoptic scale vertical motion, there must also be areas of divergence.

1.7 Operational Use of Quasi-Geostrophic Theory

Operationally, QG theory directs forecasters to several levels in the atmosphere to diagnose trough and ridge patterns and forecast the development of systems within those patterns. Specifically, forecasters look to 850 hPa warm/cold air advection, 500 hPa vorticity advection, and 200-300 hPa jet streaks. Once the areas of ascent and decent have been determined for each level, the forecaster will mentally stack the areas from each level to search for regions where all areas that suggest uplift align.

At the 850 hPa level thickness advection is the primary concern. To view thickness, temperature is used as a proxy under the assumption that an ideal gas expands when heated. A solenoid method is employed to determine where the highest levels of advection occur. In the solenoid method lines of temperature and height are overlaid on a single map. Where the lines cross, solenoids are formed. Smaller solenoids denote stronger advection. Warm air advection is associated with rising air, and cold air advection is associated with sinking air.

Vorticity is viewed at the 500 hPa level due to the assumption of the 500 hPa level as the level of non-divergence (see section 1.8). At this level, vorticity can neither be created nor destroyed and can only be advected. Employing the solenoid method again, areas of high vorticity advection are identified. Positive (cyclonic) vorticity advection is linked with rising air, and negative (anti-cyclonic) advection is linked with sinking air.

In the upper levels the movement of mass holds sway. The jet stream is responsible for the transport of mass, and within the jet stream, jet streaks are enhancements of mass advection. Jet streaks are analyzed by quadranting along the tangential axis and the normal axis. The right rear and left front regions of the jet are linked with upper level divergence and thus rising air, and the left rear and right front regions are linked with upper level convergence and thus sinking air.

Low-level thickness, mid-level vorticity, and upper-level mass advections are the primary dynamic factors in the operational diagnosis of atmospheric motions using QG theory. It is generally left up to individual forecasters to determine which factor or combination of factors is most important in any given situation. Additionally, when diagnosing strengthening storm systems, the lack of one factor may be made up for by the strength of one of the other factors. Only by separately visualizing each individual term can a forecaster discern the the overall forcing pattern. Determining the overall strength of synoptic scale forcing is left to the discretion of individual forecasters.

Despite the success forecasters have with QG theory, issues remain with the implementation of the omega and geopotential tendency equations.

1.8   Issues with QG theory

Quasi-Geostrophic dynamics, in combining vorticity advection and thickness advection, makes several assumptions as to the nature of the atmosphere that are not always correct [35]. QG theory has issues that mainly stem from the inability of QG theory to interpret 3D data. One assumption, arising from the bowstring model, is that the 500 hPa

level is the level of non-divergence. The assumption arises due to the 500 hPa level having equal amounts of mass above and below, so no air should collect along the level; i.e. as the 500 hPa level is the mid-point of the atmosphere with respect to mass, it is where the sign of divergence changes. However, though the 500 hPa level could be at the level of non-divergence, they are not always collocated. The level of non-divergence can only be described as being somewhere in the middle troposphere [54]. Part of the reason that 500 hPa is assumed to be the level of non-divergence is that there is no way to determine the real level of non-divergence because of a lack of three-dimensional diagnostic techniques.

A second assumption arises from the inability to locate the level of nondivergence. Although three-dimensional spatial analysis is implied when considering vorticity advection with height, QG analysis relies solely on the 500 hPa level (as the assumed level of non-divergence) to diagnose areas of vorticity advection. An analysis of the vorticity equation, equation 1.11 provides the reason for such a limited diagnosis.

$$
\underbrace{\frac{D\zeta}{Dt}}_{A} = -\underbrace{(\zeta + f)\left(\frac{\partial u}{\partial x} + \frac{\partial v}{\partial y}\right)}_{B}\left(-\underbrace{\frac{2\Omega cos\phi}{a}v}_{C} + \underbrace{\frac{\partial w}{\partial y}\frac{\partial u}{\partial z} - \frac{\partial w}{\partial x}\frac{\partial v}{\partial z}}_{D}\right) + \underbrace{\frac{\partial p}{\partial x}\frac{\partial \alpha}{\partial y} - \frac{\partial p}{\partial y}\frac{\partial \alpha}{\partial x}}_{E}\left(
$$

$$(1.11)$$

Term B describes the change of vorticity as the product of divergence of the wind field and vorticity itself ($\zeta + f$ is the absolute vorticity) [10]. Implicit in the equation is the statement that divergence (convergence) can destroy (create) vorticity. Only at the level of non-divergence, where divergence is zero and cancels the dependence of the change of vorticity on vorticity itself, can the assumption be made that all vorticity is conserved and only horizontally advected. By investigating vorticity advection at 500 hPa, there exists

14

the chance of some vorticity being created or destroyed by divergence in addition to being advected.

By choosing to ignore the divergence term in the vorticity equation, analysis of vorticity is limited to the level of non-divergence. The assumption is made because the thermal wind usually ensures increasing winds with height. However, increasing winds with height is not always the case. Also, winds increase with height at different rates depending on where jet streaks and the low level jets set up in each trough. Only three-dimensional analysis of vorticity and divergence can absolutely identify increasing positive vorticity advection with height.

Term E of 1.11 relates the twisting and turning of the winds due to absolute vorticity. Specifically, it incorporates the effect of a horizontal gradient of vertical velocity in changing a horizontal axis of vorticity to a vertical axis of vorticity. Winds generally increase with height because of the thermal wind, and the thermal wind is what influences the creation and movement of jet streaks. The horizontal gradient of vertical velocity clearly exists, as jet streaks exist, yet in the analysis of vorticity the sheer term is ignored and focus is instead placed on the advection of vorticity. In many synoptic cases, ignoring the twisting/sheer term is warranted because vertical velocities are so small compared to horizontal velocities. However, when considering mesoscale features or when considering large or strong synoptic systems, ignoring the term introduces unneeded error.

Quasi-geostrophic theory also fails in its relation to Dines' compensation. Dines' Compensation, in the strictest sense, contradicts QG theory. QG theory assumes that winds are geostrophic at sufficient heights; that is, winds do not cross isobars. How-

ever, for Dines' Compensation to hold, winds must leave or enter areas of divergence and convergence. Areas of divergence and convergence are associated with areas of deviant pressure, thus winds cross isobars. It is the ageostrophic component of the winds that performs the function of mass removal, so while the necessity of the ageostrophic wind is apparent, QG theory assumes it does not exist.

Dines' Compensation is not completely valid, as a parcel is displaced horizontally it is forced to rise vertically, so the movement of mass aloft in one area can force surface pressure changes in another area. Additionally, the bowstring vertical profile is not always true. For example, there may be divergence aloft and at the surface and a layer of convergence in the mid-levels, making vertical motion limited in extent. Herein lies the reason the three-dimensional study of QG theory and its causes, vorticity advection and temperature advection, is so important - horizontal motion aloft does not translate into motion at the surface all of the time. Each cause and effect must be analyzed throughout the atmospheric column to determine the vertical motions of the atmosphere.

It is these failings in QG theory that present the need for a more comprehensive view of the atmosphere via 3D analysis. By using three-dimensional diagnostic and visualization techniques, assumptions can be removed from the interpretation of QG model output. A first step to the adoption of three-dimensional visualization should be viewing the QG omega and geopotential tendency equations in three dimensions. To that end, this study develops a method, by evaluating the QG equations across the NAM model domain, to provide for reliable visualizations. The question remains though, if there are so many assumptions in the most widely used forecasting technique in meteorology and if 3D vi-

sualization could be so useful in ameliorating those problems, why has 3D analysis not already been adopted?

1.9   3D Visualization

Steps have been taken towards three-dimensional visualization, but only recently has three-dimensional visualization begun to develop more widespread acceptance in meteorology. Visualization of satellite and radar data are among the most prevalent [20], [1], [56]. Education has also begun utilizing three-dimensional visualization [29]. Computer scientists have worked to adapt three-dimensional datasets to visualization in a virtual environment [57]. Visualization of model data has been slower to be embraced, but many attempts have been made. Beginning in 2000, model output was visualized in three dimensions [49], [2]; however, since then, adoption has been limited.

Despite the continued development of three-dimensional visualization tools, operational use of three-dimensional visualization has been limited for several important reasons.

1.) The programs used are resource intensive. Only the most advanced personal computers are capable of running visualization software.

2.) Although the computer processing power required to display three-dimensional data in real time has existed for some time, the bandwidth required to send the data through a network is still limited. Considering that each time step of one model run might be upwards of hundreds of MB and that each model run may contain dozens of time steps,

17

a single model run may be 10 GB. Even with high speed internet access, download times may be upwards of several hours, by which time a new model run will have been generated.

3.) Meteorological education focuses on two-dimensional analysis as a means of forecasting and diagnosis. As a result of the lack training, demand for a new visualization platform has been limited.

4.) Most importantly, for certain variables, considerable low-amplitude noise is pervasive. This is particularly evident for the winds and any wind derived variable, especially vertical velocities, divergence, and vorticity. The cause of this phenomena is the increase resolution of NWP models. QG analysis works across the synoptic scale, but NWP models can resolve features to a small as 1 km. The result of viewing such fine resolution data on a large scale is unintelligible. Large scale smoothing is required to flesh out synoptic scale patterns of forcing. The method presented here of dynamical smoothing using the QG equations themselves as guide is the most physically grounded.

Each of these hindrances to the adoption of 3D visualization is slowly being lessened. Computer power has advanced recently so that mid-range consumer laptops are capable of running visualization software, high speed data networks allow for the rapid transfer of data, and meteorologists are slowly recognizing the power of 3D visualization in education and operational weather analysis. It is reason four, the lack of interpretation and smoothing methods, that remains as the greatest hindrance to the adoption of 3D visualization of meteorological data.

1.9.1 Paraview

Paraview is an open source software platform built on the Visualization Toolkit (VTK). It has wide applications across the computer sciences, but is only now beginning to be developed for use in meteorology [16]. Though other, more specialized, software platforms are available to visualize meteorological data, Paraview has several distinct advantages [28].

1.) ability to use the GPU to process graphics

2.) ability to use multi-core processors

3.) reduced use of RAM

4.) ability to use multiple kinds of data formats

5.) ability to script program functions

The ability of Paraview to use the GPU and multi-cored processors dramatically lessens the time required to render complex graphics. Support for varying data formats and scripting features expands the capability of Paraview to allow for various numerical weather prediction model input. For these reasons, Paraview is the visualization platform used in this study.

1.10   Objective and Merit

QG theory has been well developed and can be summarized by two fundamental equations, the QG omega equation and the QG geopotential tendency equation. Additionally, QG theory has been extensively applied to operational problems. The problem with QG analysis is the balancing act forecasters must perform when diagnosing areas of interest.

Forecasters must look at two separate terms when observing the omega equation, that of vorticity advection and of temperature advection. The issue occurs because the two components are not independent of one another [50]. Each component of the omega equation and the geopotential tendency equation must be viewed side-by-side to diagnose areas of vertical velocities and height tendencies. By locally evaluating the omega and geopotential tendency equations term by term, the separate types of forcings can be determined whether due to vorticity or thickness advection. Three-dimensional visualization is the most viable method of discerning forcing type and strength.

Unfortunately, a lack of computer processing power during the development of QG theory has limited the interpretation of the theory to a series of two-dimensional maps that necessitate the use of several assumptions that introduce error. Now that the evolution of personal computers has caught up to the theory, the atmosphere can be viewed in three dimensions to decrease forecast time and remove assumptions in QG theory. A major barrier to the evolution of NWP visualization is the lack of reliable, physically-derived smoothing techniques to clean noisy model fields. One possible method of method of smoothing is presented here.

Analysis of the zero hour forecast fields of the NAM is a logical first step towards the discipline wide adoption of 3D forecasting techniques while also addressing concerns resulting from the resource intensive nature of 3D analysis. By limiting the scope of the study to the zero hour model fields, the resources and time required to download the data are greatly diminished. Fortunately, limiting the scope in such a way does not limit the

ability for the replication of the techniques employed to be expanded to full model-run analysis.

Hoskins [24] affirmed that timely, reliable, and accurate methods of model verification are necessary to determine the physical validity and plausibility of model initializations. To address this issue, a careful study of the 3D structure of each of the QG fields is required. The objective of the study is the evaluation of NWP model fields using a QG system of equations to achieve dynamic smoothing for ease of 3D visualization. It is hypothesized that the calculated omega without static stability correlates more closely to model omega than omega with static stability.

CHAPTER 2

METHODS

The omega and geopotential tendency fields were evaluated from the geopotential height fields using the QG omega and QG geopotential tendency equations for the zero hour NAM diagnostic fields. Each of the four forcing terms was calculated individually, allowing for the separation of forcing from vorticity advection and thickness advection. A stand-alone program, written in C++, used the VTK libraries to convert GRIB2 files to VTK files. A second program, written in C++, calculated each term of the omega and geopotential tendency equations from the gridded data and appended the resulting values to the original data file. Partial derivatives were evaluated using the method of finite differencing. Evaluated omega was correlated to model derived omega for the entire atmospheric volume and the 300 hPa, 500 hPa, and 700 hPa levels. Evaluated omega for the atmospheric volume and the 300 hPa, 500 hPa, and 700 hPa was contoured using using Paraview. Eight case studies were performed for various synoptic setups.

2.1   Finite Differencing

The method of finite differencing has been used to numerically calculate derivates and integrals in meteorological equations since Charney first developed a set of equations to forecast the weather [8]. Finite differencing approximates continuous derivatives into

discretized algebraic equations. In a model grid, spacing between points is known. That is the distance between grid cells, Δ, is some easily calculated value. The change in value of some variable, M, can be determined by subtracting the value at one grid cell from the value at an adjacent grid cell. The approximation of the partial derivative using a single-moment central difference is:

$$\frac{\partial M}{\partial x} = \frac{1}{2\Delta} \left[M_{i+1} - M_{i-1} \right] \tag{2.1}$$

where the subscripts, $i + 1$ and $i - 1$ refer to the position of grid cells away from the grid cell where the difference is being calculated. The second derivative is calculated in a similar way:

$$\frac{\partial^2 M}{\partial x^2} = \frac{1}{(2\Delta)^2} \left[M_{i+2} - 2M_i + M_{i-2} \right] \tag{2.2}$$

The del operator is also easily applied using the finite difference method. As the scale of each calculation was no more than $150km$ (see section 2.7), x, y calculations are orthogonal for each grid point. Therefore, 2D partial derivates can be calculated using a simple sum of the x and y components of each operated quantity. Divergence was calculated from the difference of u winds in the x direction and v winds in the y direction on points on either side of the center grid point. The divergence of a quantity, the dot product of a quantity with the del operator, is found by:

$$\nabla \cdot \vec{V} = \frac{(u_{i+s} - u_{i-s})\text{m/s}}{(2\Delta \times s)\text{km}} + \frac{(v_{j+s} - v_{j-s})\text{m/s}}{(2\Delta \times s)\text{km}} \tag{2.3}$$

Vorticity, the cross product of a field with the del operator, was calculated in a similar way by taking the finite difference of u winds in the y direction and v winds in the x direction.

$$\nabla \times \vec{V} = \frac{(v_{i+s} - v_{i-s})\mathrm{m/s}}{(\Delta \times s)\mathrm{km}} - \frac{(u_{j+s} - u_{j-s})\mathrm{m/s}}{(\Delta \times s)\mathrm{km}} \tag{2.4}$$

The indices i and j represent each grid point iteration in the x and y directions, respectively. The offset, s, is the number of grid spaces away from the center point that are used in the calculation; Δ is the distance between grid cells. As of 2011, each grid point in the operational NAM is approximately 12 km away from its perpendicular neighbor, so for example, with a grid spacing of 10, the distance would be $10 * 12 + 10 * 12$. Vertical derivates were calculated using a single-moment, backwards difference calculation. As the omega equation and the geopotential tendency equations use pressure as the vertical coordinate, vertical derivatives take the form:

$$\frac{\partial M}{\partial p} = \frac{1}{2\Delta P}[M_k - M_{k+1}] \tag{2.5}$$

Though many other methods of difference approximation exist, for example, triangle, trapezoid, etc., for a regularly spaced grid, the finite differencing method has been proven to be of equal or better proficiency in defining derivatives while also being resource efficient [3], [42].

2.2   Data Used

Zero-hour forecast fields from the North American Mesoscale (NAM) model [55] were used due to the close spacing of grid points. Model data were used instead of observations because model fields are the only source of evenly spaced three-dimensional data

24

and because of the consistency of model products across model runs [27]. Though the grid somewhat varies by latitude, the NAM provides an approximately 12 km x 12 km x 39 vertical level gridded map of model output across the United States with meteorological variables calculated at the center of each grid cell. The wind field, temperature field, geopotential height field and pressure fields were required in the calculations of the geopotential tendency and omega equations.

2.3 Equations Used

The Quasi-Geostrophic omega equation and the QG geopotential tendency equation were used as derived from [21]. The omega equation is given as:

$$\left[\nabla^2 + \frac{f_0^2}{\sigma}\frac{\partial^2}{\partial p^2}\right]\omega = \frac{f_0}{\sigma}\frac{\partial}{\partial p}\left[\vec{V_g}\cdot\nabla\ \frac{1}{f_0}\nabla^2\Phi + f\right] + \frac{1}{\sigma}\nabla^2\left[\vec{V_g}\cdot\nabla\ -\frac{\partial\Phi}{\partial p}\right]\left(-\frac{\kappa}{\sigma p}\nabla^2 J\right)$$

(2.6)

As the scope of the study is limited to adiabatic forcing, term D was dropped as J is a result of diabatic heating. Giving:

$$\underbrace{\left[\nabla^2 + \frac{f_0^2}{\sigma}\frac{\partial^2}{\partial p^2}\right]\omega}_{A} = \underbrace{\frac{f_0}{\sigma}\frac{\partial}{\partial p}\left[\overbrace{\vec{V_g}\cdot\nabla\ \frac{1}{f_0}\nabla^2\Phi + f}^{B_1}\right]}_{B} + \underbrace{\frac{1}{\sigma}\nabla^2\left[\overbrace{\vec{V_g}\cdot\nabla\ -\frac{\partial\Phi}{\partial p}}^{C_1}\right]}_{C}$$

(2.7)

And the geopotential tendency as:

$$\underbrace{\left[\nabla^2 + \frac{\partial}{\partial p}\ \frac{f_0^2}{\sigma}\frac{\partial}{\partial p}\right]\chi}_{D} = \underbrace{-f_0\left[\overbrace{\vec{V_g}\cdot\nabla\ \frac{1}{f_0}\nabla^2\Phi + f}^{B_1}\right]}_{E} - \underbrace{\frac{\partial}{\partial p}\left[\frac{f_0^2}{\sigma}\left[\overbrace{\vec{V_g}\cdot\nabla\ -\frac{\partial\Phi}{\partial p}}^{C_1}\right]\right]}_{F}$$

(2.8)

The terms B (C) of the omega equation and E (F) of the geopotential tendency equation are very similar. The sections labeled B_1 of the omega and geopotential equations are the

25

same. Those terms are calculated as follows: the Laplacian of the geopotential field, $\nabla^2\Phi$, is first found. The finite difference expression to calculate that field is:

$$\nabla^2\Phi = \frac{1}{(2s\Delta)^2}\left[\Phi_{i+s} - 2\Phi_i + \Phi_{i+s}\right] + \frac{1}{(2s\Delta)^2}\left[\Phi_{j+s} - 2\Phi_j + \Phi_{j+s}\right] \qquad (2.9)$$

Where s is the number of grid spaces (see section 2.7), and Δ is the distance between horizontal grid points.

Following Holton [21], the Coriolis forcing term is defined by the $midlatitude\ \beta -$ $plane\ approximation$, which is the Taylor Series expansion of f.

$$f = f_0 + \beta y \qquad (2.10)$$

where $\beta = 2\Omega cos\phi/a$. When defining $\vec{V}_g$, the $\beta - plane\ approximation$ is unnecessary and f can be approximated by f_0 [21]. Dividing the laplacian of the geopotential by the Coriolis parameter then adding the Coriolis parameter gives an expression for the vorticity, denoted Γ.

With a new field defined by Γ, the gradient of that field was taken using the expression:

$$\nabla(\Gamma) = \frac{1}{(2s\Delta)}\left[(\Gamma_{i+\Delta} - \Gamma_{i-\Delta}), (\Gamma_{j+\Delta} - \Gamma_{j-\Delta})\right] = E \qquad (2.11)$$

The dot product of the result of equation 2.11 and the geostrophic velocity was taken. Multiplying by $-f_0$ gives term E in the geopotential tendency equation.

Continuing within term B of the omega equation, the partial derivative with respect to pressure must be taken. This involves a vertical finite difference and is calculated using the expression:

$$\frac{\partial E}{\partial p} = \frac{1}{(2\Delta P)}\left[E_k - E_{k+1}\right] \qquad (2.12)$$

26

As the vertical resolution is much smaller than the horizontal resolution, a backwards difference method was used to reduce truncation errors at the top and bottom of the troposphere. The values of each vertical difference were assigned to the bottom difference (i.e. the difference taken between 975 and 1000 hPa was assigned to the 1000 hPa level). Lastly, the expression was multiplied by Coriolis parameter, f_0 and divided by the static stability parameter, σ. Where

$$\sigma = -\frac{RT}{P}\frac{d(ln\theta_0)}{dp} \tag{2.13}$$

and

$$\frac{d(ln\theta_0)}{dp} = \frac{1}{(2\Delta P)}\left[(ln\theta_0)_k - (ln\theta_0)_{k+1}\right] \tag{2.14}$$

This gives a field describing term B of the omega equation.

Term C_1 was calculated in the following way. The partial derivative with respect to pressure of the geopotential field was evaluated using equation 2.15:

$$\frac{d\Phi}{dp} = \frac{1}{(2\Delta P)}\left(\Phi_k - \Phi_{k+1}\right) = Z \tag{2.15}$$

The gradient of that quantity was taking using the expression:

$$\nabla(Z) = \frac{1}{(2s\Delta)}\left[(Z_{i+\Delta} - Z_{i-\Delta}),(Z_{j+\Delta} - Z_{j-\Delta})\right] = H \tag{2.16}$$

Taking the dot product of the result of equation 2.16 and the geostrophic wind gives the expression $\vec{V_g} \cdot \nabla\left(-\frac{\partial\Phi}{\partial p}\right)$ which is term C_1. For the omega equation, the laplacian of that product was taken using equation 2.17

$$\nabla^2 H = \frac{1}{(2s\Delta)^2}\left[H_{i+s} - 2H_i + H_{i+s}\right] + \frac{1}{(2s\Delta)^2}\left[H_{j+s} - 2H_j + H_{j+s}\right] = \Theta \tag{2.17}$$

The result of equation 2.17 was divided by the static stability parameter, equation 2.13. This is term C of the omega equation.

For the geopotential tendency equation, the C_1 term was multiplied by $-\frac{(f_0)^2}{\sigma}$ and was then differentiated with respect to pressure using equation 2.18 to give term F.

$$\frac{d\Theta}{dp} = \frac{1}{(2\Delta P)} \left(\Theta_k - \Theta_{k-1} \right) \tag{2.18}$$

These four terms were then summed to yield numerical quantities for the omega and geopotential forcing fields.

2.4 Visualization Methods

The construction of three dimensional vorticity, omega, geopotential tendency, and divergence fields required the utilization of 4D (three Euclidean dimensions, x, y, and z and time) visualization tools. The open-source software Paraview was used to render the omega and geopotential tendency field data. Several common filters were used to visualize the separate variables. Contour filters plot three-dimensional isosurfaces, for example the 500 hPa isobar. Glyphs are geometric shapes such as arrows, lines, or cones denoting vectors and can be scaled by vector magnitude or other scalars. Stream tracers denote the path a released parcel will take as it travels though the control volume. Vorticity was visualized using the stream tracer, contour, and glyph filters. Divergence was visualized using the glyph and contour filters. Near zero $\pm 10\% O(\nabla \cdot \vec{V})$ values of divergence and vorticity are best viewed by coloring wind magnitude glyphs due to the chaotic nature of mesoscale winds. Areas of intense divergence and vorticity can be viewed using the contour filter. Vorticity was also viewed by coloring stream tracers by vorticity. Thickness advection is

best viewed by contours. The resultant omega forcing and geopotential tendency products are best viewed using a contour filter.

Contours were the primary visualization method for viewing the resultant forcings from the omega equation. For each case study day three isobaric levels were chosen (300 hPa, 500 hPa, 700 hPa) to represent the upper levels, the mid levels and the lower levels. On these levels model omega, as taken directly from the NAM, is compared next to term omega calculated without sigma. A second set of three dimensional images is shown. For these images, a specific value of the forcing term is selected and contoured. The contours are colored by pressure to show height in the atmosphere.

To construct the images with the least amount of noise, some areas of the model domain were removed from the dataset. The topmost vertical level ($\sim$ 50 hPa) was removed to account for the large error at the topmost level from the backward difference pressure calculations. Also, for imaging term omega calculated with sigma, the bottom 6 layers (1000-850 hPa) were removed from the dataset as the boundary layer provides very noisy data. Above the boundary layer, term omega with sigma is less noisy.

2.5 Case Studies

Eight case studies - two for each season - were performed using the described visualization techniques. The eight days were selected based off differences in synoptic setup and as paradigms of differing flow regimes.

The eight case study days are 0z on December 12, 2010, 0z on March 7, 2011, 18z on April 4, 2011, 18z on May 12, 2011, 18z on July 17, 2011, 18z on August 21, 2011, 0z on October 5, 2011, and 0z on January 2, 2012.

The analysis field for each respective time is separately analyzed for each case study day using the visualization techniques described in section 2.4. Those fields are visually compared to the classic model derived QG diagnostic fields, 300 hPa winds and heights, 500 hPa vorticity and heights, and surface potential temperature and heights. Then the model vertical velocities are compared to the calculated omega forcings and also to independent observation fields, specifically infrared satellite and rainfall rates as collected from radar. As there is no model derived geopotential tendency field to compare calculated geopotential tendency, visual and statistical analysis is restricted to only the omega field to allow for direct comparison between the model product and the calculated omega forcing field. Calculated omega with sigma and calculated omega without sigma are treated separately as they differ greatly on the placement of vertical motion and in the level of smoothing achieved.

2.6 Statistical Methods

To quantify the ability of the calculated dynamical forcing terms to reliably represent the atmosphere, a series of correlations is performed between NAM generated omega to calculated omega with sigma and NAM generated omega to calculated omega without sigma. Additionally correlations between the vorticity advection term to the thickness advection term and the vorticity term to model omega and thickness advection to model

omega are also performed. For each of the correlations, correlation values were found for the 300 hPa, 500 hPa, 700 hPa levels and across the entire troposperic column.

2.7 Grid Spacing and Smoothing

The optimum spacing for the horizontal derivatives and thus the best balance between smoothing and loss of data resolution was found using a scree plot for each month [7], [38], [37]. Calculated omega without sigma was evaluated for multiple grid spacings of 1, $2, 5, 10, 15, 20, 30, 50, 100$. (Figure 2.1, Figure 2.2, Figure 2.3, Figure 2.4, Figure 2.5, Figure 2.6, Figure 2.7, Figure 2.8, Figure 2.9) A histogram of 100 bins was constructed, plotting the frequency vertical forcing. The histogram maximum, or the bin with frequencies of 0 vertical forcing, is compared to grid spacing in a scree plot. The inflection point of the curve, where the decision regarding how many grid spaces apart to perform the finite difference calculations is based on the location of the inflection point of the curve [32]. The individual inflection points for the curves varied between $10 - 30$. For March 7, 2011, April 4, 2011, July, 17, 2011, and December 12, 2010 the inflection point is at 20 grid spaces. For the January 2, 2012 case study the inflection point is at 30 grid spaces. For the May 12, 2011 and October 5, 2011 case studies the inflection point is at 10 grid spaces. The August 21, 2011 case study has an inflection point of 15. The overall inflection point for all curves is approximately 20 grid spaces (Figure 2.9). Thusly for equations 2.9 - 2.17, the value $s = 20$.
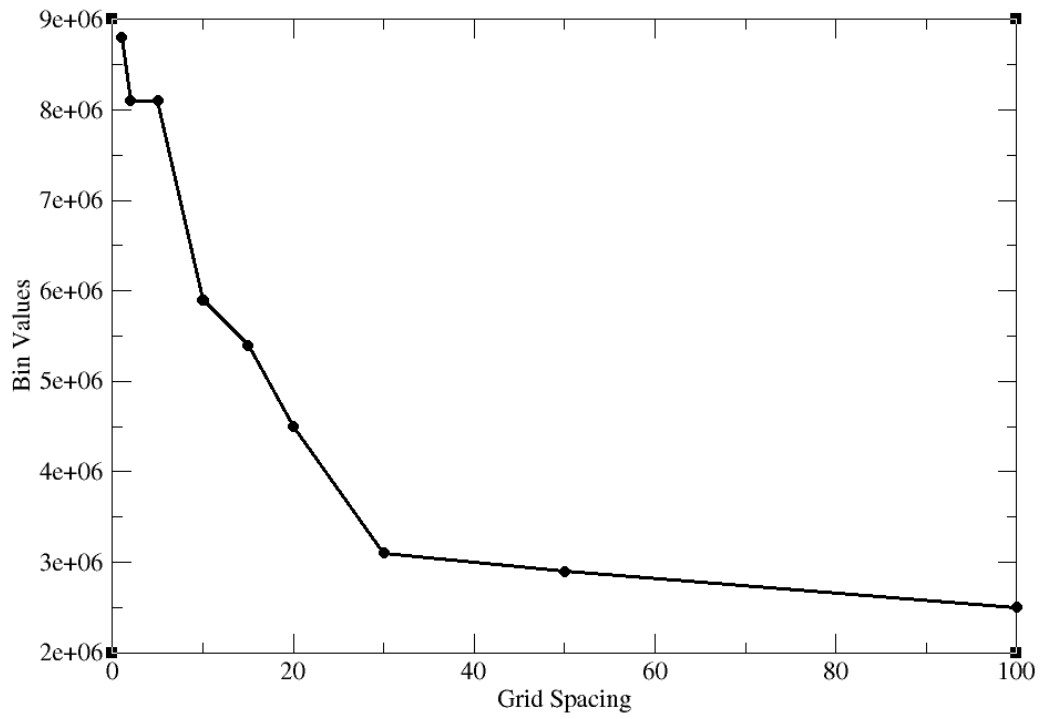
Figure 2.1

Scree plot for the January 2, 2012 case study day.
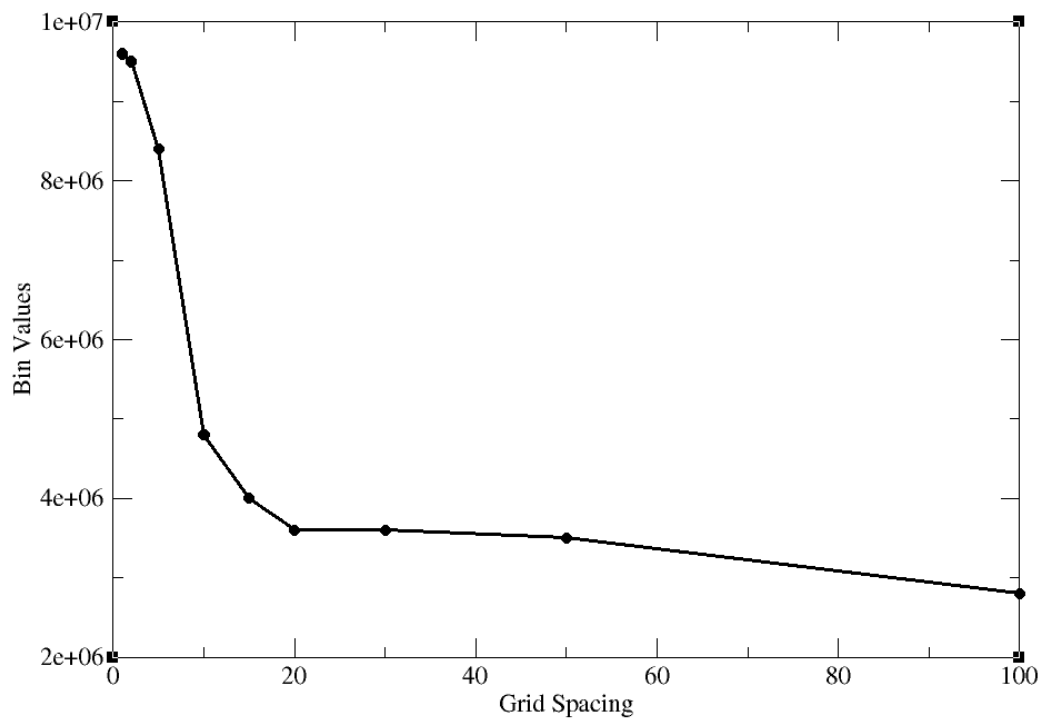
Figure 2.2

Scree plot for the March 7, 2011 case study day.
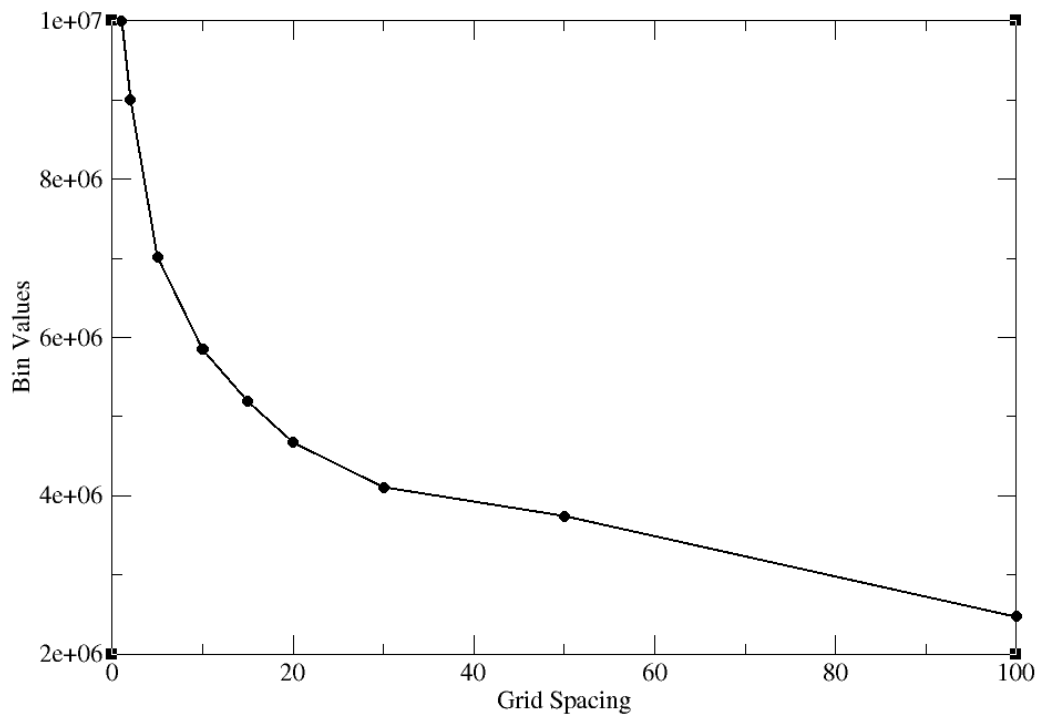
Figure 2.3

Scree plot for the April 4, 2011 case study day.
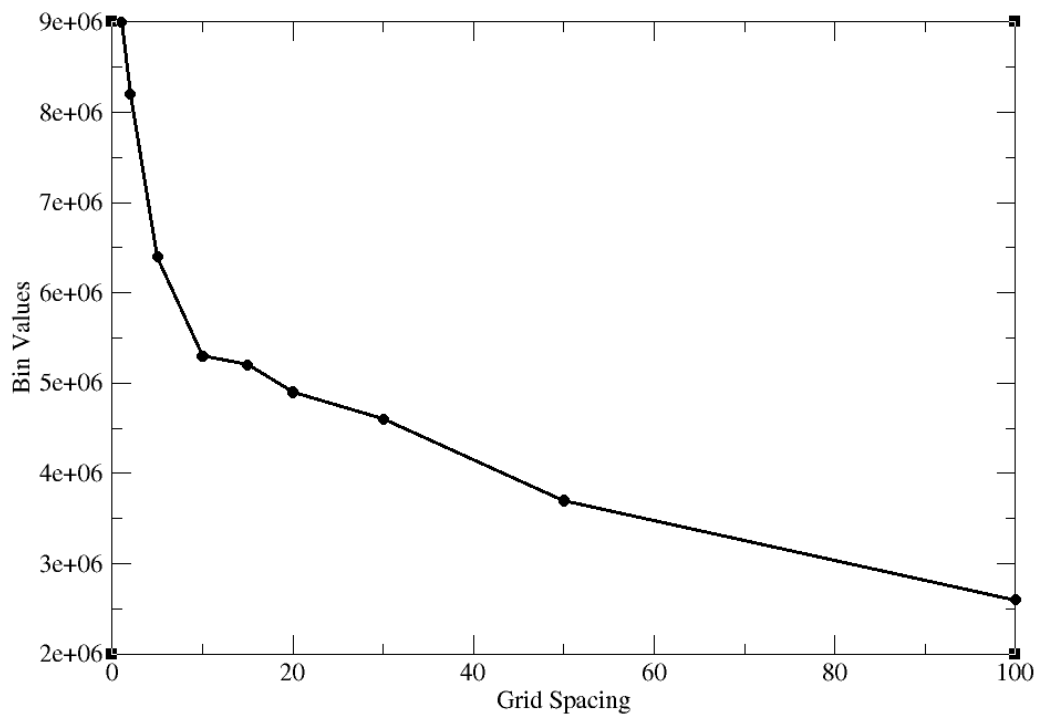
Figure 2.4

Scree plot for the May 12, 2011 case study day.
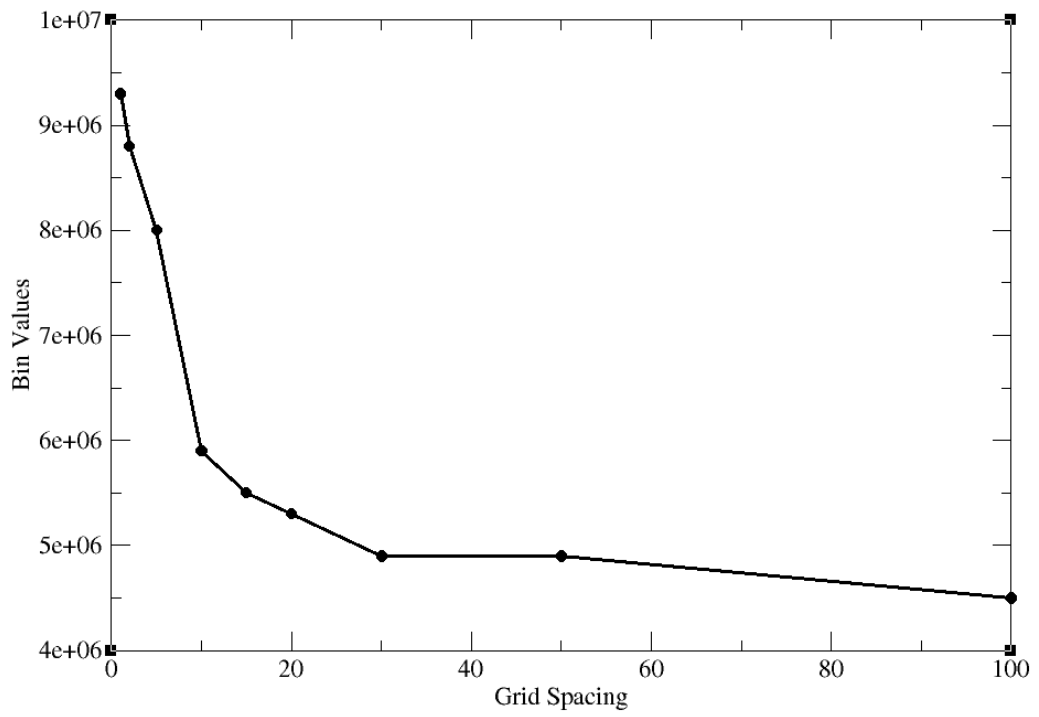
Figure 2.5

Scree plot for the July 17, 2011 case study day.
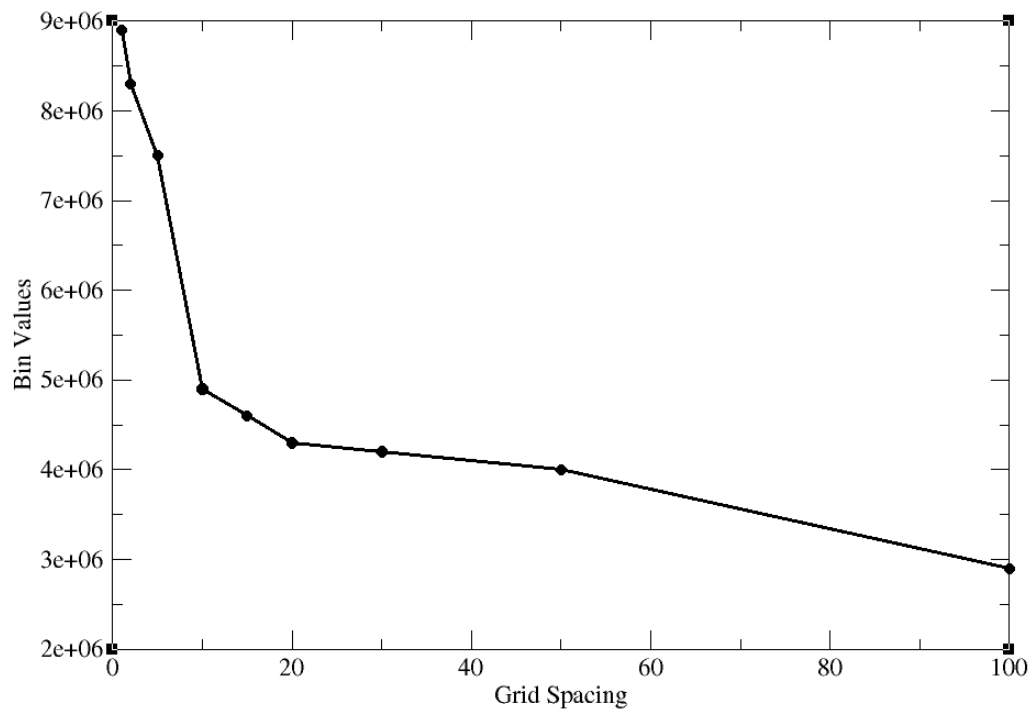
Figure 2.6

Scree plot for the August 21, 2011 case study day.
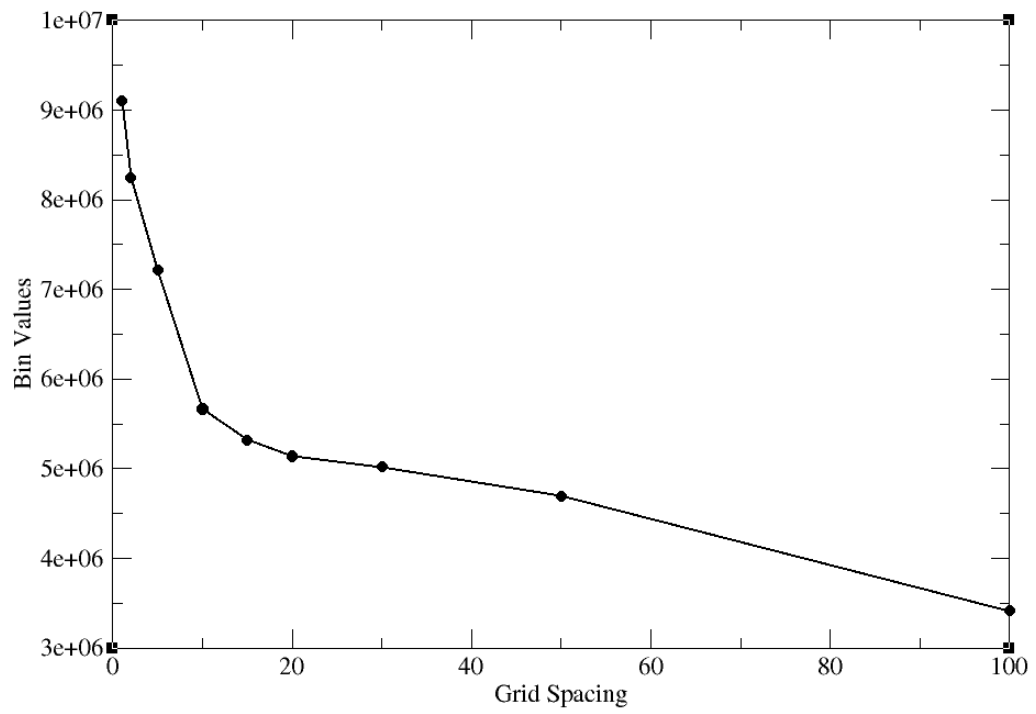
Figure 2.7

Scree plot for the October 5, 2011 case study day.
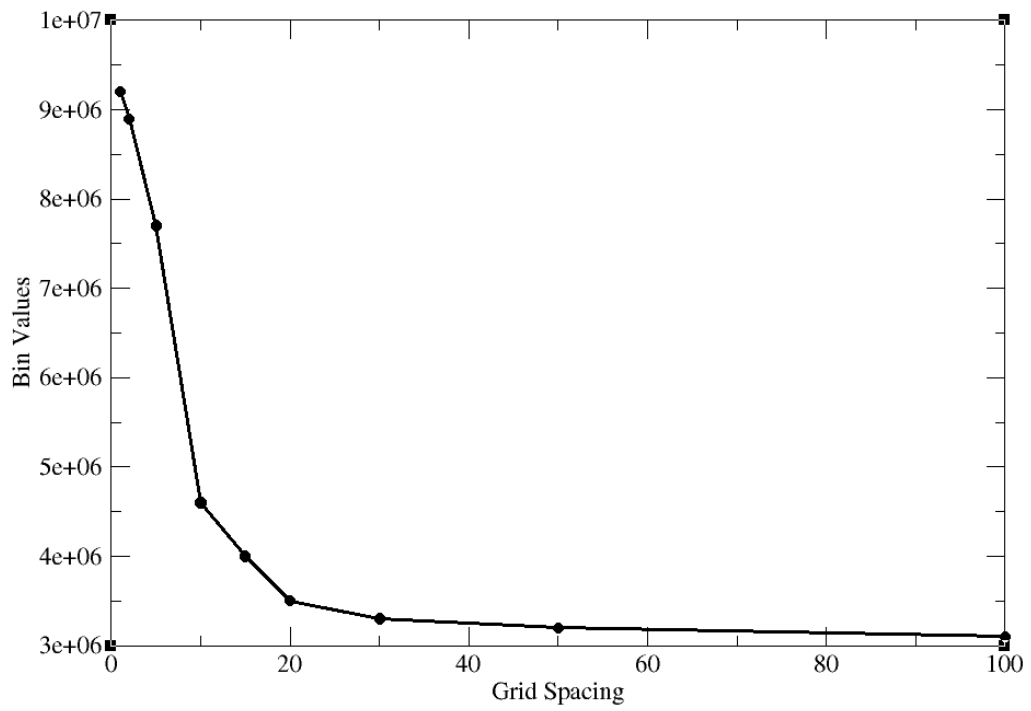
Figure 2.8

Scree plot for the December 12, 2010 case study day.
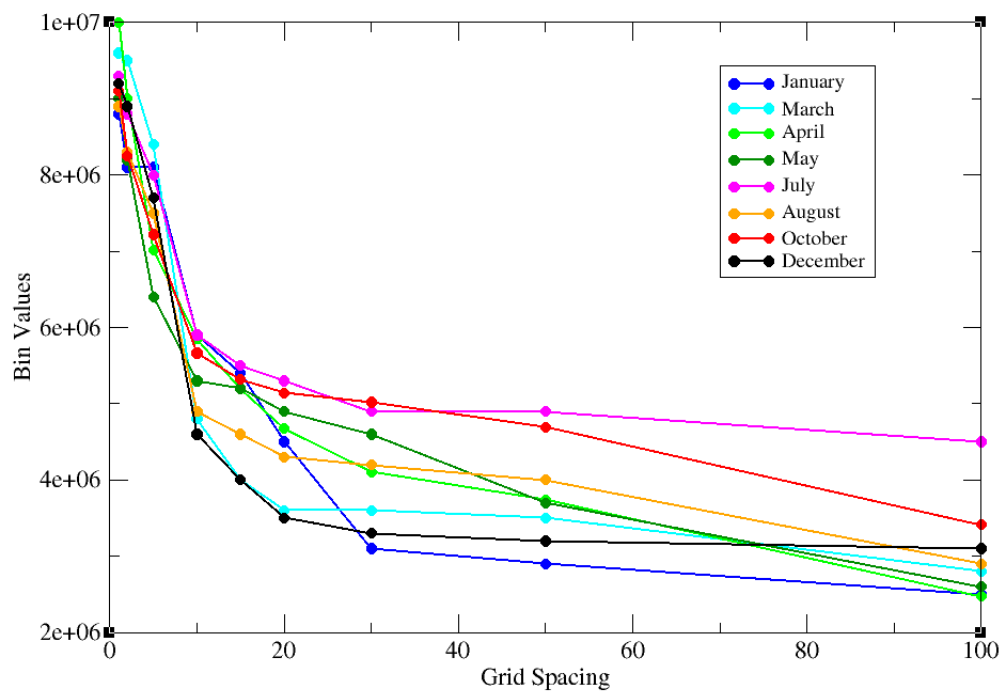
Figure 2.9

Scree plots for all case study days.

CHAPTER 3

RESULTS

Eight case studies were performed to compare term (calculated) omega to model omega. Two days were selected from each season and were chosen based on differences in synoptic flow regimes. The eight case study days were January 2, 2012, March 7, 2011, April 4, 2011, May 12, 2011, July 17, 2011, August 21, 2011, October 5, 2011, December 12, 2010. Analysis maps for each case study day are provided for comparison [19]. For the purposes of this discussion, term omega refers to omega calculated from the QG omega equation without sigma included, while model omega refers to raw vertical velocity data from the associated NAM files.

3.1 Case Studies

For each case day, a series of images is presented. The first image is raw model data for the case study. The second figure for each day is a comparison of model omega and term omega for the 300, 500, and 700 hPa levels. These levels were selected to provide familiarity as 300, 500, and 700 hPa are the mandatory levels for traditional QG analysis and they are the most familiar to operational forecasters. The third figure is a contoured comparison of term omega calculated with sigma, term omega calculated without sigma, vorticity advection, thickness advection, model omega, and divergence. Each of these

figures are oriented vertically to reduce perspective distortion based off of rotated view angle. Additional figures are presented on a case by case basis.

3.1.1 January 2, 2012

An amplified pattern across the continental United States is bringing clouds and precipitation across New England. A trough is being advected into the Great Lakes with a strong vorticity maximum (Figure 3.1c), and a ridge is in place over the Rocky Mountains. Immediately upstream, a second trough looms off the west coast, also with a strong vorticity maximum. A shield of cloud cover hangs over the Great Lakes (Figure 3.1e), associated with the eastern trough, and clouds also cover much of the Pacific Northwest. A third area of clouds over Kansas and Nebraska is associated with downsloping winds as a result of the strong western ridge.

Minimum and maximum ranges on model omega, term omega with sigma and term omega without sigma, vorticity advection, and thickness advection for January 2, 2012 are listed in Table 3.1. Figure 3.1 shows observations from the January 2, 2012 case study day: Panel a.) 300 hPa pressure level heights (geopotential meters) and shaded isotachs ranging from 30 ms^{-1} to 70 ms^{-1}. Panel b.) Surface mean sea level pressure (hPa) and shaded isentropes ranging from 240 k to 290 k. Panel c.) 500 hPa pressure level heights (geopotential meters) and shaded vorticity ranging from -2.0×10^{-4} s^{-1} to 4.0×10^{-4} s^{-1}. Panel d.) One hour rainfall accumulation mm hr^{-1} beginning at 0z. Panel e.) IR Satellite. Figure 3.2 compares the 300 hPa, 500 hPa, and 700 hPa levels for model omega (Panels a-c) and term omega without sigma (Panels d-f): Panel a.) 300 hPa pressure level.

Panel b.) 500 hPa pressure level. Panel c.) 700 hPa pressure level shaded by model derived omega at 3.0×10^{-1} ms^{-1} to -3.0×10^{-1} ms^{-1}. Panel d.) 300 hPa pressure level. Panel e.) 500 hPa pressure level. Panel f.) 700 hPa pressure level shaded by term omega calculated without sigma at 3.0×10^{-5} to -3.0×10^{-5} for January 2, 2012. Figure 3.3 displays the six panel contours for January 2, 2012: Panel a.) Contoured omega calculated with sigma at 1.2×10^{-3} ms^{-1}. Panel b.) Contoured vorticity advection at 2.0×10^{-9} rad s^{-2}. Panel c.) Contoured model derived omega at 7.0×10^{-2} ms^{-1}. Panel d.) Contoured omega calculated without sigma at 1.6×10^{-6}. Panel e.) Contoured thickness advection at 2.0×10^{-9} K s^{-1}. Panel f.) Contoured divergence at 2.5×10^{-2} s^{-1}. Each contour is colored by pressure (75-1000 hPa). Figure 3.4 shows overlapping vorticity advection and thickness advection: Panel a.) Contoured vorticity advection at -2.0×10^{-9} in blue and contoured thickness advection at $+2.0 \times 10^{-9}$ in red. Areas of opposite sign overlap. Panel b.) Contoured vorticity advection at -2.0×10^{-9} in blue and contoured thickness advection at $+2.0 \times 10^{-9}$ in red and contoured term omega 1.6×10^{-6} in white.

Table 3.1

Minimum and maximum ranges for calculated variables for Jan. 2, 2012.

	Lower Bound	Upper Bound
Model Omega	-3.8×10^{-1} ms^{-1}	6.0×10^{-1} ms^{-1}
Term Omega without sigma	-8.3×10^{-5}	7.9×10^{-6}
Term Omega with sigma	-7.2×10^{-2} ms^{-1}	1.6×10^{-1} ms^{-1}
Vorticity Advection	-7.9×10^{-9} rad s^{-2}	7.9×10^{-9} rad s^{-2}
Thickness Advection	-7.9×10^{-9} K s^{-1}	7.1×10^{-9} K s^{-1}

Despite a potent trough pushing though the great lakes, the range of vertical velocities is limited. Term omega calculated without sigma shows a broad area of vertical motion over New England, extending south to Washington D.C (Figure 3.3d). This vertical motion extends though the depth of the troposphere. Other small pockets of upper level vertical motion exist upstream, including an area from Tennessee to Missouri, an area over western Nebraska, and another area over the western Dakotas. The broad area of upward vertical velocities (UVVs) coincides with the most widespread showers and cloud cover over the Northeast US and extends into Canada (Figure 3.1d,e). The trailing areas of dynamic vertical forcing are not associated with cloud cover due to a lack of moisture, except for the area over Nebraska. Model omega (Figure 3.3c) shows a similar pattern except the area of upward vertical velocities is more widespread. In addition, there are trailing UVVs ahead of the dry cold front which extends into the Florida panhandle.

Term omega calculated with sigma (Figure 3.3a) shows scattered vertical motion associated with the upper level low, especially concentrated over Michigan. There is widespread cloud cover in that region, accompanied by scattered lighter showers (Figure 3.1d). Model omega shows almost no UVVs directly associated with the upper level low or with the trailing cold front. A second, more potent trough moves towards the west coast and has stronger vorticity advection associated with it. Both term omega and model omega depict strong UVVs over the west coast of comparable breadth and strength.

Vorticity advection and thickness advection (Figure 3.3b,e) both show widespread forcing along the jet stream (Figure 3.1a). However, upstream of the trough, there are large areas of cancelation between the vorticity advection and thickness advection terms

(Figure 3.4a), and thickness advection forcing and vorticity advection forcing are highly negatively correlated (Table 3.3). When viewing the combined omega term with the advection terms, the extent of term omega is greatly diminished (Figure 3.1b), a result of the high negative correlations. This is to be expected as northwesterly winds bring in cold air from Canada, canceling any possible positive vorticity advection associated with speed shear. The reason for the large values of advection but small values of omega may be a result of the strong jet stream winds. Even small changes in thickness or vorticity equal large advection due to the speed at which they are transported. Divergence (Figure 3.3f) corroborates the placement of vertical motion as a large area of upper level divergence exists over New England and a second large area exists over the eastern Pacific.

Two dimensional slices of term omega (Figure 3.2a-f) offer further insight to the nature of omega over the midwest. At 500 hPa (Figure 3.2e), term omega shows a linear axis of downward vertical velocities extending from Tennessee to Nebraska. This pattern is weakly mirrored at 700 hPa (Figure 3.2f), so while there are some limited values of upward vertical velocities over the midwest, they are limited to the top of the troposphere. In the mid and lower levels vertical motion is downward. Model omega (Figure 3.2b,c) shows minimal vertical motion over the eastern US. The strongest vertical motion shown by model omega is over the western US. Model omega shows spotty, intense areas of vertical motion corresponding to forcing caused by terrain. The resolution of the NAM is fine enough to trace individual mountain ranges, so the predominant cause of vertical motion in the NAM over the Mountain West is orography. Term omega does not see the terrain

and so is not forced by orographic effects; term omega is only forced by dynamics and thus paints a smoother picture of vertical motion.

Pearson's R correlations at 300 hPa, 500 hPa, 700 hPa, and the atmospheric column from 1000 hPa to 50 hPa for model omega to term omega with sigma and term omega without sigma for January 2, 2012 are shown in Table 3.2. Pearson's R correlations at 300 hPa, 500 hPa, 700 hPa, and the atmospheric column from 1000 hPa to 50 hPa for vorticity advection to thickness advection, vorticity advection to model omega, and thickness advection to model omega for January 2, 2012 are shown in Table 3.3. Term omega calculated with sigma shows a weak correlation to model omega (Table 3.2). The strongest correlation is at the 500 hPa level, and the weakest correlation is to the entire atmospheric volume. Term omega calculated without sigma shows a stronger relationship. The upper levels are more strongly correlated than the lower levels with 500 hPa again the strongest; however the relationship between term omega and model omega for the entire column is an order of magnitude smaller than for the upper levels.

Table 3.2

Correlations for model omega to term omega for Jan. 2, 2012.

	With Sigma	Without Sigma
300 hPa	0.0004	0.1690
500 hPa	0.0072	0.2795
700 hPa	0.0018	0.0800
Column	0.0002	0.0915

a.) 300 hPa c.) 500 hPa

b.) Surface d.) Radar

e.) IR Satellite
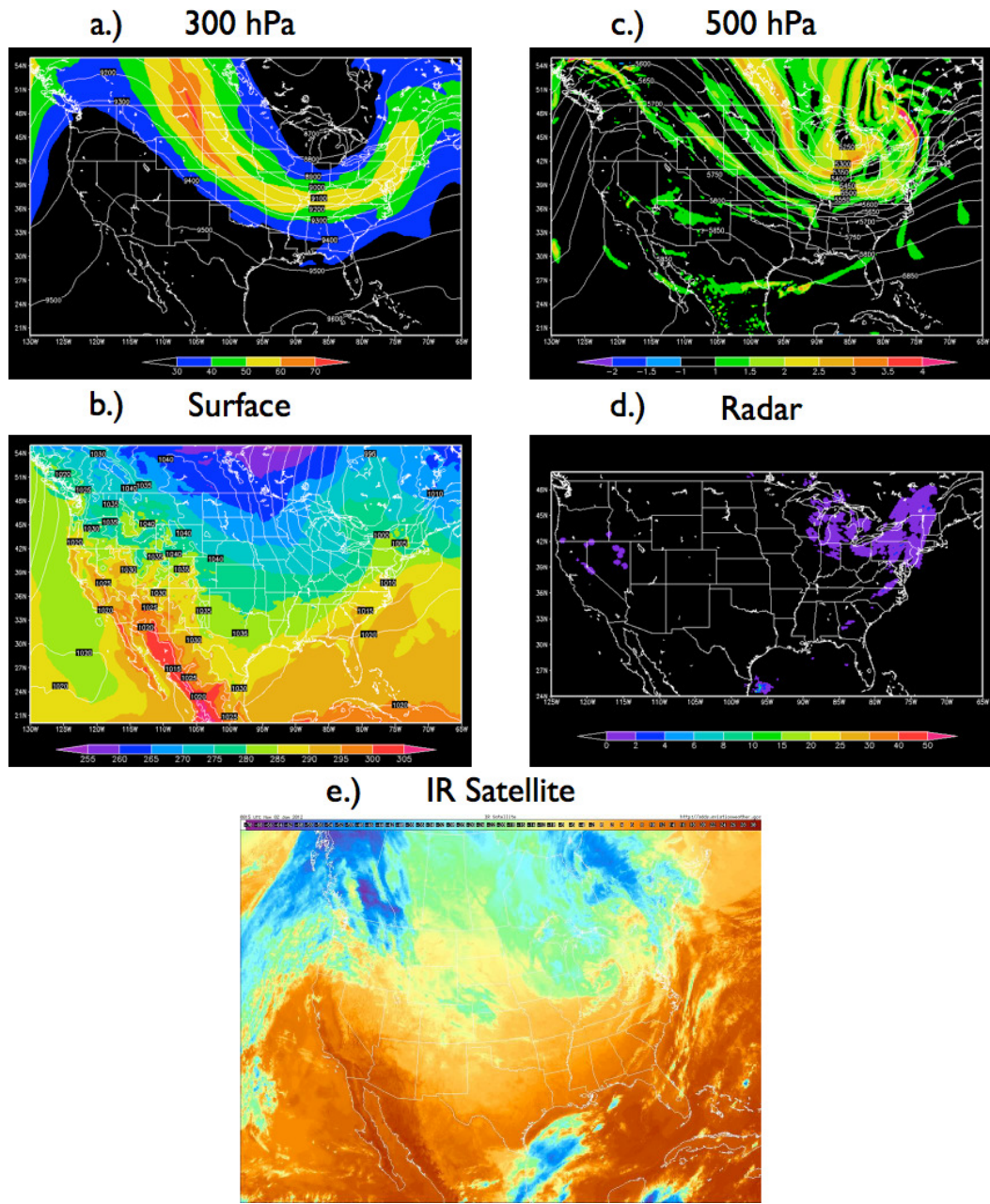
Figure 3.1

January 2, 2012 0z observations.

47
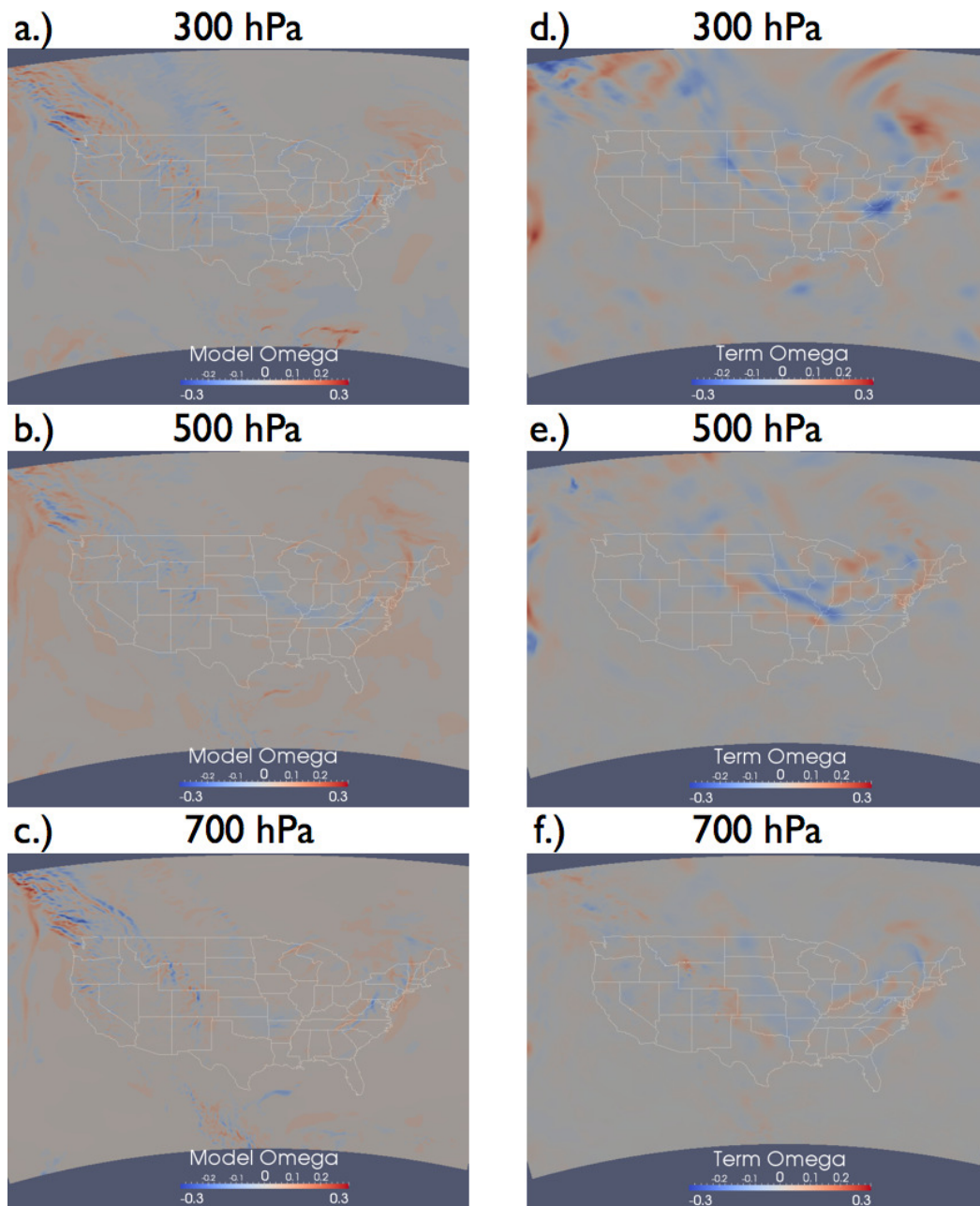
Figure 3.2

Isobars shaded by model omega or term omega without sigma on Jan. 2, 2012
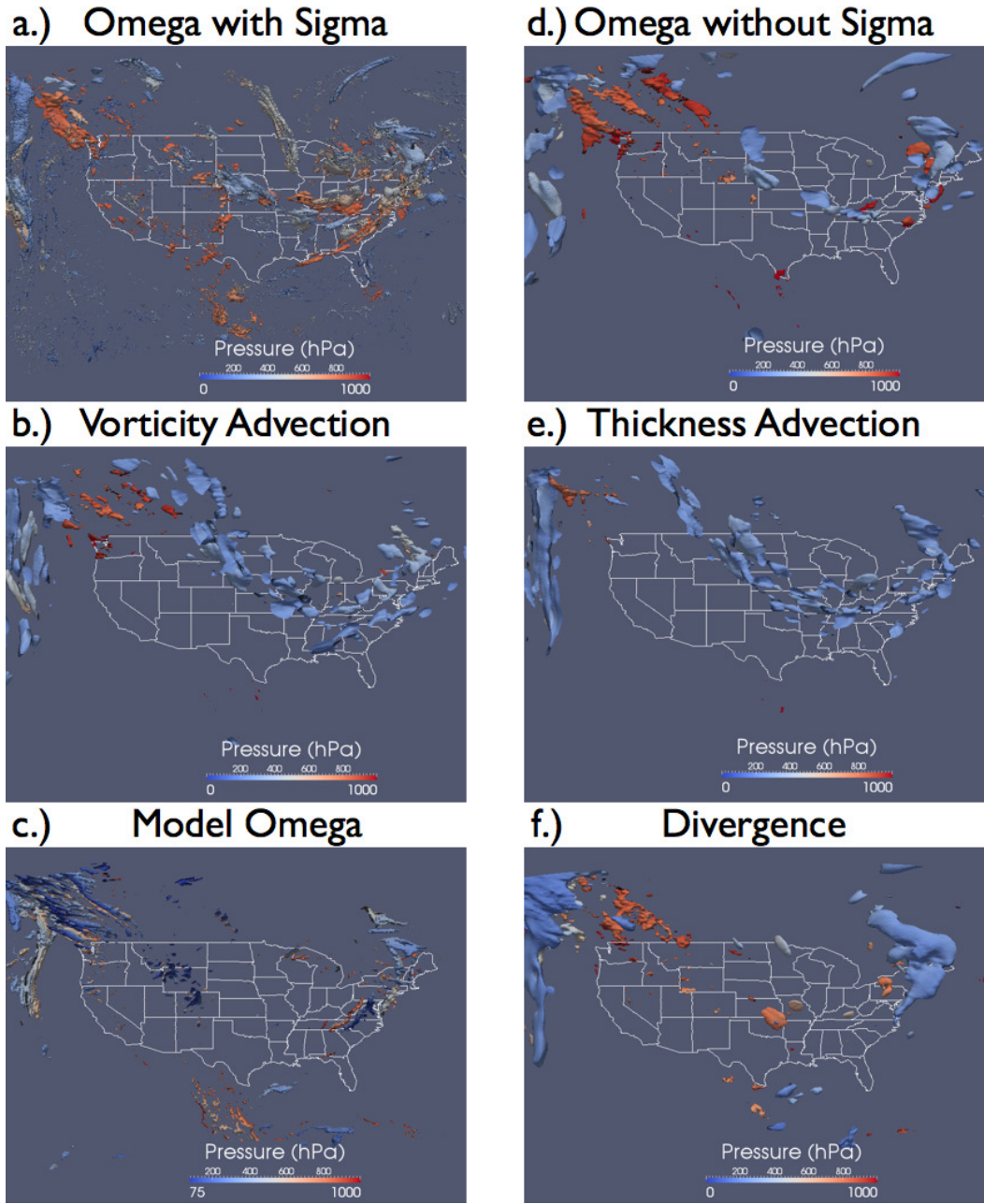
Figure 3.3

Six panel contours for January 2, 2012.

Table 3.3

Correlations between terms for Jan. 2, 2012.

	Vorticity Advection to Thickness Advection	Vorticity Advection to Model Omega	Thickness Advection to Model Omega
300 hPa	-0.8385	0.2985	0.2700
500 hPa	-0.7104	0.5762	0.1660
700 hPa	-0.7700	0.3221	0.3563
Column	-0.7377	0.4634	0.2563
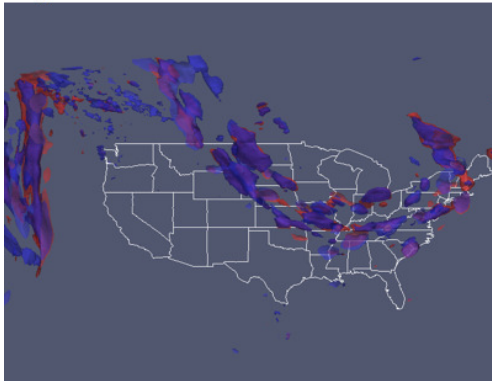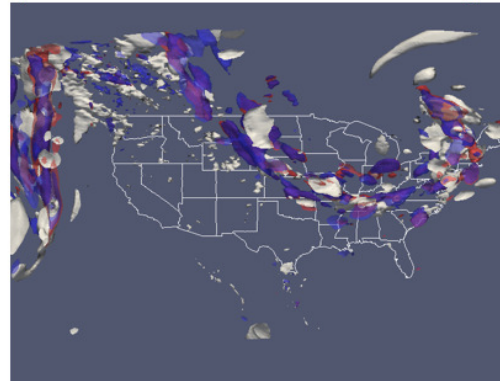
Figure 3.4

Cancelation between vorticity advection and thickness advection.

3.1.2   March 7, 2011

Zonal flow is the predominant pattern across the western two-thirds of the continental United States, while an upper level trough is exiting the eastern seaboard (Figure 3.5a). Figure 3.5 shows observations from the March 7, 2011 case study day: Panel a.) 300 hPa pressure level heights (geopotential meters) and shaded isotachs ranging from 30 ms^{-1} to 70 ms^{-1}. Panel b.) Surface mean sea level pressure (hPa) and shaded isentropes ranging from 240 k to 290 k. Panel c.) 500 hPa pressure level heights (geopotential meters) and shaded vorticity ranging from -2.0×10^{-4} s^{-1} to 4.0×10^{-4} s^{-1}. Panel d.) One hour rainfall accumulation mm hr^{-1} beginning at 0z. Panel e.) IR Satellite. The eastern trough has a localized area of vorticity (Figure 3.5c) persisting over the Carolinas which has developed a large shield of precipitation that is pushing up the eastern seaboard, across the entire Northeast US, from Virginia to Maine (Figure 3.5d). A 300 hPa jet streak (Figure 3.5a) is spurring development of a baroclinic leaf over New England (Figure 3.5e). Scattered showers are developing over Minnesota and Iowa, as well as over Colorado and Utah, and Oregon and California. Each area is associated with a series of shortwaves imbedded within the zonal flow.

Minimum and maximum ranges on model omega, term omega with sigma and term omega without sigma, vorticity advection, and thickness advection for March 7, 2011 are listed in Table 3.4. Figure 3.5 shows observations from the March 7, 2011 case study day: Panel a.) 300 hPa pressure level heights (geopotential meters) and shaded isotachs ranging from 30 ms^{-1} to 70 ms^{-1}. Panel b.) Surface mean sea level pressure (hPa) and shaded isentropes ranging from 240 k to 290 k. Panel c.) 500 hPa pressure level heights

51

(geopotential meters) and shaded vorticity ranging from -2.0×10^{-4} s^{-1} to 4.0×10^{-4} s^{-1}. Panel d.) One hour rainfall accumulation mm hr^{-1} beginning at 0z. Panel e.) IR Satellite. Figure 3.6 compares the 300 hPa, 500 hPa, and 700 hPa levels for model omega (Panels a-c) and term omega without sigma (Panels d-f): Panel a.) 300 hPa pressure level. Panel b.) 500 hPa pressure level. Panel c.) 700 hPa pressure level shaded by model derived omega at 4.0×10^{-1} ms^{-1} to -4.0×10^{-1} ms^{-1}. Panel d.) 300 hPa pressure level. Panel e.) 500 hPa pressure level. Panel f.) 700 hPa pressure level shaded by term omega calculated without sigma at 4.0×10^{-5} to -4.0×10^{-5} for March 7, 2011. Figure 3.7 displays the six panel contours for March 7, 2011: Panel a.) Contoured omega calculated with sigma at 2.5×10^{-3} ms^{-1}. Panel b.) Contoured vorticity advection at 3.0×10^{-9}. Panel c.) Contoured model derived omega at 15.0×10^{-2} ms^{-1}. Panel d.) Contoured omega calculated without sigma at 1.5×10^{-6} rad s^{-2}. Panel e.) Contoured thickness advection at 3.0×10^{-9} K s^{-1}. Panel f.) Contoured divergence at 3.0×10^{-2} s^{-1}. Each contour is colored by pressure (75-1000 hPa).

Table 3.4

Minimum and maximum ranges for calculated variables for Mar. 7, 2011.

	Lower Bound	Upper Bound
Model Omega	-9.8×10^{-1} ms^{-1}	6.5×10^{-1} ms^{-1}
Term Omega without sigma	-8.4×10^{-5}	7.5×10^{-6}
Term Omega with sigma	-7.7×10^{-2} ms^{-1}	1.5×10^{-1} ms^{-1}
Vorticity Advection	-1.1×10^{-8} rad s^{-2}	1.1×10^{-8} rad s^{-2}
Thickness Advection	-1.3×10^{-8} K s^{-1}	1.5×10^{-8} K s^{-1}

Two areas of interest are present for March 7, 2011. The most prevalent forcing feature is the trough which extends across the eastern US with the trailing cold front along the East Coast (Figure 3.5b). Term omega (Figure 3.7d) draws a tube of low level ($\sim$ 900 hPa) vertical velocities just off the New England coast and a large area of upper level vertical velocities extending from New York City southwestward to central Florida. Model omega (Figure 3.7c) presents a similar picture except the lowest level velocities are near the 700 hPa level and are further inland. Model omega paints more scattered upper level vertical velocities further off the eastern seaboard. When compared to satellite and radar imagery (Figure 3.5d,e), model omega more correctly lines up with the position of rainfall over the northeast - Maine through Virginia, while term omega has the greatest forcing off the coast. This is corroborated by the placement of upper level divergence (Figure 3.7f). The 3.0×10^{-2} s^{-1} contour shows upper level divergence over much of the Northeast and off the Carolina coast and lines up with term omega. The high divergence over the northeast is causing the strong vertical motion that is inducing the large shield of precipitation. Though model omega has the placement of the warm front precipitation, term omega correctly places the uplift associated with the cold front.

However, when viewed at pressure levels (Figure 3.6a-f) both model and term omega show the strongest vertical velocities over land, coinciding with the greatest precipitation. The difference between the placement of 3D visualization and 2D visualization term omega could be attributed to the orientation of 3D point of view. For this system, term omega (Figure 3.6d-f) provides limited improvement over model omega (Figure 3.6a-c) except in concentrating forcing along the trailing cold front over the Gulf Stream.

For the west coast, the easiest comparison can be made by viewing the pressure levels (Figure 3.6a-f). The 300 hPa level for term omega (Figure 3.6d) shows the area of vertical velocities associated with precipitation over the California/Oregon border, a second area over northern Nevada and northern Utah, a third maximum over western Colorado, and a fourth area over southeastern Colorado. Each of the areas of vertical forcing corresponds to an area of precipitation (Figure 3.5d). Term omega also shows strong downward velocities over central Nevada and southern Utah, and those areas are lacking in precipitation. Model omega paints localized areas of vertical velocity on the 300 hPa level (Figure 3.6a), associated with orography. At 500 hPa (Figure 3.6b), model omega continues to be focused on orography, while term omega picks up on scattered convection through northern New Mexico. Except for small vertical velocities over the northern Great Plains on the 500 hPa level (1.0×10^{-1} ms^{-1} to 2.0×10^{-1} ms^{-1}), neither term omega nor model omega depict precipitation over Minnesota.

The 3D view of model omega over the west coast demonstrates the fine scale resolution of the NAM (Figure 3.7c) but also demonstrates how high resolution produces noise in vertical velocities. Small, discrete areas of model omega are not organized into discernible patterns over the Southwest. Term omega shows two areas of vertical velocities over Utah and Colorado. Term omega clearly shows an improvement over model omega in the placement of precipitation areas over the west where the NAM is focused on orographic effects.

Pearson's R correlations at 300 hPa, 500 hPa, 700 hPa, and the atmospheric column from 1000 hPa to 50 hPa for model omega to term omega with sigma and term omega

without sigma for March 7, 2011 are shown in Table 3.5. Pearson's R correlations at 300 hPa, 500 hPa, 700 hPa, and the atmospheric column from 1000 hPa to 50 hPa for vorticity advection to thickness advection, vorticity advection to model omega, and thickness advection to model omega for March 7, 2011 are shown in Table 3.6. Term omega calculated with sigma is the most strongly correlated to model omega at the 300 hPa level (Table 3.5). The correlation at the lower levels is an order of magnitude less and even smaller for the entire column. Term omega calculated without sigma has the strongest correlation at 700 hPa with the 500 hPa and 300 hPa levels approximately %20 weaker; the correlation for the entire atmospheric column is weakest at roughly half the strength of the correlation at 700 hPa. This is perhaps due to the overall weaker forcing near the surface and stronger forcing aloft.

Table 3.5

Correlations for model omega to term omega for Mar. 7, 2011.

	With Sigma	Without Sigma
300 hPa	0.0207	0.2741
500 hPa	0.0022	0.2538
700 hPa	0.0052	0.3384
Column	0.0013	0.1505

3.1.3   April 4, 2011

The primary feature is a positively tilted trough that extends through the middle of the country, while weak ridges are in place across each of the coasts. A linear swath of vor-
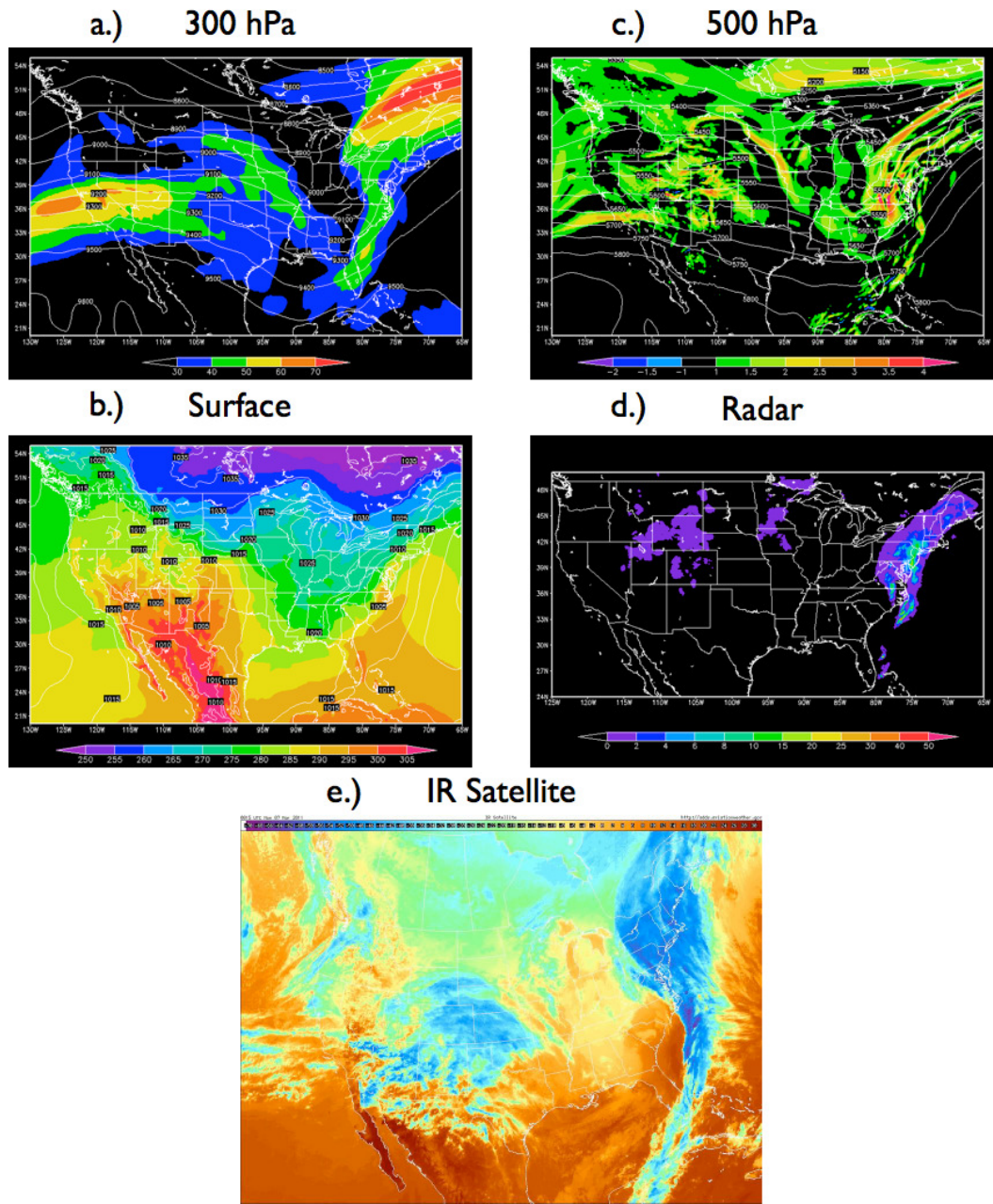
Figure 3.5

March 7, 2011 0z observations
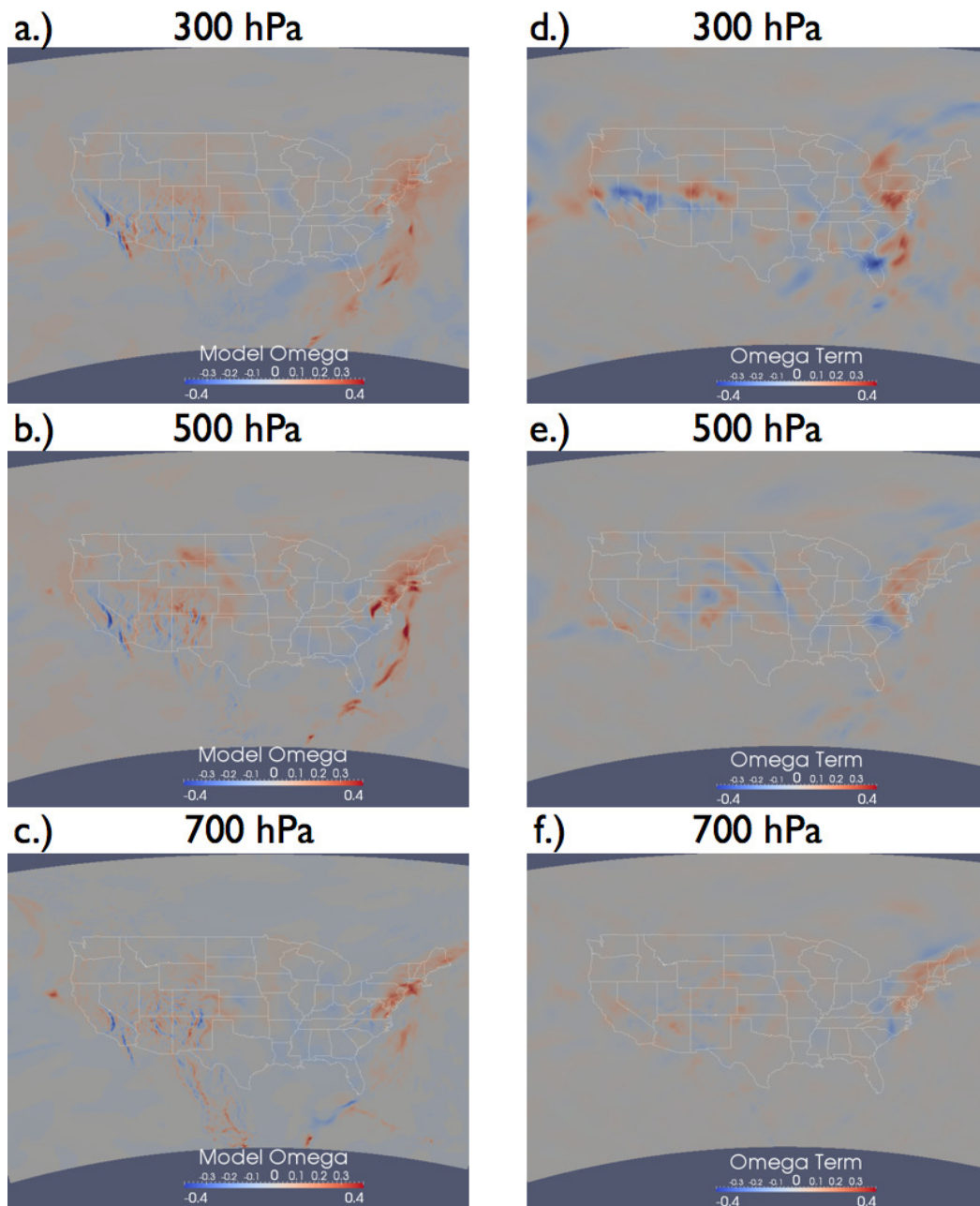
Figure 3.6

Isobars shaded by model omega or term omega without sigma on Mar. 7, 2011

a.) Omega with Sigma

d.) Omega without Sigma

b.) Vorticity Advection

e.) Thickness Advection

c.) Model Omega

f.) Divergence
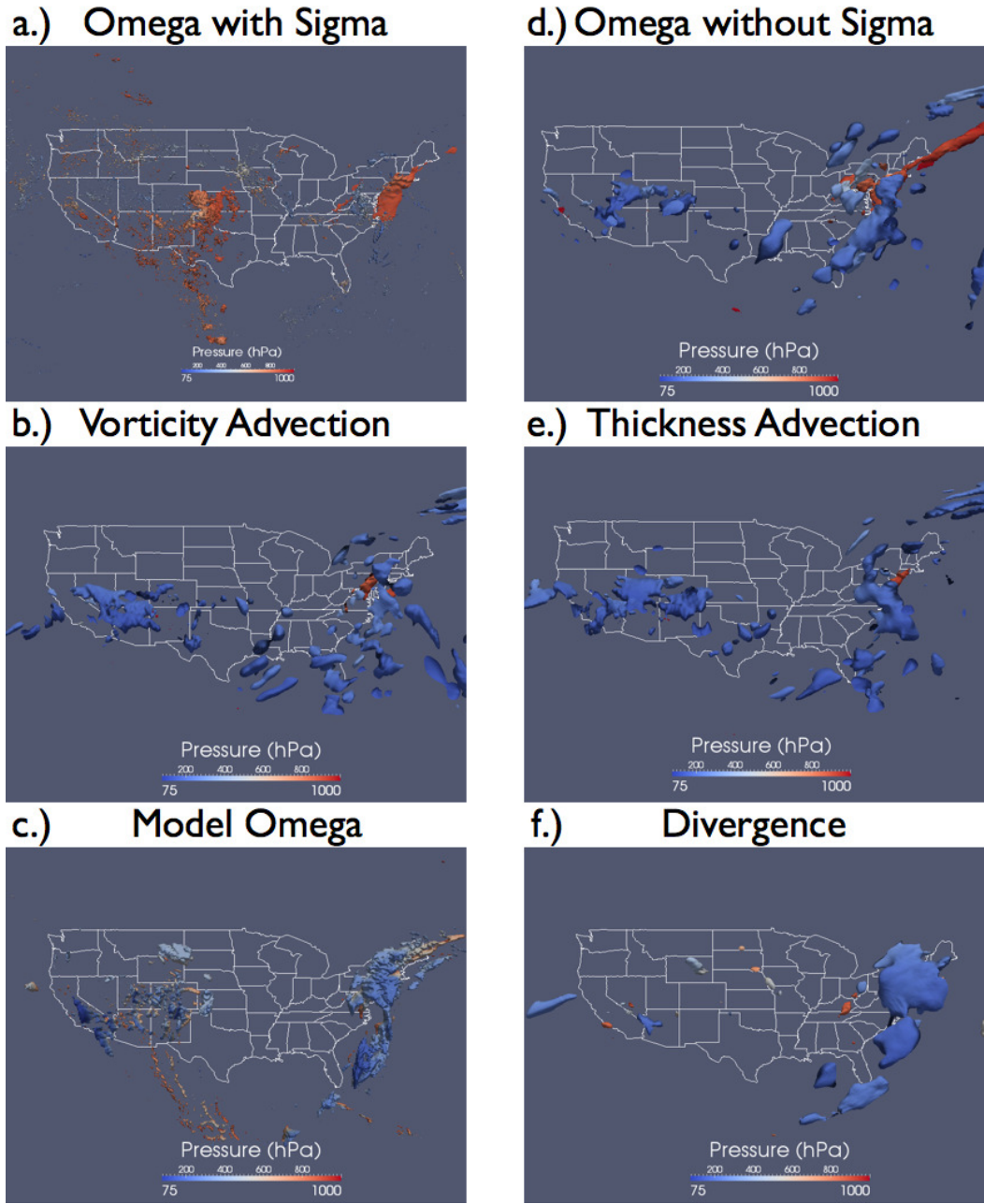
Figure 3.7

Six panel contours for March 7, 2011.

58

Table 3.6

Correlations between terms for Mar. 7, 2011.

	Vorticity Advection to Thickness Advection	Vorticity Advection to Model Omega	Thickness Advection to Model Omega
300 hPa	-0.6922	0.5397	0.2340
500 hPa	-0.6491	0.4963	0.3382
700 hPa	-0.4529	0.4610	0.5824
Column	-0.7512	0.3830	0.3220

ticity (Figure 3.8c) is rotating around the trough, which is supporting a broken squall line that has developed from Dallas, TX, through Little Rock, AR with additional associated showers occur across the southern Great Lakes (Figure 3.8d). A second area of clouds is streaming into the Pacific northwest ahead of the next trough (Figure 3.8e).

Minimum and maximum ranges on model omega, term omega with sigma and term omega without sigma, vorticity advection, and thickness advection for April 4, 2011 are listed in Table 3.7. Figure 3.8 shows observations from the April 4, 2011 case study day: Panel a.) 300 hPa pressure level heights (geopotential meters) and shaded isotachs ranging from 30 ms^{-1} to 70 ms^{-1}. Panel b.) Surface mean sea level pressure (hPa) and shaded isentropes ranging from 240 k to 290 k. Panel c.) 500 hPa pressure level heights (geopotential meters) and shaded vorticity ranging from -2.0×10^{-4} s^{-1} to 4.0×10^{-4} s^{-1}. Panel d.) One hour rainfall accumulation mm hr^{-1} beginning at 18z. Panel e.) IR Satellite. Figure 3.9 compares the 300 hPa, 500 hPa, and 700 hPa levels for model omega (Panels a-c) and term omega without sigma (Panels d-f): Panel a.) 300 hPa pressure level. Panel b.) 500 hPa pressure level. Panel c.) 700 hPa pressure level shaded by model

derived omega at 4.0×10^{-1} ms^{-1} to -4.0×10^{-1} ms^{-1}. Panel d.) 300 hPa pressure level. Panel e.) 500 hPa pressure level. Panel f.) 700 hPa pressure level shaded by term omega calculated without sigma at 4.0×10^{-5} to -4.0×10^{-5} for April 4, 2011. Figure 3.10 displays the six panel contours for April 4, 2011: Panel a.) Contoured omega calculated with sigma at 4.0×10^{-3} ms^{-1}. Panel b.) Contoured vorticity advection at 4.2×10^{-9} rad s^{-2}. Panel c.) Contoured model derived omega at 20.0×10^{-2} ms^{-1}. Panel d.) Contoured omega calculated without sigma at 3.0×10^{-6}. Panel e.) Contoured thickness advection at 4.0×10^{-9} K s^{-1}. Panel f.) Contoured divergence at 5.0×10^{-2} s^{-1}. Each contour is colored by pressure (75-1000 hPa). Figure 3.11 shows upper level model omega and term omega: Panel a.) 200 hPa pressure level. Panel b.) 250 hPa pressure level shaded by model derived omega at 4.0×10^{-1} ms^{-1} to -4.0×10^{-1} ms^{-1}. Panel c.) 500 hPa pressure level shaded by divergence at -4.5×10^{-2} s^{-1} to 4.5×10^{-2} s^{-1}. Panel d.) 200 hPa pressure level. Panel e.) 250 hPa pressure level shaded by term omega calculated without sigma 4.0×10^{-5} to -4.0×10^{-5} for April 4, 2011.

Table 3.7

Minimum and maximum ranges for calculated variables for Apr. 4, 2011.

	Lower Bound	Upper Bound
Model Omega	-4.8×10^{-1} ms^{-1}	8.9×10^{-1} ms^{-1}
Term Omega without sigma	-9.6×10^{-6}	1.1×10^{-6}
Term Omega with sigma	-6.4×10^{-2} ms^{-1}	1.2×10^{-1} ms^{-1}
Vorticity Advection	-1.4×10^{-8} rad s^{-2}	1.7×10^{-8} rad s^{-2}
Thickness Advection	-1.3×10^{-8} K s^{-1}	1.4×10^{-8} K s^{-1}

Term omega without sigma (Figure 3.10d) shows strong upper level UVVs ahead of the trough axis. These are associated with a linear stretch of positive vorticity advection and are aligned with a QLCS that is pushing across the Ohio River valley and extends into eastern Texas (Figure 3.8d). Some lower level forcing is visible near Memphis, TN. Term omega also shows upward motion into the Great Lakes region that is associated with the baroclinic leaf of the developing trough. Term omega calculated with sigma (Figure 3.10a) shows noisy results over the mountain west but does show more wide spread forcing along the cold front. Particularly insightful is the placement of lower level UVVs ahead of the front. There are three discrete areas of low level vertical motion ahead of the front. One area is over the Mississippi Delta, a second across middle tennessee, and a third over southern Ohio. Compared to the IR satellite image (Figure 3.8e), each of the areas of low level vertical motion correspond to several areas of colder cloud tops (shown in indigo), signifying enhanced convection.

Vorticity advection (Figure 3.10b) and thickness advection (Figure 3.10e) agree on the placement of vertical motion; however, there is some cancelation directly behind the front, which is expected as correlation values between terms B and C remain high (Table 3.9). Thickness advection presents more widespread forcing across the Great Lakes, which is a result of moist inflow ahead of the system and is developing the baroclinic leaf structure. Otherwise, thickness advection and vorticity advection line up ahead of the upper level trough and along the 300 hPa level jet stream (Figure 3.8a).

Comparing the 2D pressure panels shows an interesting upper level structure to the vertical motion profile. Term omega (Figure 3.9d-f) shows limited upward vertical mo-

tion. The 300 hPa level (Figure 3.9d) shows more widespread downward vertical motion behind the front than upward motion ahead of the front. Model omega shows widespread vertical motion at the 300 hPa level (Figure 3.9a) and a similar situation for the 500 hPa (Figure 3.9b) and 700 hPa (Figure 3.9c) levels. Term omega only shows weak forcing behind the front. However, at higher levels term omega shows widespread vertical motion. At the 200 hPa level (Figure 3.11d) term omega shows strong vertical motion over Mississippi, Arkansas, and Tennessee, extending northeastward to the Great Lakes. Model omega shows little vertical motion at the 200 hPa level (Figure 3.11a). At 250 hPa term omega (Figure 3.11e) only shows slightly stronger UVVs that are still weaker than 300 hPa (Figure 3.10a). It is unknown why vertical motion shown by term omega is so strong at the 200 hPa level. For comparison, Figure 3.11c shows 500 hPa divergence. The most widespread 500 hPa convergence is beneath the largest area of 200 hPa UVVs. Winds are converging beneath the 200 hPa upward vertical motion maximum to replace mass that is being evacuated aloft. The upper level divergence (Figure 3.10f) is located above the strongest UVVs, corroborating the placement of vertical motion.

Two smaller areas of vertical motion are present over the mountain west. There is high agreement between term omega without sigma (Figure 3.10d) and model omega (Figure 3.10c) There is a widespread area of clouds over the mountain west, and rain is falling over the Puget Sound (Figure 3.8d).

Pearson's R correlations at 300 hPa, 500 hPa, 700 hPa, and the atmospheric column from 1000 hPa to 50 hPa for model omega to term omega with sigma and term omega without sigma for April 4, 2011 are shown in Table 3.8. Pearson's R correlations at 300

hPa, 500 hPa, 700 hPa, and the atmospheric column from 1000 hPa to 50 hPa for vorticity advection to thickness advection, vorticity advection to model omega, and thickness advection to model omega for April 4, 2011 are shown in Table 3.9. Correlations between term omega with sigma and model omega continue to be weak for April 4, 2011 (Table 3.8). The strongest correlation is at the 500 hPa level with 300 hPa, 700 hPa, and the volume an order of magnitude weaker. The 500 hPa level also has the strong correlation between term omega calculated without sigma and model omega. The weakest is at the 300 hPa level while 700 hPa and the volume correlations are of the same magnitude as 500 hPa.

Table 3.8

Correlations for model omega to term omega for Apr. 4, 2011.

	With Sigma	Without Sigma
300 hPa	0.0002	0.0668
500 hPa	0.0068	0.2595
700 hPa	0.0004	0.1509
Column	0.0006	0.1010

3.1.4 May 12, 2011

A series of low pressure systems embedded in otherwise weak upper-level flow is transiting across the continental United States (Figure 3.12a). One system has pushed off the east coast, with a second system centered over the midwest and a third system developing over the Canadian maritime. Only the system over the midwestern states is

a.) 300 hPa

c.) 500 hPa

b.) Surface

d.) Radar

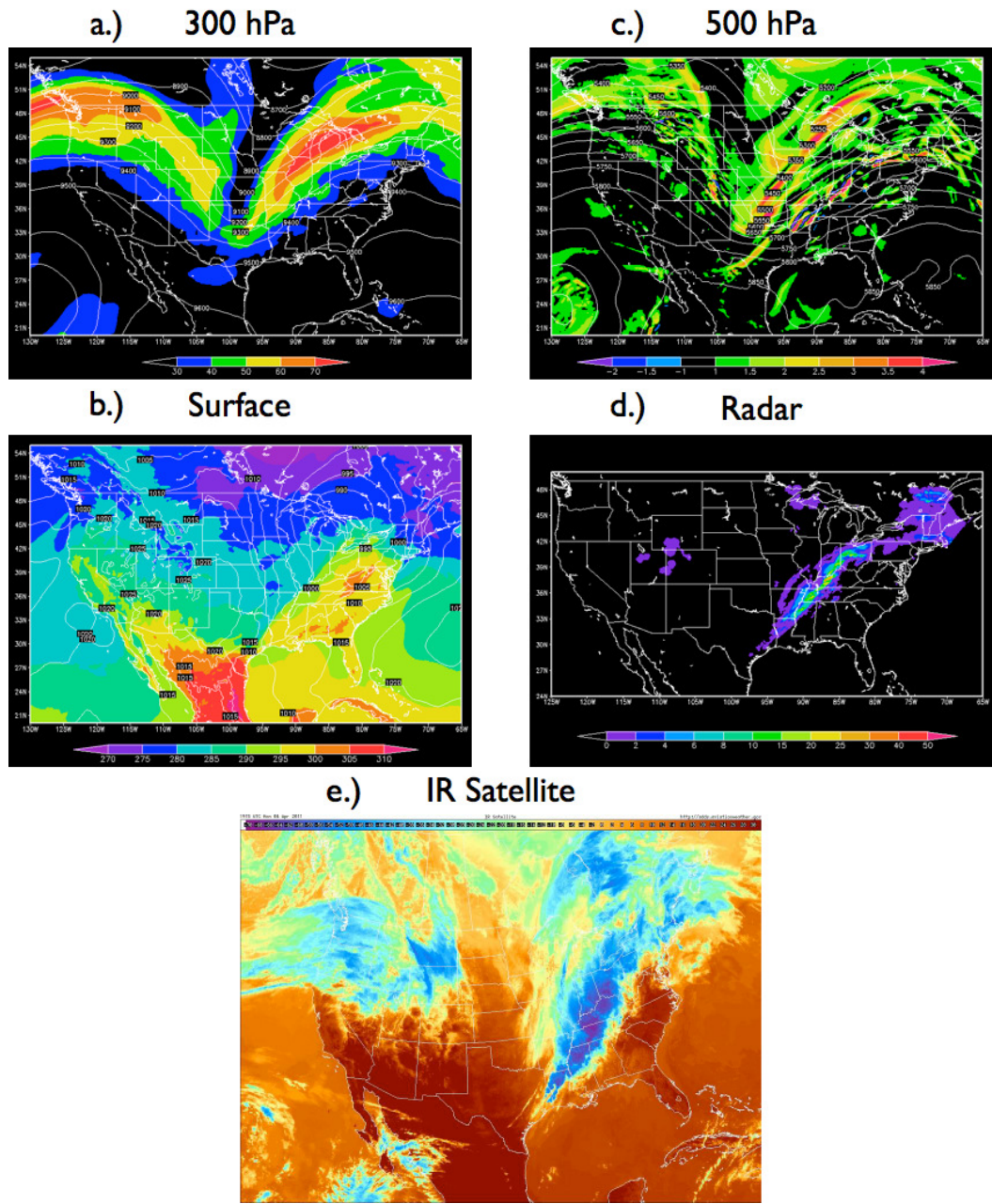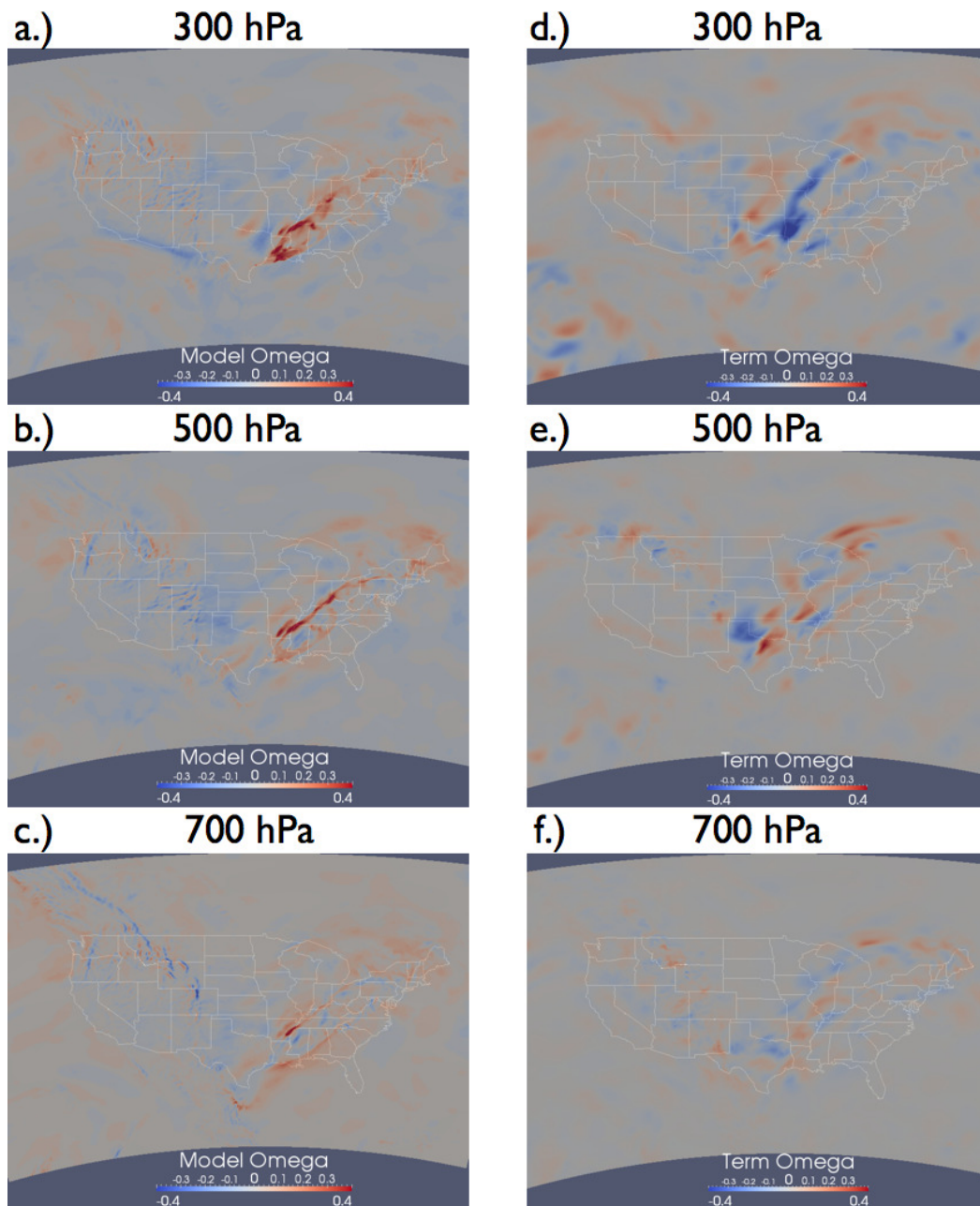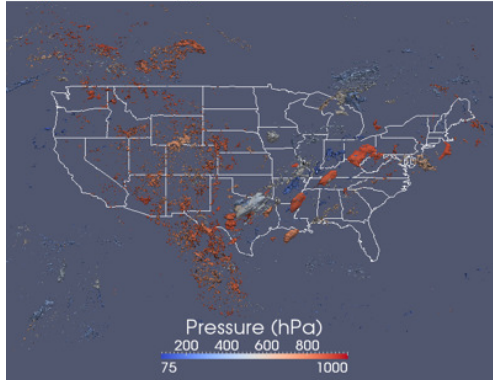e.) IR Satellite

Figure 3.8

April 4, 2011 18z observations

Figure 3.9

Isobars shaded by model omega or term omega without sigma on Apr. 4, 2011

a.) Omega with Sigma   d.) Omega without Sigma
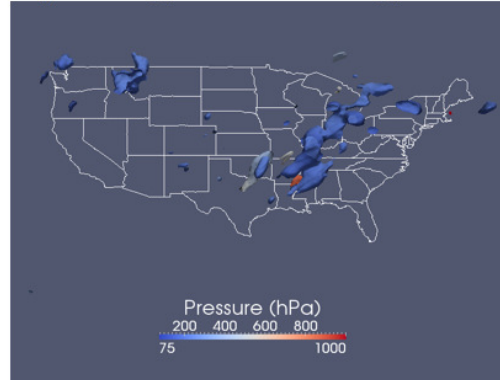
b.) Vorticity Advection   e.) Thickness Advection
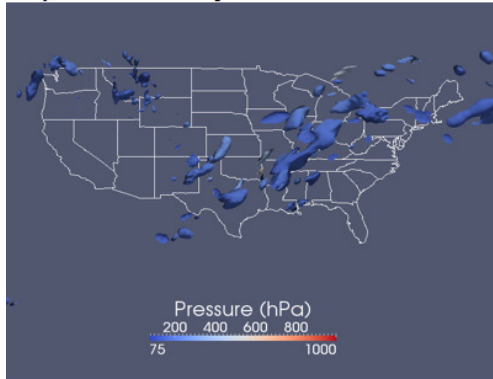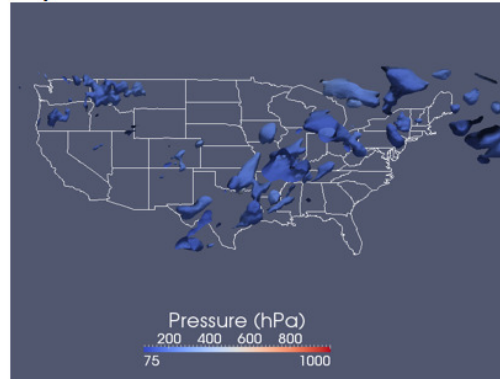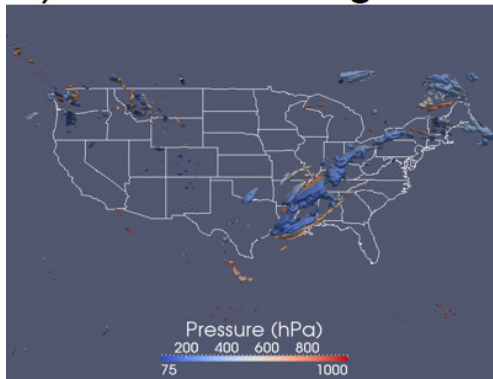
c.) Model Omega   f.) Divergence
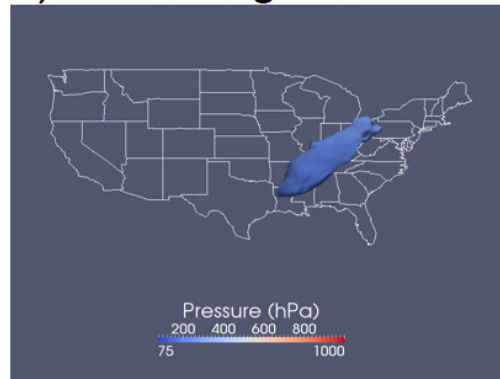
Figure 3.10

Six panel contours for April 4, 2011.
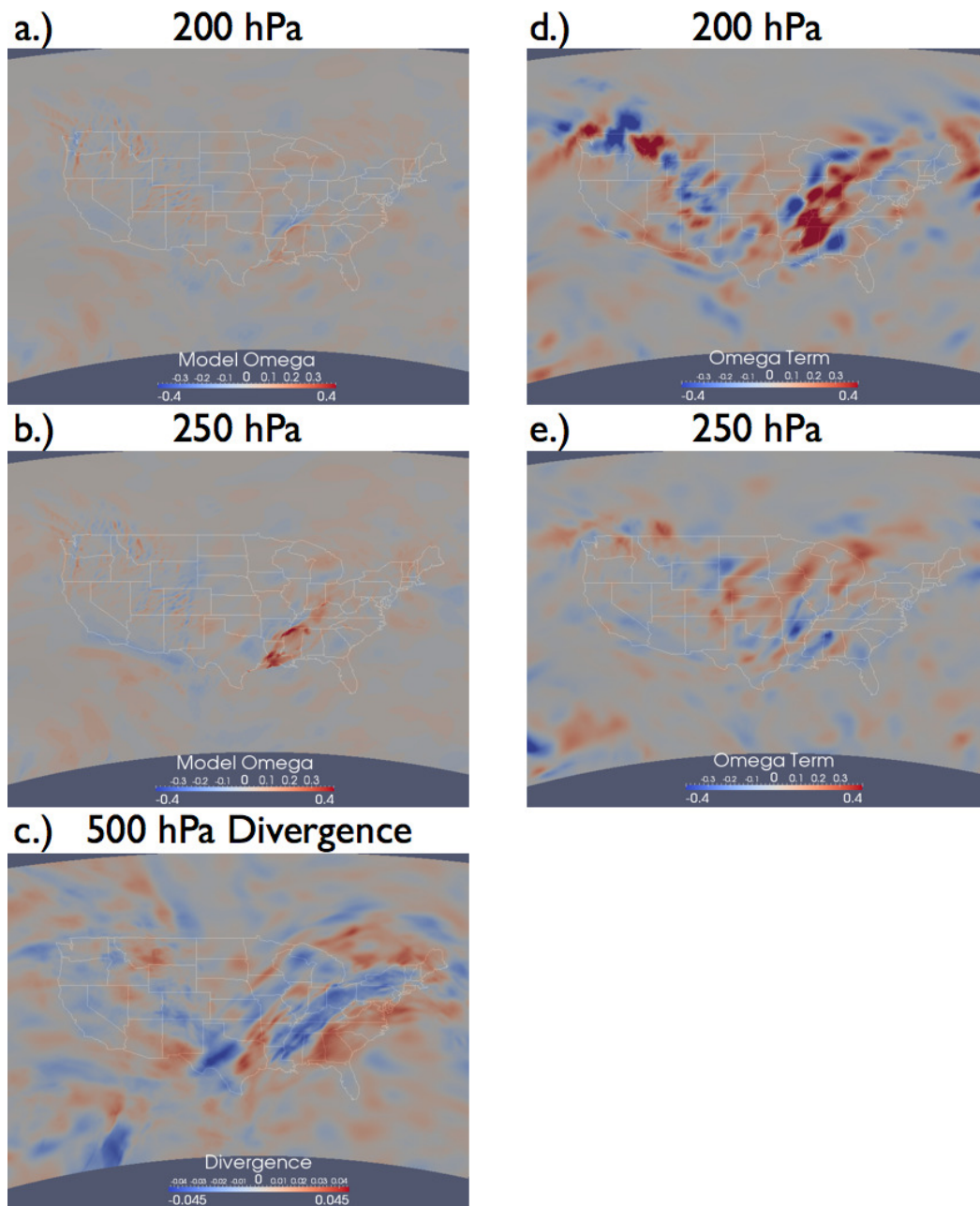
Figure 3.11

Upper level model omega and term omega for April 4, 2011

Table 3.9

Correlations between terms for Apr. 4, 2011.

	Vorticity Advection to Thickness Advection	Vorticity Advection to Model Omega	Thickness Advection to Model Omega
300 hPa	-0.7682	0.5116	0.1571
500 hPa	-0.5824	0.5802	0.3242
700 hPa	-0.6826	0.3569	0.4391
Column	-0.7288	0.4214	0.3138

bringing any organized areas of activity. A large complex of storms is pushing through Texas toward the Gulf of Mexico and is associated with the cold front trailing the low over Nebraska (Figure 3.8d). A second large swath of rain falls from Denver, CO through South Dakota to central Minnesota, which is associated with the upper level low pressure centered over the Kansas, Nebraska, Colorado border. This system is primarily driven by a vorticity maximum over Kansas (Figure 3.8c) and strong surface warm air advection (Figure 3.8b) as the upper level flow is weak (Figure 3.8a).

Minimum and maximum ranges on model omega, term omega with sigma and term omega without sigma, vorticity advection, and thickness advection for May 12, 2011 are listed in Table 3.10. Figure 3.12 shows observations from the May 12, 2011 case study day: Panel a.) 300 hPa pressure level heights (geopotential meters) and shaded isotachs ranging from 30 ms^{-1} to 70 ms^{-1}. Panel b.) Surface mean sea level pressure (hPa) and shaded isentropes ranging from 240 k to 290 k. Panel c.) 500 hPa pressure level heights (geopotential meters) and shaded vorticity ranging from -2.0×10^{-4} s^{-1} to 4.0×10^{-4} s^{-1}. Panel d.) One hour rainfall accumulation mm hr^{-1} beginning at 18z. Panel e.) IR Satellite.

Figure 3.14 compares the 300 hPa, 500 hPa, and 700 hPa levels for model omega (Panels a-c) and term omega without sigma (Panels d-f): Panel a.) 300 hPa pressure level. Panel b.) 500 hPa pressure level. Panel c.) 700 hPa pressure level shaded by model derived omega at 3.5×10^{-1} ms^{-1} to -3.5×10^{-1} ms^{-1}. Panel d.) 300 hPa pressure level. Panel e.) 500 hPa pressure level. Panel f.) 700 hPa pressure level shaded by term omega calculated without sigma at 3.5×10^{-5} to -3.5×10^{-5} for May 12, 2011. Figure 3.15 displays the six panel contours for May 12, 2011: Panel a.) Contoured omega calculated with sigma at 1.5×10^{-3} ms^{-1}. Panel b.) Contoured vorticity advection at 2.0×10^{-9} rad s^{-2}. Panel c.) Contoured model derived omega at 7.0×10^{-2} ms^{-1}. Panel d.) Contoured omega calculated without sigma at 1.5×10^{-6}. Panel e.) Contoured thickness advection at 2.0×10^{-9} K s^{-1}. Panel f.) Contoured divergence at 3.0×10^{-2} s^{-1}. Each contour is colored by pressure (75-1000 hPa). Figure 3.16 shows downward velocities and convergence for May 12, 2011: Contoured negative omega calculated without sigma at -1.9×10^{-6}. Contoured negative model derived omega at 2.5×10^{-2} ms^{-1}. Contoured convergence at -2.5×10^{-2} s^{-1} for May 12, 2011. Each contour is colored by pressure (75-1000 hPa). Figure 3.17 shows term omega calculated with sigma (ms^{-1}): Panel a.) May 300 hPa pressure level 2.0×10^{-3} to -2.0×10^{-3}. Panel b.) May 700 hPa pressure level 2.0×10^{-3} to -2.0×10^{-3}. Panel c.) August 300 hPa pressure level 2.5×10^{-3} to -2.5×10^{-3}. Panel d.) August 500 hPa pressure level 2.5×10^{-3} to -2.5×10^{-3}. Panel e.) December 300 hPa pressure level 3.5×10^{-3} to -3.5×10^{-3}. Panel f.) December 500 hPa pressure level 3.5×10^{-3} to -3.5×10^{-3}.

Table 3.10

Minimum and maximum ranges for calculated variables for May 12, 2011.

	Lower Bound	Upper Bound
Model Omega	-6.2×10^{-1} ms^{-1}	7.6×10^{-1} ms^{-1}
Term Omega without sigma	-6.7×10^{-6}	1.2×10^{-5}
Term Omega with sigma	-1.3×10^{-2} ms^{-1}	3.6×10^{-1} ms^{-1}
Vorticity Advection	-1.0×10^{-8} rad s^{-2}	1.2×10^{-8} rad s^{-2}
Thickness Advection	-7.9×10^{-9} K s^{-1}	1.1×10^{-8} K s^{-1}

For May 12, 2011, two large areas of precipitation are falling. One area is associated with an upper level low centered over Colorado. Term omega distinctly shows the center of the low as strong vertical motion (Figure 3.14d) on the 300 hPa pressure level. Further UVVs are shown through South Dakota where the greatest precipitation extends. Model omega (Figure 3.14a) only shows vertical motion through South Dakota but little directly associated with the low in Colorado. At 500 hPa, model omega (Figure 3.14b) continues to be strong, but term omega (Figure 3.14e) quickly diminishes, showing downward velocities in Nebraska. At the 700 hPa level, orographic effects dominate model omega (Figure 3.14e), but term omega (Figure 3.14f) shows weak upward motion, suggesting convergence between the 700 hPa and 500 hPa. This is shown in Figure 3.16c with convergence over Nebraska between 600-700 hPa as well as downward velocities with term omega. Model omega lacks these features, showing a tendency towards isolating individual thunderstorms.

As would be expected, vorticity advection (Figure 3.15b) is the predominant forcing feature with the upper low itself (compared to 500 hPa observed vorticity, Figure 3.12c,

which shows the highest vorticity collocated with the calculated vorticity advection), while thickness advection (Figure 3.15e) is more widespread ahead of the forcing aloft due to lower level warm air advection (Figure 3.12b).

The second area of convection pushes to the southeast over Texas, towards the Gulf of Mexico. Model omega places upward motion off the coast of Texas (Figure 3.15c), while radar imagery (Figure 3.12d) shows the QLCS still west of Houston, TX. Model omega has upward vertical velocities at all levels (Figure 3.14a-c), but they are placed too far east. At 700 hPa, model omega (Figure 3.14c) shows strong downward vertical velocities just ahead of bowing segment, whereas term omega (Figure 3.14f) shows forcing in a more representative area than model omega when compared to rainfall estimates. While model omega shows more concentrated and linear vertical velocities, the placement is many hundreds of miles southeastward. Term omega shows weaker forcing but does give correct placement. This is a result of dynamic forcing elements in the upper levels over Texas. Though vorticity advection (Figure 3.15b) and thickness advection (Figure 3.15e) are separately weak over Texas, their combination is cumulative in this region (e.g. vorticity advection and thickness advection are working together instead of canceling each other [Table 3.12]). This is as demonstrated by strong divergence in the upper-levels over Texas (Figure 3.15f). Mass is being evacuated over southeastern Texas and vertical velocities are upward to fill in lowered heights.

Term omega calculated with sigma shows an odd feature at the 700 hPa level (Figure 3.17d). A large swath of upward vertical velocities exists over eastern Kansas and central Nebraska. At the upper levels, there is a distinct lack of upward vertical motion

over Kansas though central Nebraska. The strongest dynamic forcing is associated with the precipitation over the Dakotas (Figure 3.17a). However, this feature is not collocated with any radar returns (Figure 3.12d). What this feature might suggest is confined forcing beneath a cap that could soon develop. This theory is corroborated by rainfall estimates from approximately six hours ahead of the analyzed time step. A large area of discrete thunderstorms has developed over eastern Nebraska, Kansas, and eastern Oklahoma (Figure 3.13). Term omega calculated with sigma could show areas where the boundary layer is capped.

Pearson's R correlations at 300 hPa, 500 hPa, 700 hPa, and the atmospheric column from 1000 hPa to 50 hPa for model omega to term omega with sigma and term omega without sigma for May 12, 2011 are shown in Table 3.11. Pearson's R correlations at 300 hPa, 500 hPa, 700 hPa, and the atmospheric column from 1000 hPa to 50 hPa for vorticity advection to thickness advection, vorticity advection to model omega, and thickness advection to model omega for May 12, 2011 are shown in Table 3.12. The correlations between term omega calculated with sigma and model omega vary considerably (Table 3.11). The strongest correlation is at the 500 hPa level, while the 300 hPa level is correlated two orders of magnitude smaller. The 700 hPa level is correlated negatively. As a result, the correlation throughout the entire column is small, on the order of 10^{-6}. Term omega calculated without sigma is of similar magnitude to other study days with correlations for each level on the order 10^{-1}.

Table 3.11

Correlations for model omega to term omega for May 12, 2011.

	With Sigma	Without Sigma
300 hPa	0.0002	0.2461
500 hPa	0.0150	0.3286
700 hPa	-0.0032	0.2216
Column	0.000002	0.1477

Table 3.12

Correlations between terms for May 12, 2011.

	Vorticity Advection to Thickness Advection	Vorticity Advection to Model Omega	Thickness Advection to Model Omega
300 hPa	-0.6884	0.4804	0.3054
500 hPa	-0.4990	0.4984	0.5026
700 hPa	-0.5043	0.5007	0.4949
Column	-0.6571	0.4709	0.3557

a.) 300 hPa   c.) 500 hPa

b.) Surface   d.) Radar

e.) IR Satellite
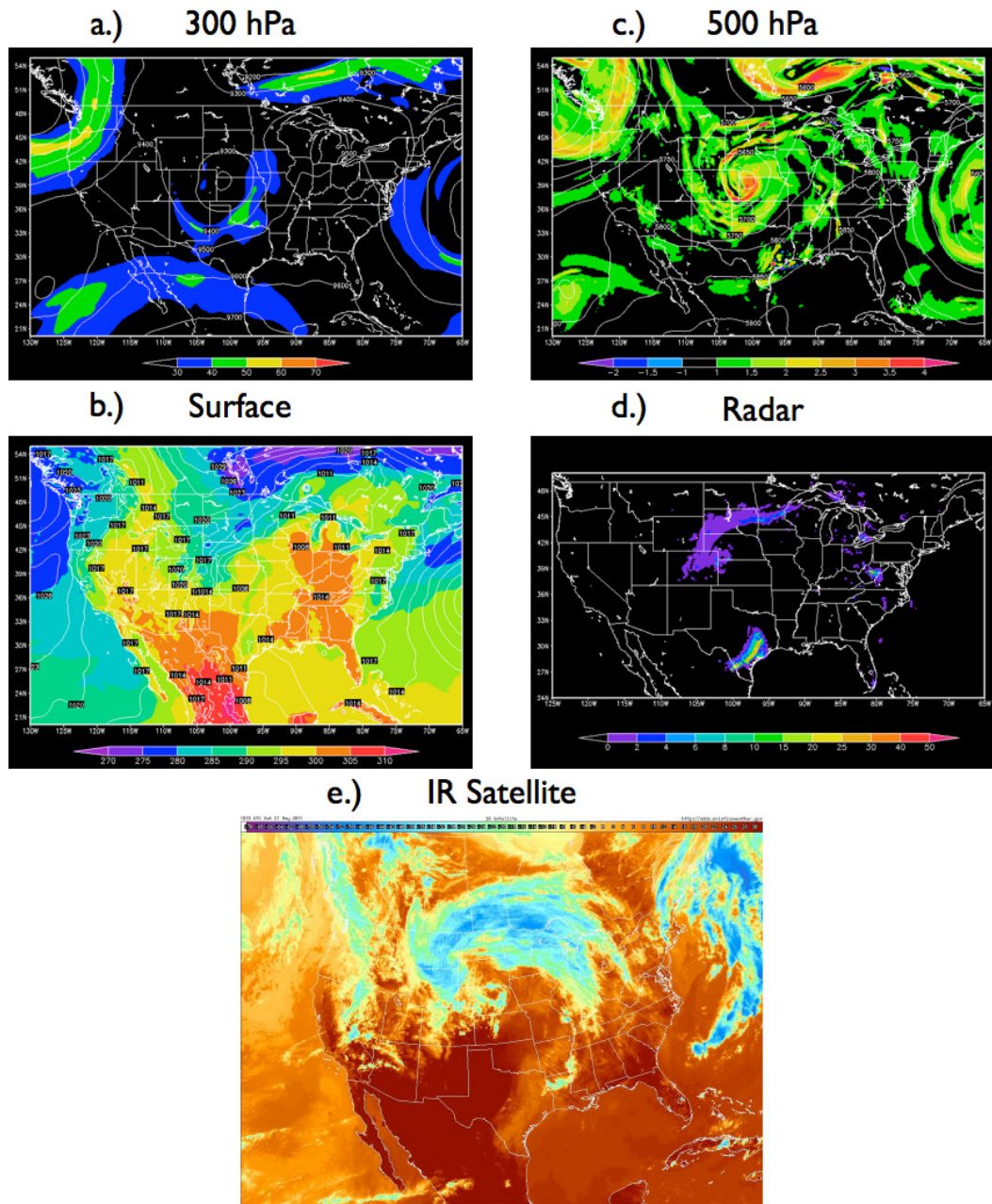
Figure 3.12

May 12, 2011 18z observations
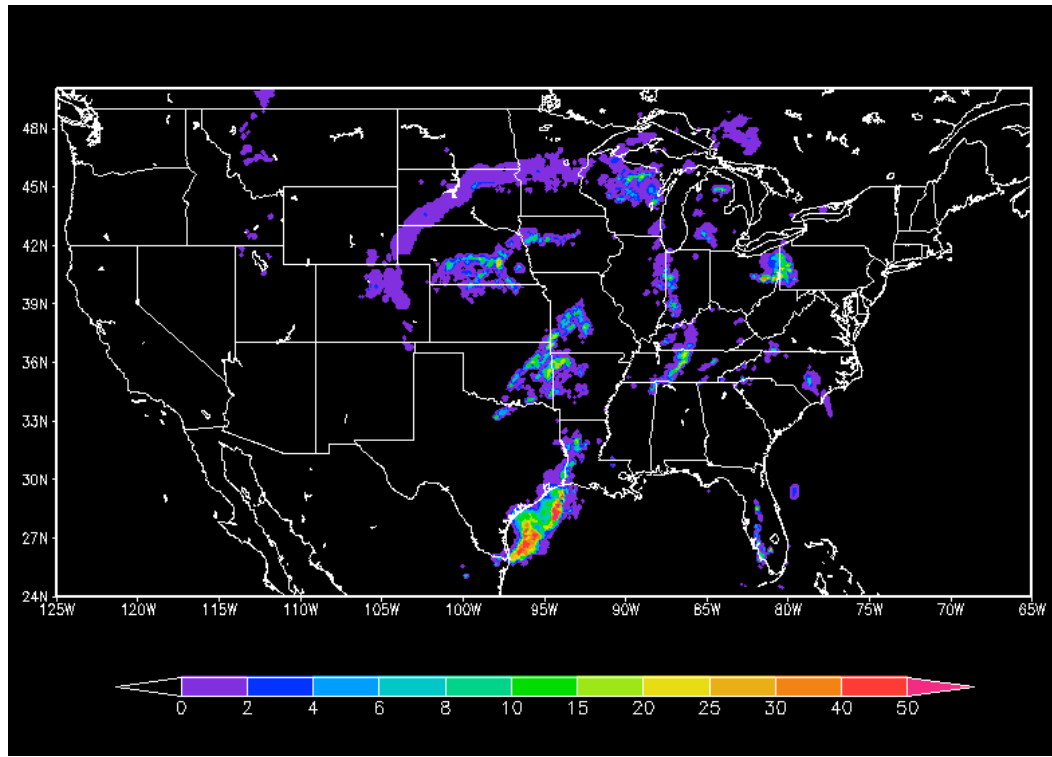
Figure 3.13

Rainfall accumulation (mm hr^{-1}) for 0z May 13, 2011.
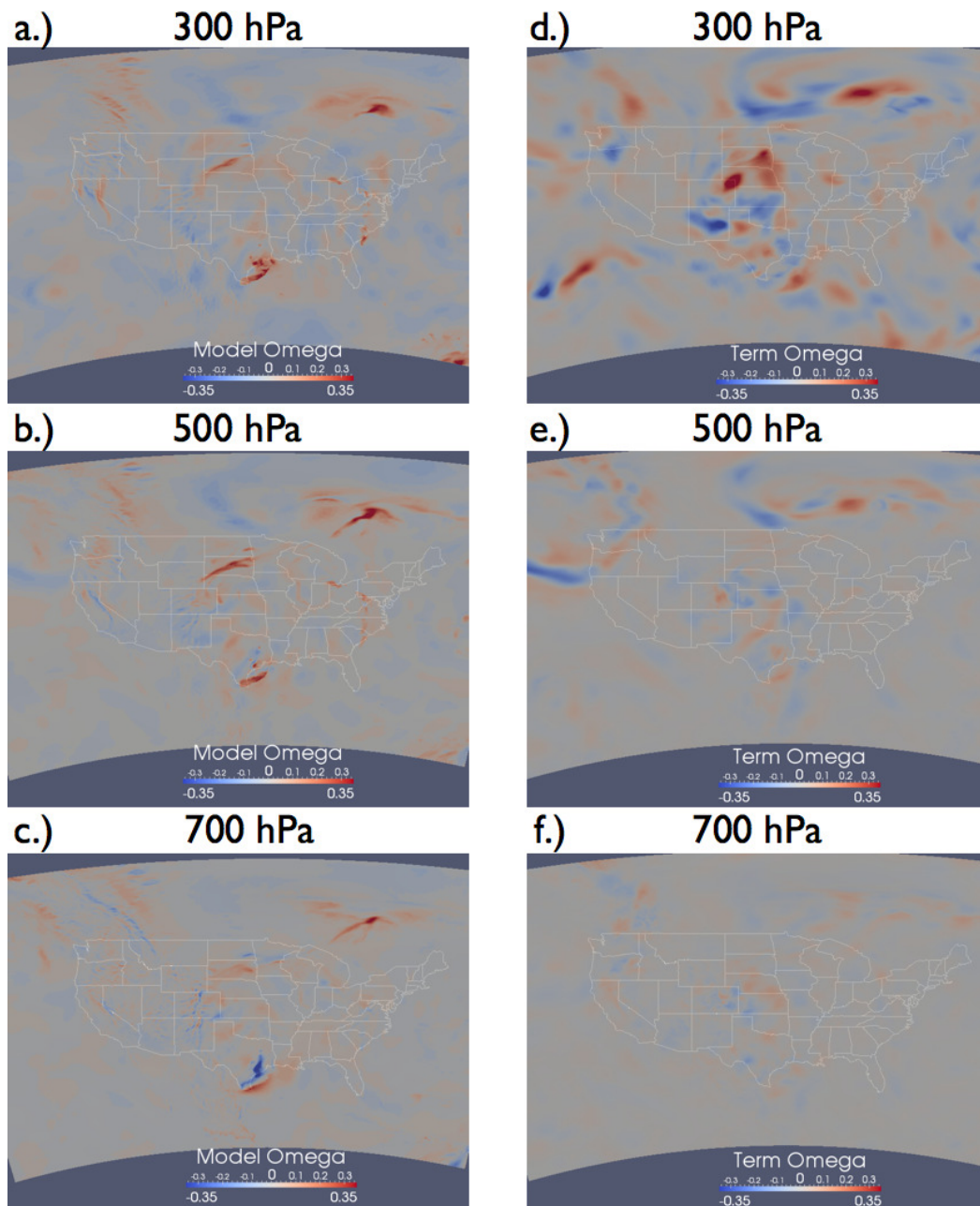
Figure 3.14

Isobars shaded by model omega or term omega without sigma on May 12, 2011

a.) Omega with Sigma
Pressure (hPa)
200 400 600 800
75 1000
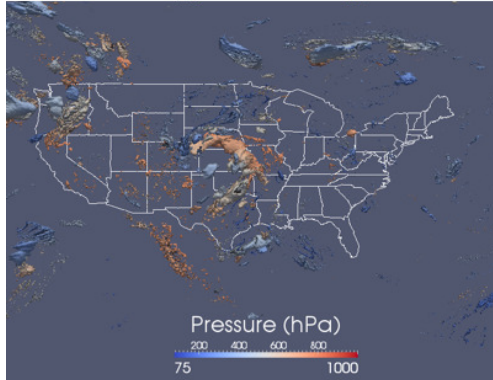
d.) Omega without Sigma
Pressure (hPa)
200 400 600 800
75 1000

b.) Vorticity Advection
Pressure (hPa)
200 400 600 800
75 1000

e.) Thickness Advection
Pressure (hPa)
200 400 600 800
75 1000

c.) Model Omega
Pressure (hPa)
200 400 600 800
75 1000
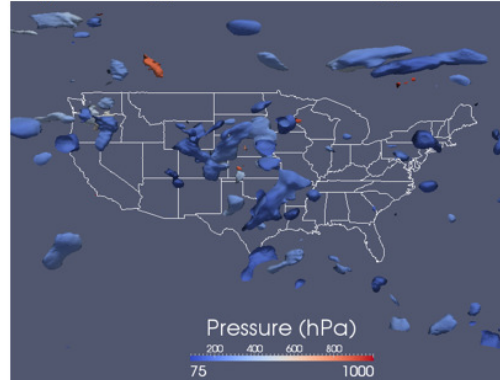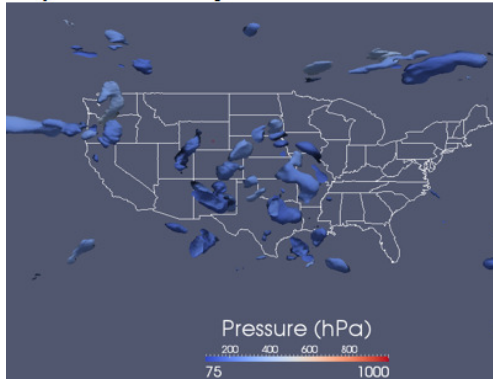
f.) Divergence
Pressure (hPa)
200 400 600 800
75 1000
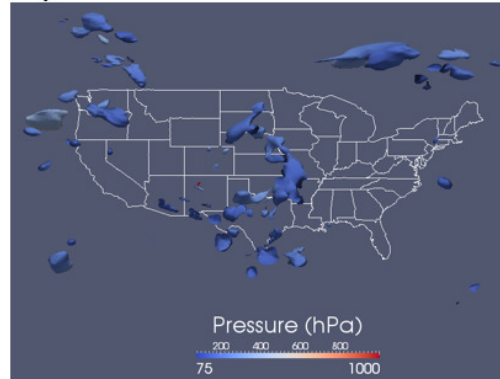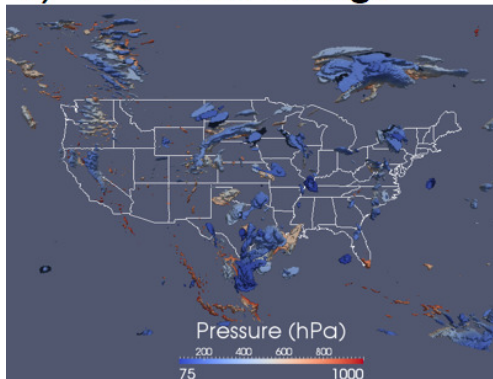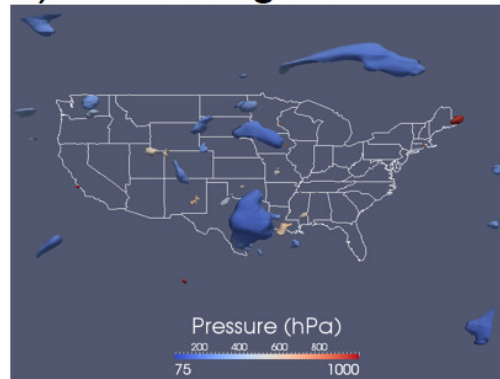
Figure 3.15

Six panel contours for May 12, 2011.

77

a.) Negative Omega without Sigma
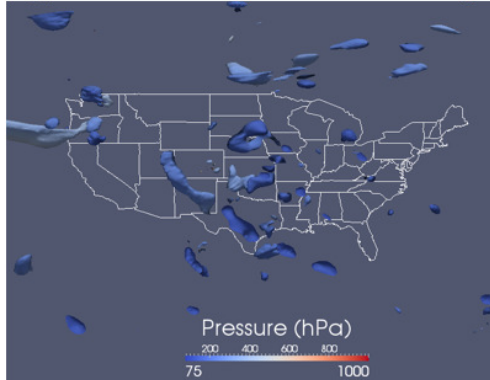
b.) Negative Model Omega
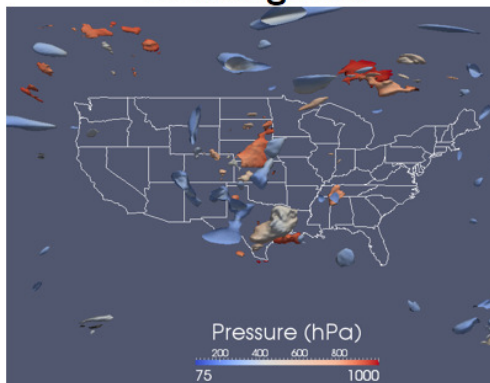
c.) Convergence

Figure 3.16

Three panel downward velocities and convergence for May 12, 2011.
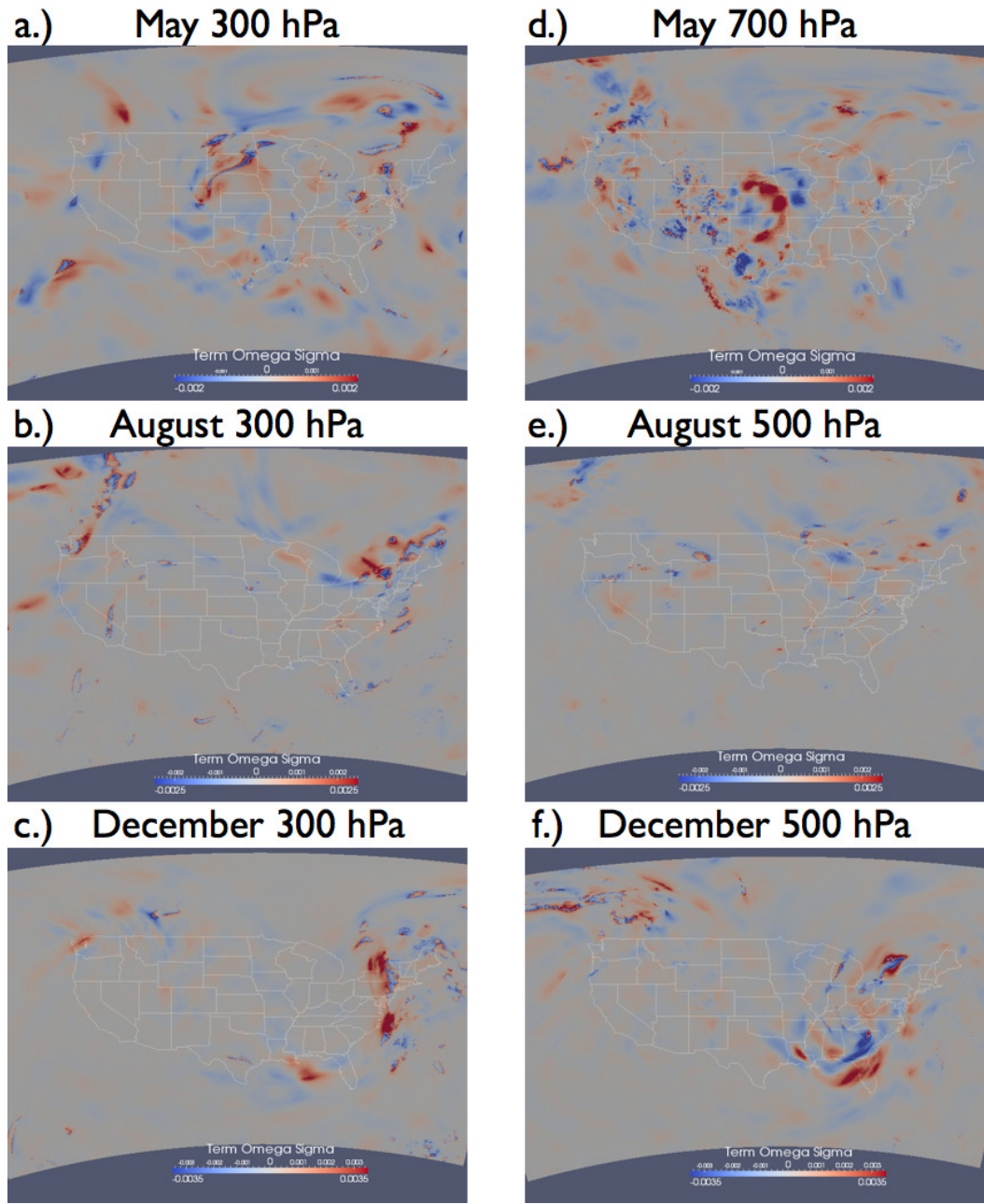
Figure 3.17

Term omega calculated with sigma (ms^{-1}) for May, August, and December.

3.1.5 July 17, 2011

An extensive ridge, buoyed by warm air, has built into the midwest and eastern US, while a weak upper level trough stagnates off the Northwestern US coast (Figure 3.18a). Weak areas of positive vorticity are rotating around the center of the western upper level low and are the impetus for clouds and showers over the Pacific Northwest (Figure 3.18c). An area of strong storms and rain prevails over the Dakotas as a piece of vorticity energy is ejected from the western low and rotates north of the midwestern high. Numerous thunderstorms have developed with daytime heating across the Deep South, predominately off the Mississippi and Alabama coasts (Figure 3.8d).

Minimum and maximum ranges on model omega, term omega with sigma and term omega without sigma, vorticity advection, and thickness advection for July 17, 2011 are listed in Table 3.13. Figure 3.18 shows observations from the July 17, 2011 case study day: Panel a.) 300 hPa pressure level heights (geopotential meters) and shaded isotachs ranging from 30 ms^{-1} to 70 ms^{-1}. Panel b.) Surface mean sea level pressure (hPa) and shaded isentropes ranging from 255 k to 300 k. Panel c.) 500 hPa pressure level heights (geopotential meters) and shaded vorticity ranging from -2.0×10^{-4} s^{-1} to 4.0×10^{-4} s^{-1}. Panel d.) One hour rainfall accumulation mm hr^{-1} beginning at 18z. Panel e.) IR Satellite. Figure 3.19 compares the 300 hPa, 500 hPa, and 700 hPa levels for model omega (Panels a-c) and term omega without sigma (Panels d-f): Panel a.) 300 hPa pressure level. Panel b.) 500 hPa pressure level. Panel c.) 700 hPa pressure level shaded by model derived omega at 4.0×10^{-1} ms^{-1} to -4.0×10^{-1} ms^{-1}. Panel d.) 300 hPa pressure level. Panel e.) 500 hPa pressure level. Panel f.) 700 hPa pressure level shaded by term omega calculated

without sigma at 4.0×10^{-5} to -4.0×10^{-5} for July 17, 2011. Figure 3.20 displays the

six panel contours for July 17, 2011: Panel a.) Contoured term omega calculated with

sigma at 3.0×10^{-3} ms^{-1}. Panel b.) Contoured vorticity advection at 1.5×10^{-9} rad s^{-2}.

Panel c.) Contoured model derived omega at 15.0×10^{-2} ms^{-1}. Panel d.) Contoured term

omega calculated without sigma at 1.6×10^{-6}. Panel e.) Contoured thickness advection

at 1.5×10^{-9} K s^{-1}. Panel f.) Contoured divergence at 2.0×10^{-2} s^{-1}. Each contour is

colored by pressure (75-1000 hPa). Figure 3.21a shows contoured term omega calculated

with sigma with boundary layer included at 3.0×10^{-3} ms^{-1} for July 17, 2011.

Table 3.13

Minimum and maximum ranges for calculated variables for Jul. 17, 2011.

	Lower Bound	Upper Bound
Model Omega	-5.0×10^{-1} ms^{-1}	1.1×10^{-1} ms^{-1}
Term Omega without sigma	-8.2×10^{-5}	6.3×10^{-6}
Term Omega with sigma	-1.4×10^{-1} ms^{-1}	2.7×10^{-2} ms^{-1}
Vorticity Advection	-9.4×10^{-9} rad s^{-2}	1.2×10^{-8} rad s^{-2}
Thickness Advection	-1.4×10^{-8} K s^{-1}	1.2×10^{-9} K s^{-1}

A climatological normal summer pattern with a strong high pressure system is the over-

riding factor for July 17, 2011. As this is a thermodynamically driven environment, term

omega has difficulty pinpointing organized areas of uplift (Figure 3.20d); however, there

are few areas of observed convection. Though model omega shows more discrete updrafts,

the placement of updrafts does not coincide with the location of convection as compared to

satellite and radar imagery (Figure 3.18d,e). For example, the convection along the Gulf

Coast does not line up with vertical motion from either model omega (Figure 3.20c) or term omega (Figure 3.20d), though there is divergence aloft (Figure 3.20f). Model omega also shows updrafts at the North Dakota, South Dakota, Minnesota border; however, the strongest convection is several hundred miles to the northwest. Term omega shows strong low level upward motion but does not show upper level motion over the northern Great Plains. As expected, term omega shows the largest areas of uplift associated with the strongest dynamical forcing feature, a weak trough off the Pacific Northwest.

Comparing the pressure panels (Figure 3.19a-f), term omega shows the strongest area of vertical motion to be associated with strong vorticity advection at 300 hPa (Figure 3.19c) over the eastern Pacific Ocean. An area of uplift is shown over the California, Oregon border; however the strongest convection is further north into Oregon (Figure 3.18). At the lower levels term omega (Figure 3.19f) shows little vertical movement. Model omega strongly shows thermodynamically driven convection, but as noted before, the locations of convective complexes are not correct.

Term omega poorly handles a thermodynamically driven day. Term omega calculated with sigma (Figure 3.19a) shows little vertical motion over the eastern US but does show some elevated UVVs over the western US. The lack of UVVs over the eastern US can be attributed to the thermodynamic nature of the atmosphere. If the boundary layer is added to the image (Figure 3.21a), individual patches of vertical motion abound. By not including the boundary layer, none of the scattered, summertime convection is depicted over the eastern US, which is to be expected as air mass thunderstorms are driven by the boundary layer. However, term omega calculated with sigma over represents the coverage of

thunderstorms though several individual areas are well depicted, Minnesota for example. Model omega depicts a more realistic environment though convection placement is poor. As term omega without sigma does not factor in thermodynamics, vertical motion driven by non-dynamic process is represented poorly.

Pearson's R correlations at 300 hPa, 500 hPa, 700 hPa, and the atmospheric column from 1000 hPa to 50 hPa for model omega to term omega with sigma and term omega without sigma for July 17, 2011 are shown in Table 3.14. Pearson's R correlations at 300 hPa, 500 hPa, 700 hPa, and the atmospheric column from 1000 hPa to 50 hPa for vorticity advection to thickness advection, vorticity advection to model omega, and thickness advection to model omega for July 17, 2011 are shown in Table 3.15. For July, the 500 hPa level has the weakest correlation between term omega calculated with sigma to model omega (Table 3.14). The 300 hPa and 700 hPa levels are an order of magnitude stronger. The column correlation is quite weak, two orders of magnitude less. Term omega calculated without sigma along the pressure levels is on the order of 10^{-1}, while the correlation for the entire atmospheric column is of the order 10^{-2}.

Table 3.14

Correlations for model omega to term omega for Jul. 17, 2011.

	With Sigma	Without Sigma
300 hPa	0.0034	0.1554
500 hPa	0.0007	0.1898
700 hPa	0.0094	0.1605
Column	0.00007	0.0858

83
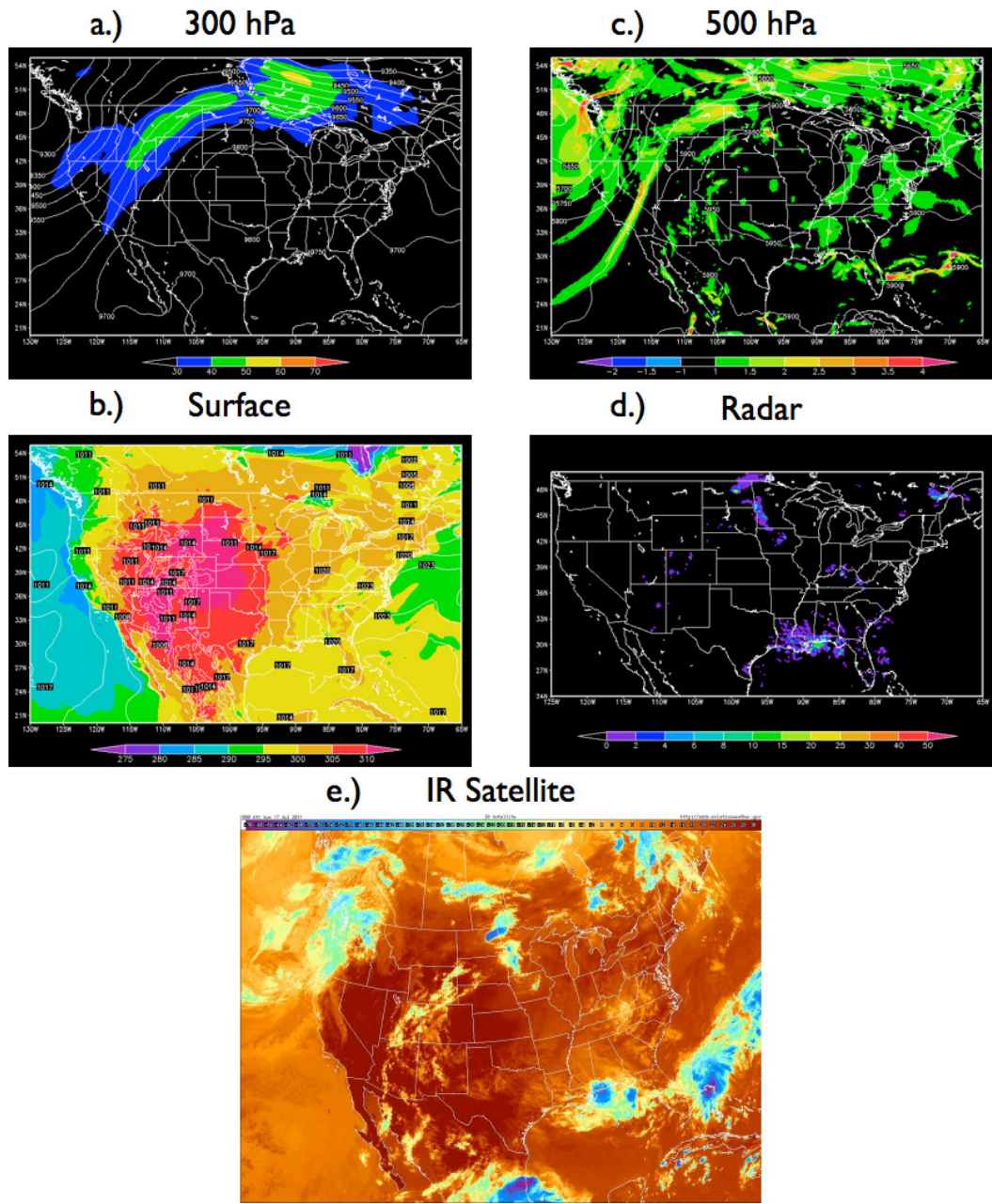
Figure 3.18

July 17, 2011 18z observations
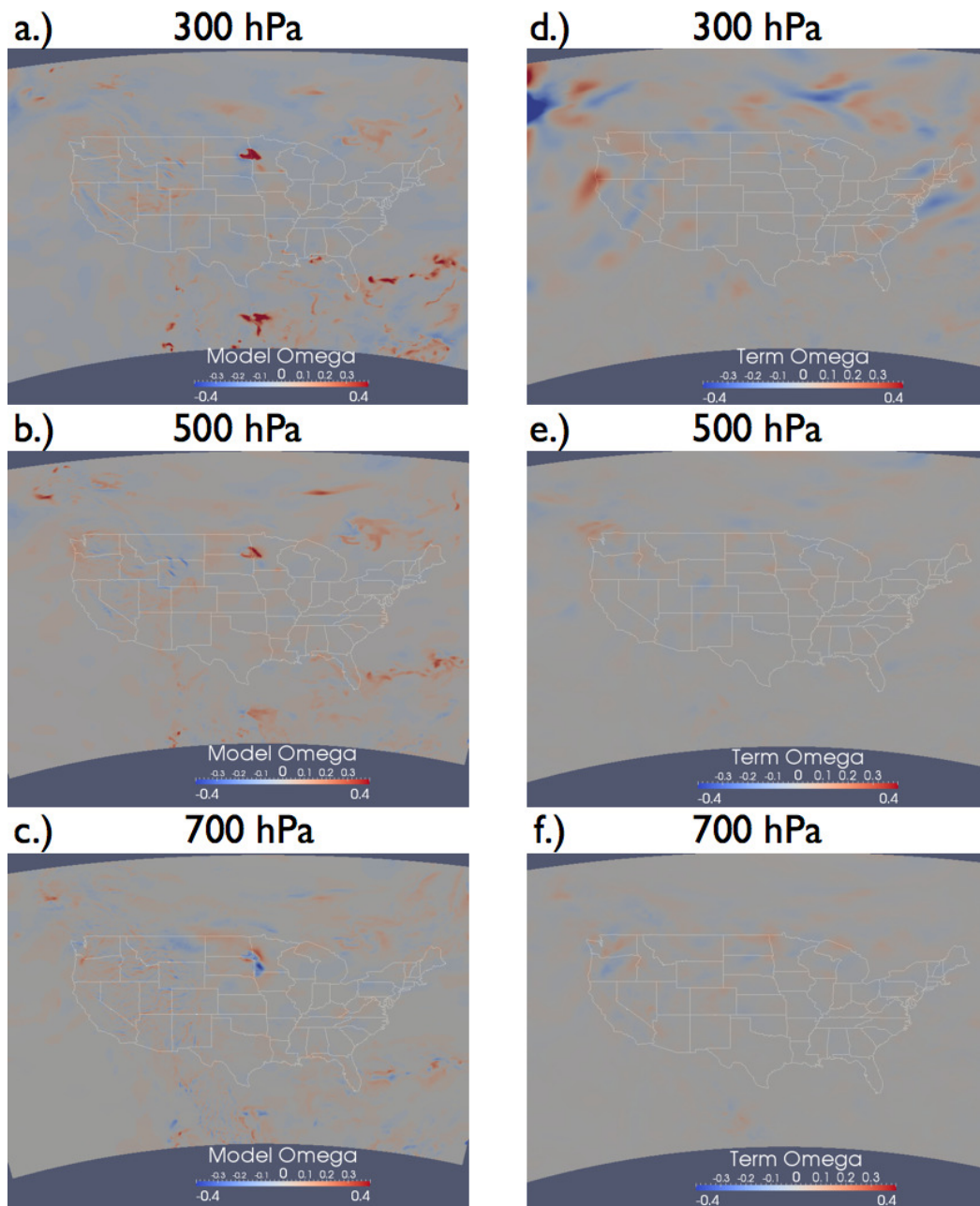
Figure 3.19

Isobars shaded by model omega or term omega without sigma on Jul. 17, 2011
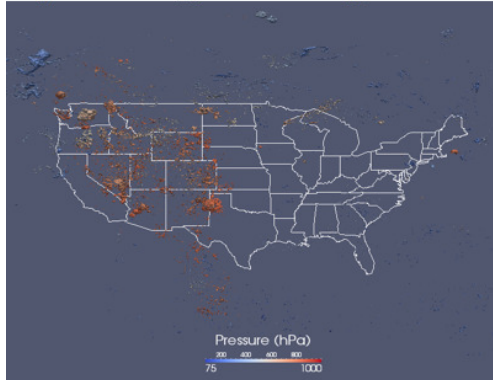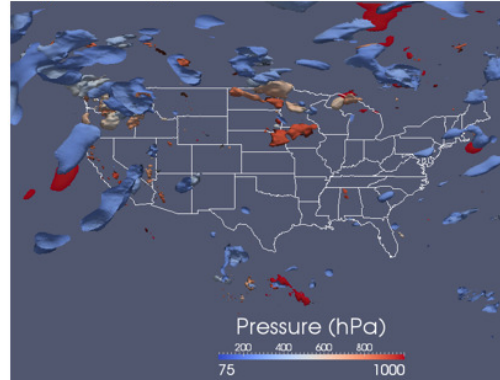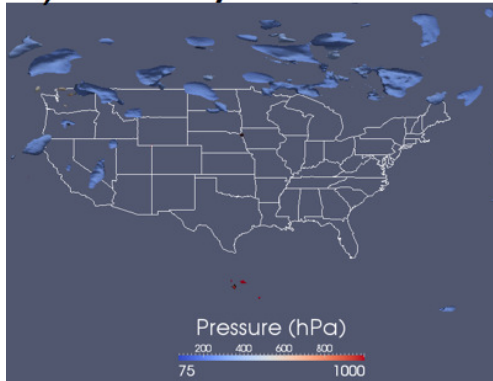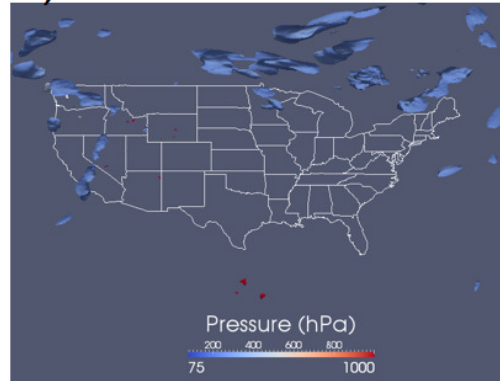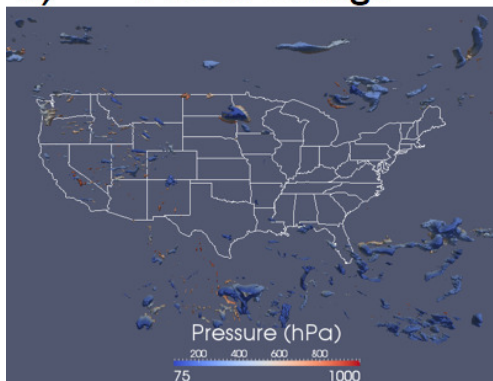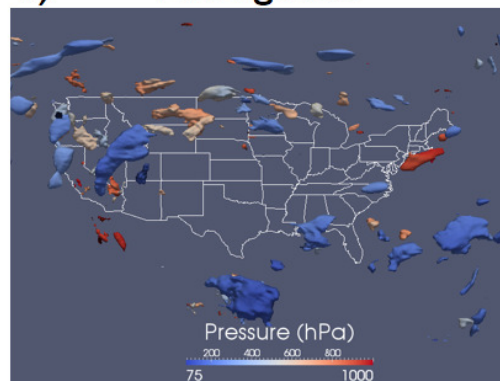
Figure 3.20

Six panel contours for July 17, 2011.

Table 3.15

Correlations between terms for Jul. 17, 2011.

	Vorticity Advection to Thickness Advection	Vorticity Advection to Model Omega	Thickness Advection to Model Omega
300 hPa	-0.5711	0.5432	0.3790
500 hPa	-0.7340	0.4213	0.3067
700 hPa	-0.5059	0.4962	0.4979
Column	-0.7190	0.4649	0.2812
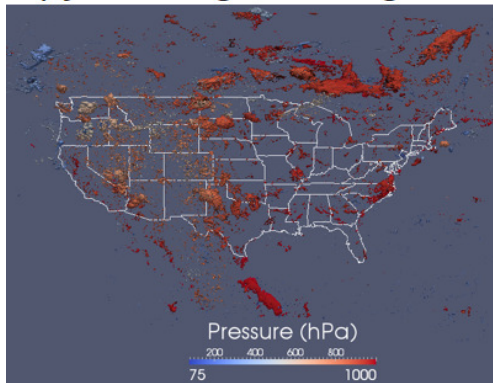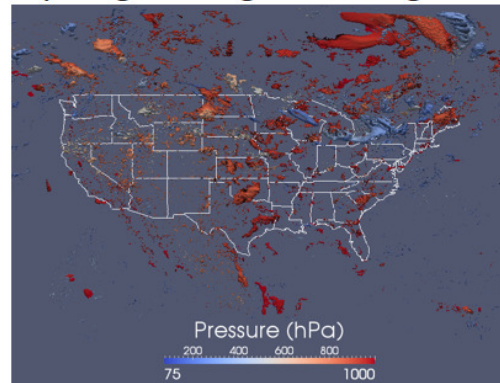
Figure 3.21

Contoured term omega with sigma with boundary layer for July and August

3.1.6 August 21, 2011

The country is held in a slightly amplified pattern with a moderate trough across eastern Canada that is influencing the pattern across the Northeast and a ridge across the western US. Scattered, thermodynamically driven areas of cloud cover and showers extend around the edge of the trough, from Oklahoma through the ArkLaTex and along the Florida panhandle (Figure 3.22d). More organized areas of showers and storms exist over the eastern Great Lakes and through Pennsylvania to Vermont that are a result of a jet streak (Figure 3.22a) and a longitudinally elongated area of vorticity (Figure 3.22c).

Minimum and maximum ranges on model omega, term omega with sigma and term omega without sigma, vorticity advection, and thickness advection for August 21, 2011 are listed in Table 3.16. Figure 3.22 shows observations from the August 21, 2011 case study day: Panel a.) 300 hPa pressure level heights (geopotential meters) and shaded isotachs ranging from 30 ms^{-1} to 70 ms^{-1}. Panel b.) Surface mean sea level pressure (hPa) and shaded isentropes ranging from 255 k to 300 k. Panel c.) 500 hPa pressure level heights (geopotential meters) and shaded vorticity ranging from -2.0×10^{-4} s^{-1} to 4.0×10^{-4} s^{-1}. Panel d.) One hour rainfall accumulation mm hr^{-1} beginning at 18z. Panel e.) IR Satellite. Figure 3.23 compares the 300 hPa, 500 hPa, and 700 hPa levels for model omega (Panels a-c) and term omega without sigma (Panels d-f): Panel a.) 300 hPa pressure level. Panel b.) 500 hPa pressure level. Panel c.) 700 hPa pressure level shaded by model derived omega at 2.5×10^{-1} ms^{-1} to -2.5×10^{-1} ms^{-1}. Panel d.) 300 hPa pressure level. Panel e.) 500 hPa pressure level. Panel f.) 700 hPa pressure level shaded by term omega calculated without sigma at 2.5×10^{-5} to -2.5×10^{-5} for August 21, 2011.

Figure 3.24 displays the six panel contours for August 21, 2011: Panel a.) Contoured omega calculated with sigma at 2.0×10^{-3} ms^{-1}. Panel b.) Contoured vorticity advection at 2.5×10^{-9} rad s^{-2}. Panel c.) Contoured model derived omega at 1.0×10^{-2} ms^{-1}. Panel d.) Contoured omega calculated without sigma at 1.5×10^{-6}. Panel e.) Contoured thickness advection at 2.5×10^{-9} K s^{-1}. Panel f.) Contoured divergence at 3.0×10^{-2} s^{-1}. Each contour is colored by pressure (75-1000 hPa). Figure 3.21b shows contoured term omega calculated with sigma with boundary layer included at 3.0×10^{-3} ms^{-1} for August 21, 2011. Figure 3.17 shows term omega calculated with sigma (ms^{-1}): Panel a.) May 300 hPa pressure level 2.0×10^{-3} to -2.0×10^{-3}. Panel b.) May 700 hPa pressure level 2.0×10^{-3} to -2.0×10^{-3}. Panel c.) August 300 hPa pressure level 2.5×10^{-3} to -2.5×10^{-3}. Panel d.) August 500 hPa pressure level 2.5×10^{-3} to -2.5×10^{-3}. Panel e.) December 300 hPa pressure level 3.5×10^{-3} to -3.5×10^{-3}. Panel f.) December 500 hPa pressure level 3.5×10^{-3} to -3.5×10^{-3}.

Table 3.16

Minimum and maximum ranges for calculated variables for Aug. 21, 2011.

	Lower Bound	Upper Bound
Model Omega	-4.3×10^{-1} ms^{-1}	7.7×10^{-1} ms^{-1}
Term Omega without sigma	-4.5×10^{-6}	7.9×10^{-6}
Term Omega with sigma	-1.4×10^{-1} ms^{-1}	6.7×10^{-1} ms^{-1}
Vorticity Advection	-1.0×10^{-8} rad s^{-2}	9.7×10^{-9} rad s^{-2}
Thickness Advection	-8.4×10^{-9} K s^{-1}	8.1×10^{-9} K s^{-1}

A typical summertime pattern holds for August 21, 2011, while the influence of a trough skirts the Canadian border. Term omega particularly picks up on the upward vertical velocities associated with the trough (Figure 3.24d). Vorticity advection (Figure 3.24b) is the predominant dynamic forcing feature on the western side of the trough, over Minnesota and Wisconsin, and thickness advection (Figure 3.24e) is dominant over the eastern side of the trough. Showers and storms are strongly associated with an area of vertical velocities over western New York. Model omega also shows upward vertical velocities (1.0×10^{-2} ms^{-1}) over New England but does not show any velocities associated with the vorticity advection over Minnesota. Infrared satellite imagery (Figure 3.22e) does show cloud cover over Minnesota and Wisconsin in the same orientation as term omega while model omega shows no vertical motion.

The 300 hPa level term omega calculated with sigma (Figure 3.17b) shows a strong area of upward motion over the eastern Great Lakes with an abrupt change to downward velocities over eastern New York. A similar feature exists along the US Canadian border with strong upward motion to the north and strong vertical motion to the south. The pattern could possibly be a result of the conserved nature of static stability. The pattern disappears at 500 hPa (Figure 3.17e) with a smaller range of values, due to the lack of dynamic forcing in the summer months.

Over the Southeast, model omega (Figure 3.24c) shows scattered, thermodynamically driven convection while term omega calculated without sigma shows none (Figure 3.24d). This is expected as term omega is not dependent on thermodynamics. Despite model omega depicting scattered convection, it does not correctly locate the convection. Term

omega calculated with sigma (Figure 3.24a) does show larger groups of convection over the southeast, but this convection is also spread across the midwest which does not verify. Neither term nor model omega show strong vertical velocities with convection over the desert southwest. Interestingly, term omega calculated with sigma shows a gap in velocities precisely where the cloud cover is most widespread. The reason for this might be attributed to the mountainous terrain in the desert regions of the continental US.

The 300 hPa level term omega (Figure 3.23d) shows strong (2.5×10^{-5} to -2.5×10^{-5}), broad vertical velocities associated with the trough, especially over Lake Erie. The strongest model omega at 300 hPa (Figure 3.23a) is just north of Maine. This suggests that the convection over New York is more dynamically driven while the convection north of Maine is more thermodynamically driven, though both term and model omega show vertical motion for both areas. At lower levels, term omega (Figure 3.23e,f) is smoother, a result of the lack of thermodynamic forcing functions within term omega. Model omega (Figure 3.23b,c) continues to be focused on thermodynamic convection, while coverage is similar to radar imagery, the location of convection does not match as in the July case study.

A second broader area of vorticity advection (Figure 3.24b) is located over the Canadian maritime. Model omega (Figure 3.24c) is once again dominated by orographic effects north of Washington state while term omega (Figure 3.24d) paints more broadly occurring vertical motion. Cloud cover associated with the trough (Figure 3.22e) closely aligns with term omega.

Pearson's R correlations at 300 hPa, 500 hPa, 700 hPa, and the atmospheric column from 1000 hPa to 50 hPa for model omega to term omega with sigma and term omega without sigma for August 21, 2011 are shown in Table 3.17. Pearson's R correlations at 300 hPa, 500 hPa, 700 hPa, and the atmospheric column from 1000 hPa to 50 hPa for vorticity advection to thickness advection, vorticity advection to model omega, and thickness advection to model omega for August 21, 2011 are shown in Table 3.18. As the synoptic conditions are similar for the July and August case studies, the correlations are similar (Table 3.17). The 700 hPa has the strongest correlation, then 300 hPa and 500 hPa, and the column correlation is an order of magnitude weaker. For term omega calculated without sigma, the correlations along pressure levels are similar, and the correlation for the column an order of magnitude weaker 10^{-2}.

Table 3.17

Correlations for model omega to term omega for Aug. 21, 2011.

	With Sigma	Without Sigma
300 hPa	0.0033	0.1599
500 hPa	0.0060	0.1484
700 hPa	0.0302	0.1322
Column	0.0001	0.0909

3.1.7 October 5, 2011

A mostly benign pattern holds for the center of the country as a trough develops along the west coast and a second trough exits the east coast. A tight vorticity maximum

a.) 300 hPa   c.) 500 hPa

b.) Surface   d.) Radar

e.) IR Satellite
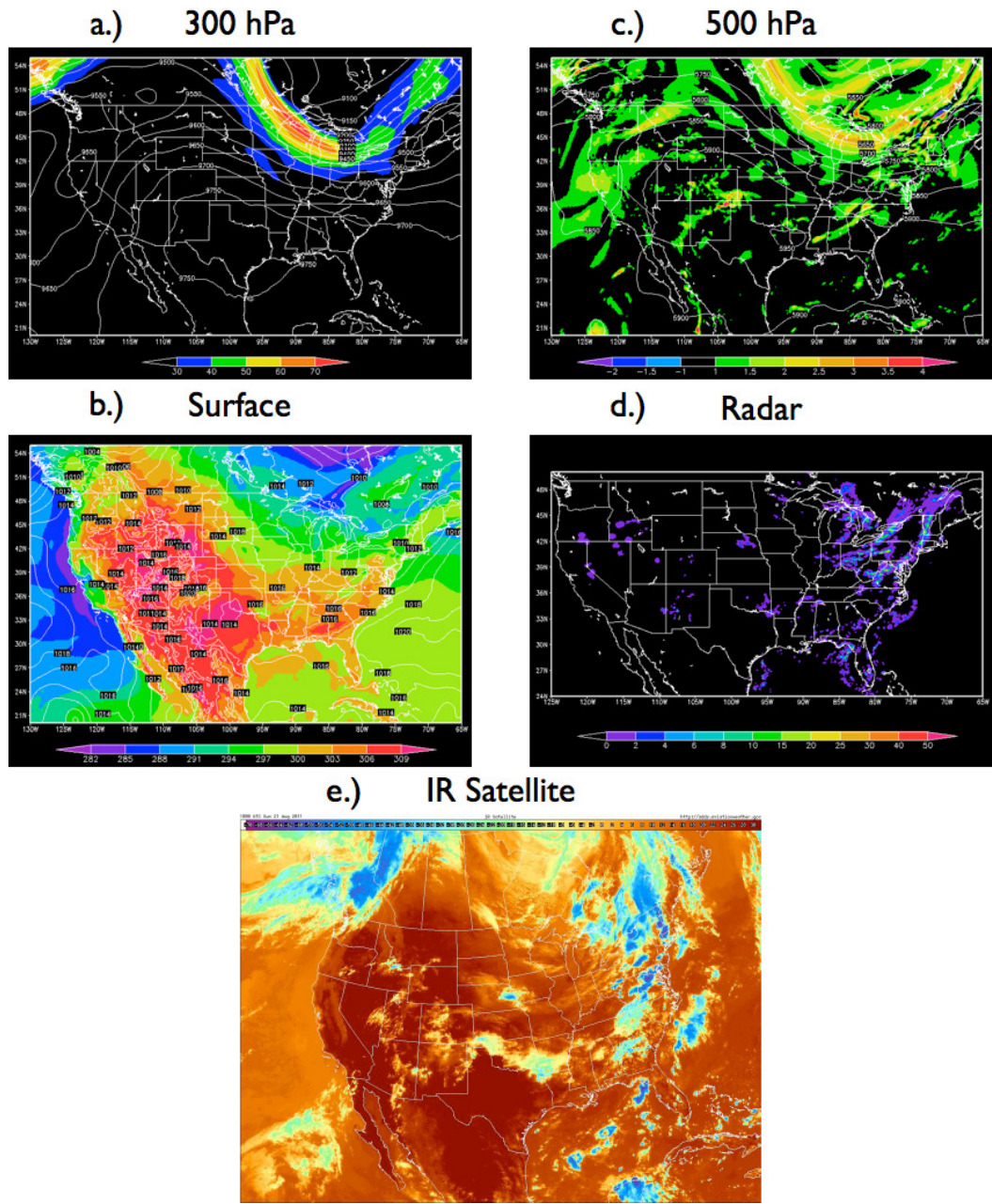
Figure 3.22

August 21, 2011 18z observations

93
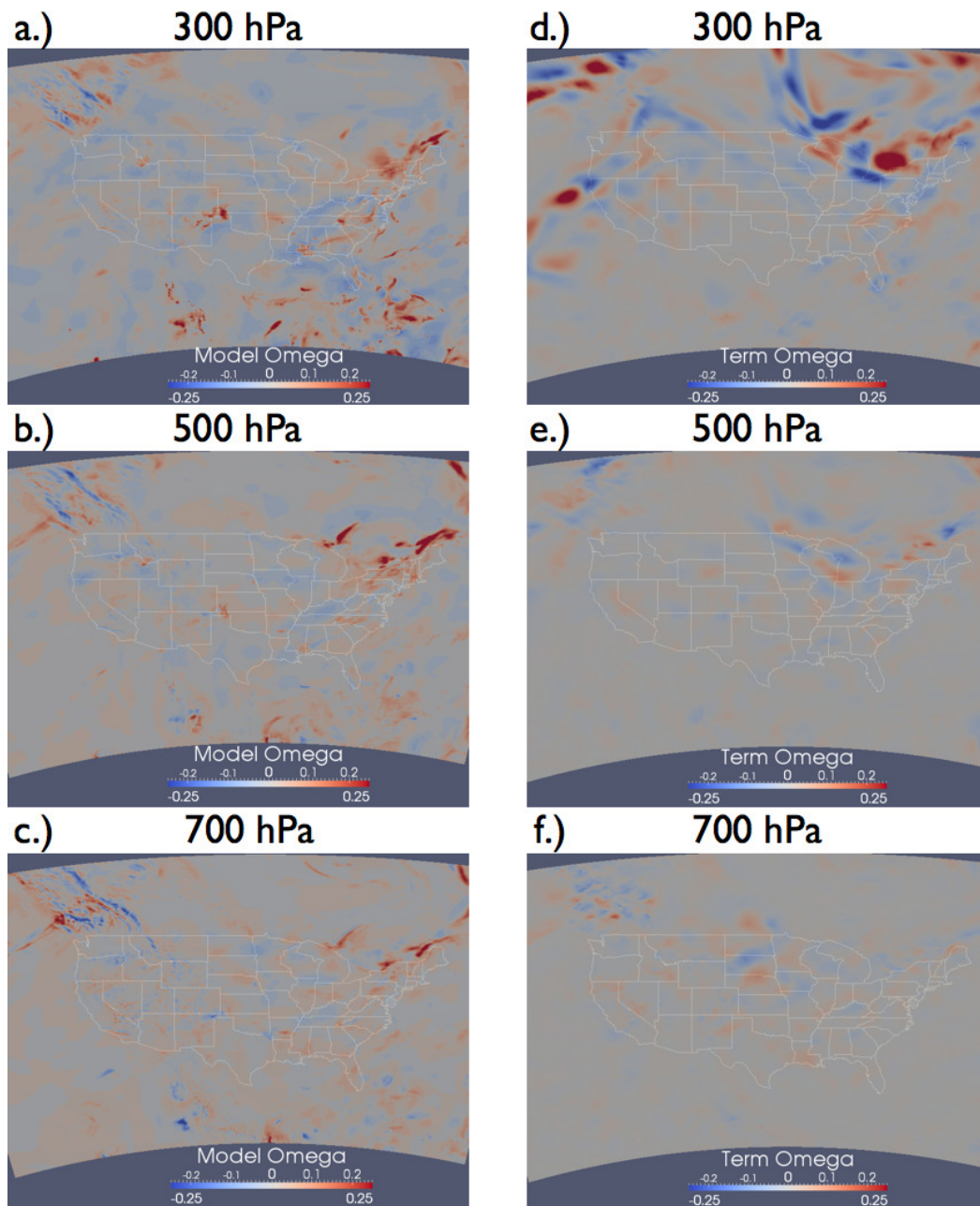
Figure 3.23

Isobars shaded by model omega or term omega without sigma on Aug. 21, 2011
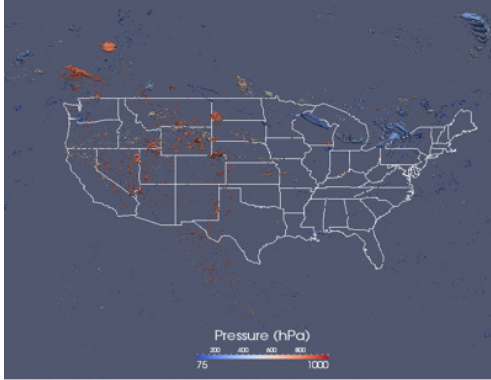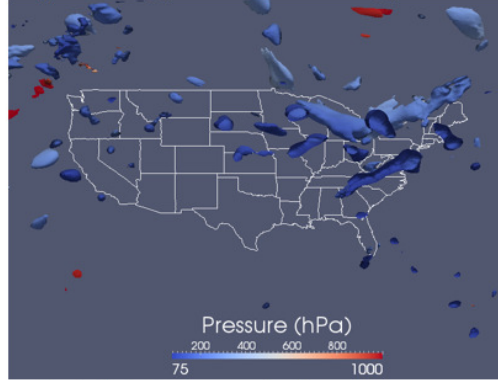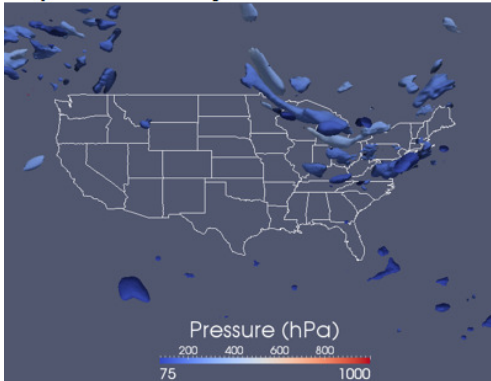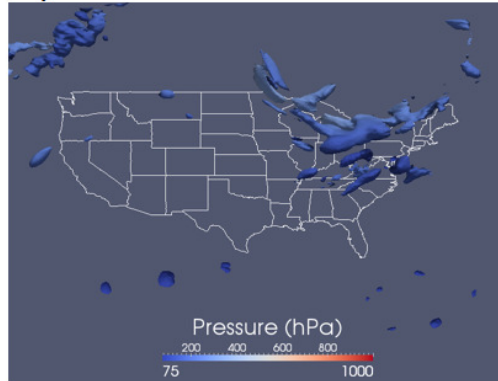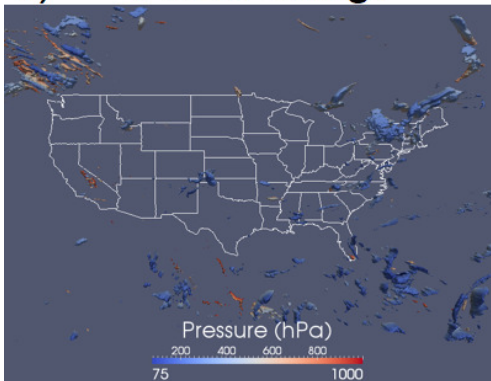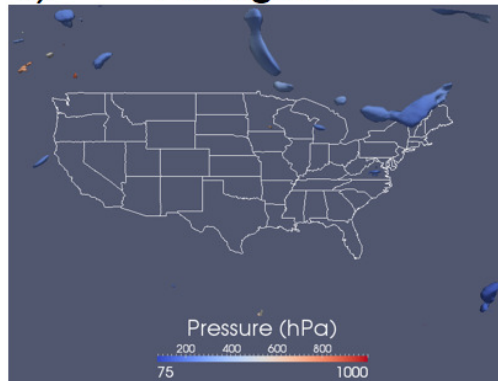
Figure 3.24

Six panel contours for August 21, 2011.

Table 3.18

Correlations between terms for Aug. 21, 2011.

	Vorticity Advection to Thickness Advection	Vorticity Advection to Model Omega	Thickness Advection to Model Omega
300 hPa	-0.6316	0.5623	0.2859
500 hPa	-0.6921	0.4662	0.3159
700 hPa	-0.6096	0.4943	0.3877
Column	-0.7287	0.5037	0.2246

(Figure 3.25c) that is responsible for precipitation and cloud cover over New England

(Figure 3.25d, e) lies just off the Delmarva Peninsula. The western trough has tightly

packed vorticity gradients (Figure 3.25c), which are creating a large area of cloud cover

extending from Canada, through the mountain west, and into Mexico.

Minimum and maximum ranges on model omega, term omega with sigma and term

omega without sigma, vorticity advection, and thickness advection for October 5, 2011

are listed in Table 3.19. Figure 3.25 shows observations from the October 5, 2011 case

study day: Panel a.) 300 hPa pressure level heights (geopotential meters) and shaded

isotachs ranging from 30 ms^{-1} to 70 ms^{-1}. Panel b.) Surface mean sea level pressure

(hPa) and shaded isentropes ranging from 245 k to 395 k. Panel c.) 500 hPa pressure

level heights (geopotential meters) and shaded vorticity ranging from -2.0×10^{-4} s^{-1} to

4.0×10^{-4} s^{-1}. Panel d.) One hour rainfall accumulation mm hr^{-1} beginning at 0z. Panel

e.) IR Satellite. Figure 3.26 compares the 300 hPa, 500 hPa, and 700 hPa levels for model

omega (Panels a-c) and term omega without sigma (Panels d-f): Panel a.) 300 hPa pressure

level. Panel b.) 500 hPa pressure level. Panel c.) 700 hPa pressure level shaded by model

derived omega at 2.5×10^{-1} ms^{-1} to -2.5×10^{-1} ms^{-1}. Panel d.) 300 hPa pressure level.

Panel e.) 500 hPa pressure level. Panel f.) 700 hPa pressure level shaded by term omega

calculated without sigma at 2.5×10^{-5} to -2.5×10^{-5} for October 5, 2011. Figure 3.27

displays the six panel contours for October 5, 2011: Panel a.) Contoured omega calculated

with sigma at 2.0×10^{-3} ms^{-1}. Panel b.) Contoured vorticity advection at 2.2×10^{-9} rad

s^{-2}. Panel c.) Contoured model derived omega at 1.1×10^{-1} ms^{-1}. Panel d.) Contoured

omega calculated without sigma at 1.3×10^{-6}. Panel e.) Contoured thickness advection

at 2.2×10^{-9} K s^{-1}. Panel f.) Contoured divergence at 2.5×10^{-2} s^{-1}. Each contour is

colored by pressure (75-1000 hPa).

Table 3.19

Minimum and maximum ranges for calculated variables for Oct. 5, 2011.

	Lower Bound	Upper Bound
Model Omega	-6.5×10^{-1} ms^{-1}	1.0×10^{1} ms^{-1}
Term Omega without sigma	-1.2×10^{-5}	1.1×10^{-5}
Term Omega with sigma	-6.5×10^{-2} ms^{-1}	1.3×10^{-1} ms^{-1}
Vorticity Advection	-1.2×10^{-8} rad s^{-2}	1.2×10^{-8} rad s^{-2}
Thickness Advection	-1.1×10^{-8} K s^{-1}	9.0×10^{-9} K s^{-1}

The most impressive feature is the Pacific trough. A large area of rain is being pushed

into the Pacific Northwest and northern California. Term omega (Figure 3.27d) shows an

extensive area of vertical motion along the Pacific coast which extends though the entire

troposphere. Additional smaller areas of UVVs cover areas of the southwest, especially

Arizona. This coincides well with scattered shower activity (Figure 3.25d) throughout the

interior Rockies that is caused by a strongly negatively tilted shortwave through western Arizona. There is a strong vorticity maximum (Figure 3.25c) associated with the shortwave, and there is a clear impact on the upward vertical motion shown by term omega. An area of dynamic forcing shown by vorticity advection but not shown by thickness advection is over New York and New Jersey. This area has limited dynamic forcing shown by term omega without sigma. A reason for this might be the high correlation between negative thickness advection and vorticity advection (Table 3.21). There is a high degree of cancelation between vorticity advection and thickness advection in the upper levels. Both vorticity advection (Figure 3.27b) and thickness advection (Figure 3.27e) show lower and middle level vertical motion. The broadest area of vertical motion shown by term omega with sigma (Figure 3.27a) is coincident with the vorticity maximum, with model omega (Figure 3.27c) also showing mid level UVVs over southern Arizona. This vorticity advection is heavily influencing vertical motion over Arizona. However, despite good agreement among term and model omega, precipitation and cloud cover are limited in extent (Figure 3.25d,e). This is most likely a result of a lack of moisture over the desert southwest.

Term omega calculated with sigma (Figure 3.27a) highlights the edge of cloud cover along the lee side of the Rocky Mountains. Term omega calculated with sigma also shows a strong area of upward vertical velocities over southwestern Arizona and several areas of UVVs over Minnesota that are not shown by model omega, term omega calculated without sigma, or vorticity and thickness advection. These smaller areas of vertical motion

correspond to non-precipitating low level clouds at the top of the upper level ridge over central Minnesota.

A second, weaker trough is exiting the Northeast. Comparing term omega (Figure 3.27d) to model omega (Figure 3.27c) shows that term omega holds vertical motion further upstream than model omega. Term omega has UVVs over eastern Maine, while model omega has vertical motion well off the coast. Infrared satellite imagery (Figure 3.25e) shows that term omega is closer to the location and coverage of clouds and precipitation. The placement of the convection near Maine by term omega and model omega is mirrored at the 300 hPa level (Figure 3.26a,d); term omega also shows stronger subsidence directly behind the trough at 300 hPa (Figure 3.26d). The pattern of subsidence off the New Jersey coast closely matches the clearing pattern behind the storm system as shown on IR satellite (Figure 3.25e).

Also of note at 300 hPa (Figure 3.26a,d) is the strong area of subsidence shown on term omega over southern Nevada that is only weakly mirrored by model omega. This area of subsidence aligns with a lack of cloud over in the same region. At 500 hPa (Figure 3.26e), term omega strongly shows the area of UVVs caused by mid-level vorticity advection, while model omega (Figure 3.26b) only shows scattered, orographically-caused vertical velocities. At 700 hPa, term omega (Figure 3.26f) shows only weak vertical velocities, and model omega (Figure 3.26c) shows isolated strong vertical motion throughout the mountain west, again caused by terrain.

Pearson's R correlations at 300 hPa, 500 hPa, 700 hPa, and the atmospheric column from 1000 hPa to 50 hPa for model omega to term omega with sigma and term omega

without sigma for October 5, 2011 are shown in Table 3.20. Pearson's R correlations at 300 hPa, 500 hPa, 700 hPa, and the atmospheric column from 1000 hPa to 50 hPa for vorticity advection to thickness advection, vorticity advection to model omega, and thickness advection to model omega for October 5, 2011 are shown in Table 3.21. The term omega calculated with sigma correlations are strongest in the middle and lower levels at 10^{-3} and weakest for 300 hPa and the column (Table 3.20). The correlations for term omega calculated without sigma are strongest at the middle and upper levels 10^{-1} and weakest for the lower levels and for the column.

Table 3.20

Correlations for model omega to term omega for Oct. 5, 2011..

	With Sigma	Without Sigma
300 hPa	0.0040	0.2765
500 hPa	0.0034	0.2557
700 hPa	0.0306	0.2202
Column	0.0007	0.1718

3.1.8 December 12, 2010

A strong nor-easter, driven by an upper-level trough digging across the eastern third of continental US, is developing along the Gulf Stream as an equally strong ridge is building in the western US. The eastern trough is being strengthened by a strong jet stream (Figure 3.28a) that is transporting mass through the trough at values of upwards of 50 ms^{-1} and a strong accompanying vorticity maximum across Mississippi and Alabama

a.) 300 hPa

c.) 500 hPa

b.) Surface

d.) Radar

e.) IR Satellite
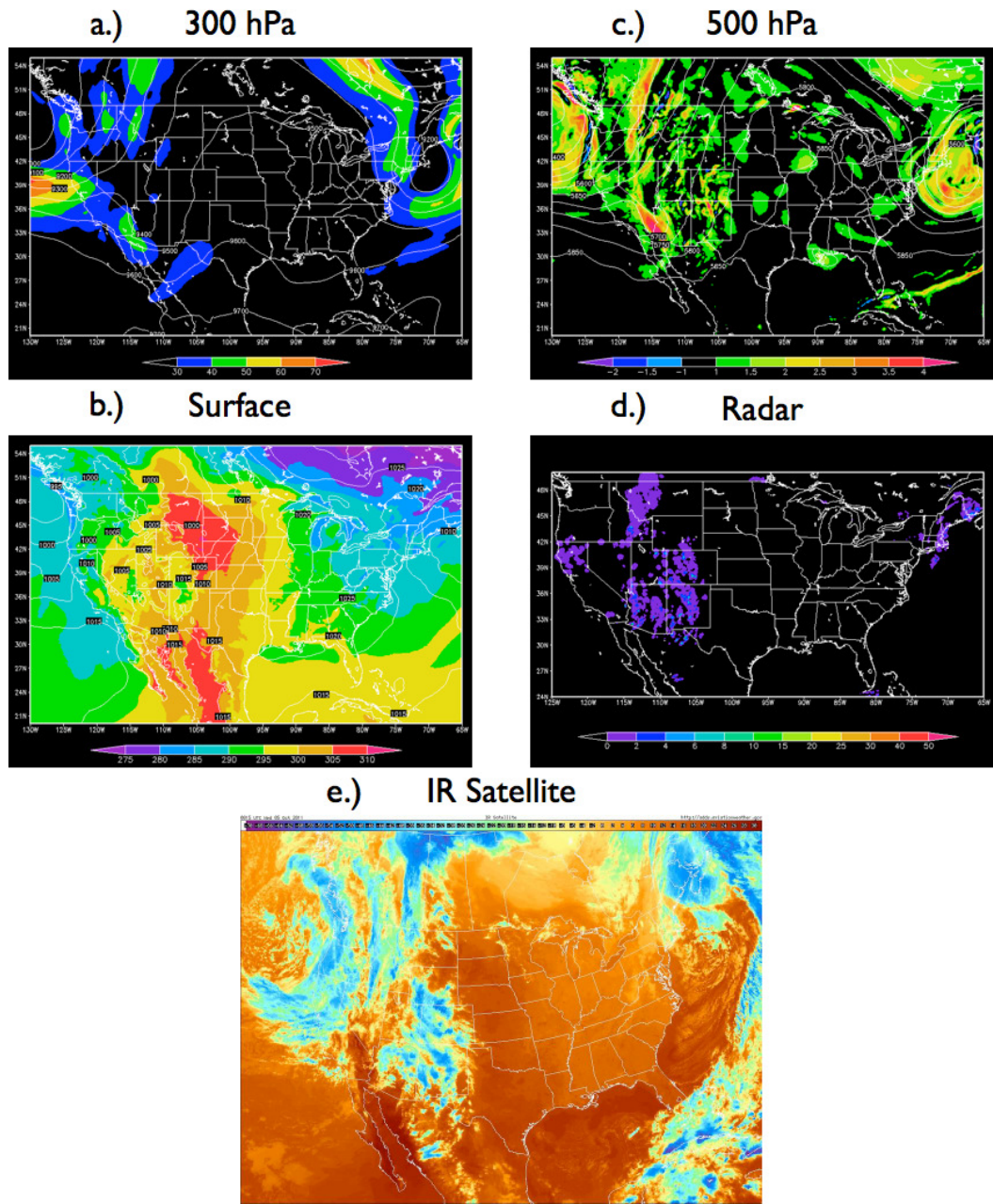
Figure 3.25

October 5, 2011 0z observations
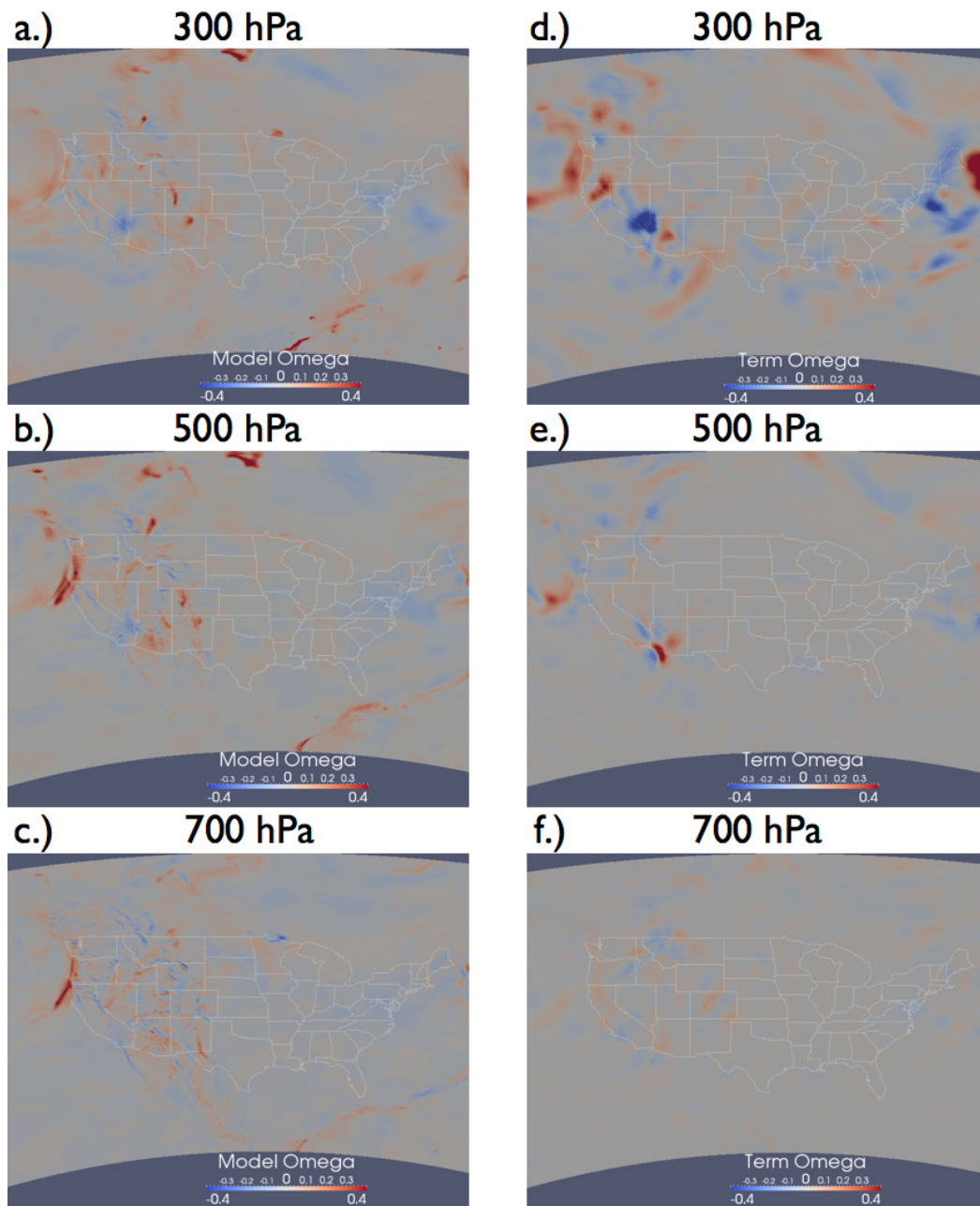
Figure 3.26

Isobars shaded by model omega or term omega without sigma on Oct. 5, 2011

a.) Omega with Sigma

d.) Omega without Sigma

b.) Vorticity Advection

e.) Thickness Advection

c.) Model Omega

f.) Divergence
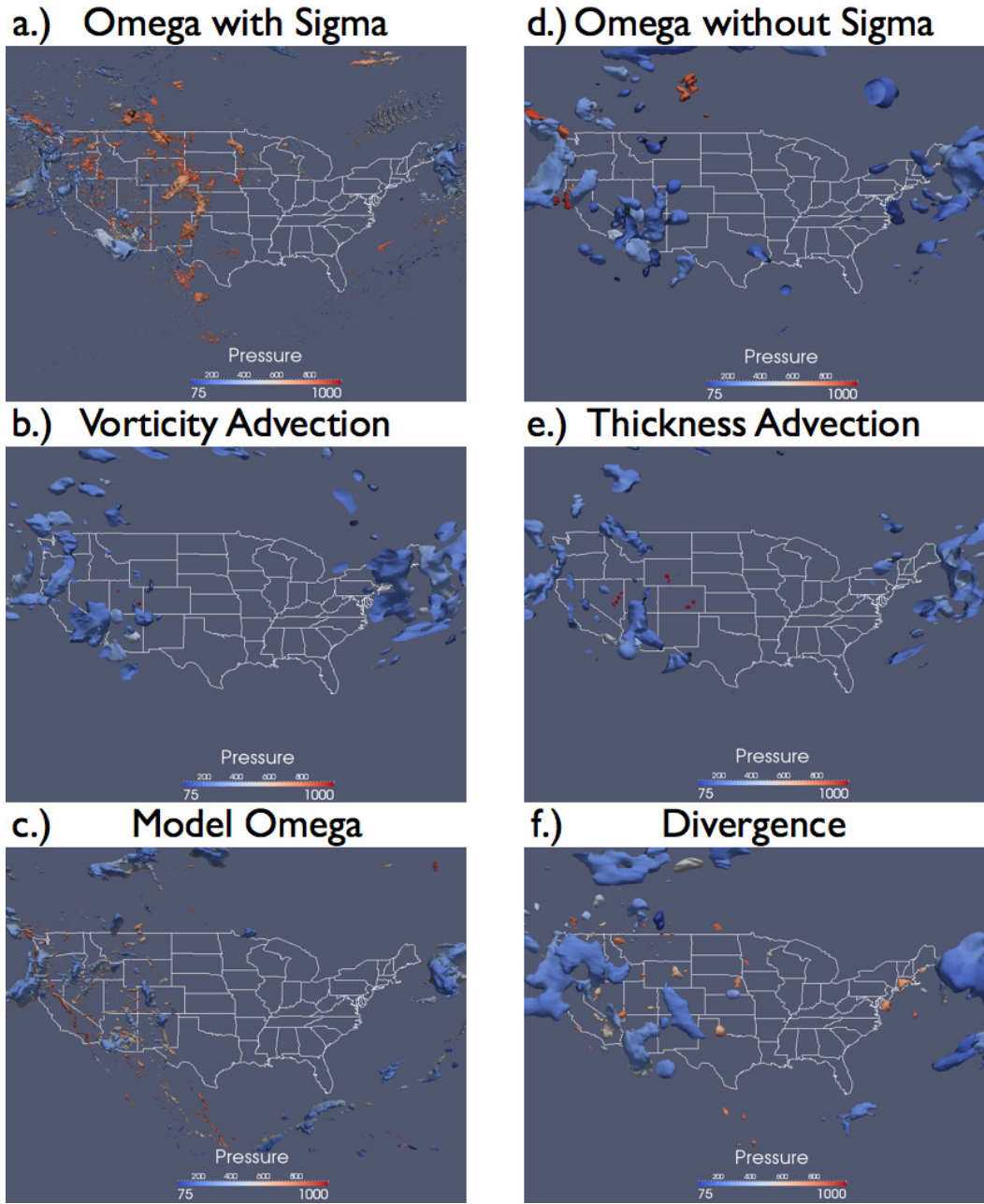
Figure 3.27

Six panel contours for October 5, 2011.

Table 3.21

Correlations between terms for Oct. 5, 2011.

	Vorticity Advection to Thickness Advection	Vorticity Advection to Model Omega	Thickness Advection to Model Omega
300 hPa	-0.6000	0.5428	0.3465
500 hPa	-0.6538	0.5417	0.2818
700 hPa	-0.5375	0.4613	0.5002
Column	-0.6778	0.5100	0.2874

(Figure 3.28c). These synoptic features are responsible for three large areas of precipitation (Figure 3.28d). A large shield of rain is exiting the east coast, stretching from Maine to South Carolina with a trailing cold front through southern Florida. A second area of precipitation is falling across the Ohio River valley as moisture wraps around the upper level low. Lastly, an approaching trough off the Pacific Northwest is triggering rain over Oregon and Washington state.

Minimum and maximum ranges on model omega, term omega with sigma and term omega without sigma, vorticity advection, and thickness advection for December 12, 2010 are listed in Table 3.22. Figure 3.28 shows observations from the December 12, 2010 case study day: Panel a.) 300 hPa pressure level heights (geopotential meters) and shaded isotachs ranging from 30 ms^{-1} to 70 ms^{-1}. Panel b.) Surface mean sea level pressure (hPa) and shaded isentropes ranging from 235 k to 290 k. Panel c.) 500 hPa pressure level heights (geopotential meters) and shaded vorticity ranging from -2.0×10^{-4} s^{-1} to 4.0×10^{-4} s^{-1}. Panel d.) One hour rainfall accumulation mm hr^{-1} beginning at 0z. Panel e.) IR Satellite. Figure 3.29 compares the 300 hPa, 500 hPa, and 700 hPa levels for model

omega (Panels a-c) and term omega without sigma (Panels d-f): Panel a.) 300 hPa pressure level. Panel b.) 500 hPa pressure level. Panel c.) 700 hPa pressure level shaded by model derived omega at 3.5×10^{-1} ms^{-1} to -3.5×10^{-1} ms^{-1}. Panel d.) 300 hPa pressure level. Panel e.) 500 hPa pressure level. Panel f.) 700 hPa pressure level shaded by term omega calculated without sigma at 3.5×10^{-5} to -3.5×10^{-5} for December 12, 2010. Figure 3.30 displays the six panel contours for December 12, 2010: Panel a.) Contoured omega calculated with sigma at 2.5×10^{-3} ms^{-1}. Panel b.) Contoured vorticity advection at 3.5×10^{-9} rad s^{-2}. Panel c.) Contoured model derived omega at 1.5×10^{-2} ms^{-1}. Panel d.) Contoured omega calculated without sigma at 1.8×10^{-6}. Panel e.) Contoured thickness advection at 3.5×10^{-9} K s^{-1}. Panel f.) Contoured divergence at 3.0×10^{-2} s^{-1}. Each contour is colored by pressure (75-1000 hPa). Figure 3.31 shows downward velocities and convergence for December 12, 2010. Panel a.) Contoured negative omega calculated without sigma at -1.9×10^{-6}. Panel b.) Contoured negative model derived omega at -1.0×10^{-2} ms^{-1}. Panel c.) Contoured convergence at -3.0×10^{-3} s^{-1} for May 12, 2011. Each contour is colored by pressure (75-1000 hPa). Figure 3.17 shows term omega calculated with sigma (ms^{-1}): Panel a.) May 300 hPa pressure level 2.0×10^{-3} to -2.0×10^{-3}. Panel b.) May 700 hPa pressure level 2.0×10^{-3} to -2.0×10^{-3}. Panel c.) August 300 hPa pressure level 2.5×10^{-3} to -2.5×10^{-3}. Panel d.) August 500 hPa pressure level 2.5×10^{-3} to -2.5×10^{-3}. Panel e.) December 300 hPa pressure level 3.5×10^{-3} to -3.5×10^{-3}. Panel f.) December 500 hPa pressure level 3.5×10^{-3} to -3.5×10^{-3}.

Table 3.22

Minimum and maximum ranges for calculated variables for Dec. 12, 2010.

	Lower Bound	Upper Bound
Model Omega	-8.1×10^{-1} ms^{-1}	1.0×10^{1} ms^{-1}
Term Omega without sigma	-7.6×10^{-6}	7.0×10^{-6}
Term Omega with sigma	-7.6×10^{-2} ms^{-1}	6.6×10^{-1} ms^{-1}
Vorticity Advection	-1.8×10^{-8} rad s^{-2}	2.0×10^{-8} rad s^{-2}
Thickness Advection	-2.3×10^{-8} K s^{-1}	2.0×10^{-8} K s^{-1}

An upper-level trough is digging across the eastern third of the continental US. As this system is strongly dynamically driven, term omega performs well. Term omega without sigma (Figure 3.30d) shows vertical motion at the upper levels over New York, eastern Pennsylvania, eastern Virginia, the Carolinas through Florida and curving back to Louisiana. Term omega shows low level vertical motion over eastern New England and the northern Great Lakes. These areas coincide with the greatest cloud cover and heaviest precipitation (Figure 3.28d,e). Term omega calculated with sigma (Figure 3.30a) brings out lower level (600 hPa) vertical motion over the Carolinas and Virginia while reducing the vertical motion at the upper levels over the Gulf Stream. Model omega (Figure 3.30c) shows vertical velocities favored to the Northeast while showing few vertical velocities with the cold front itself; what limited vertical velocities that are associated with the front are placed too far east.

Comparing vorticity advection (Figure 3.30b) and thickness advection (Figure 3.30e) shows that the largest areas of thickness advection are further north while the strongest vorticity is further south. When viewing term omega calculated with sigma (Figure 3.30a),

106

the strongest low level vertical velocity values are to the north where the greatest thickness advection occurs. This seems to concur with QG theory as thickness advection is strongest below 500 hPa while vorticity advection is strongest above 500 hPa.

Looking at the divergence pattern (Figure 3.30f) shows strong upper level divergence over the Northeast and a second area of strong divergence off the coast of the Carolinas ahead of the front that confirms the location of vertical velocities. Lower level convergence (Figure 3.31c) is greatest over the Northeast, forcing upward vertical velocities. Upper level convergence is greatest across Louisiana and Texas, which should encourage downward vertical velocities (Figure 3.31a).

A plot of 500 hPa term omega with sigma (Figure 3.17f) shows a wedge shaped feature just north of New York. An abrupt wedge of DVVs is surrounded by a strong area of UVVs. The reason for such a shape is unknown, although the particular shape might possibly have to do with nearby Lake Ontario. Further south, term omega with sigma mirrors the strong forcing over central Florida, suggesting this forcing is more synoptically driven. At 300 hPa, term omega with sigma (Figure 3.17c) shows further UVVs over New York and off the coast of the Carolinas but no forcing over southeast, implying that the forcing over Florida at 500 hPa is only due to the surface front.

Of interest is a large area of upward vertical velocities from term omega over the Gulf of Mexico and extending into Louisiana. These vertical velocities show up with (Figure 3.30d) or without sigma (Figure 3.30a); however, precipitation or cloud cover are not present in those areas (Figure 3.28d,e). While it is possible that the environment is simply too dry to support cloud formation, a second explanation is possible. The vertical veloc-

107

ities over the Gulf of Mexico are a result of vorticity advection (Figure 3.30b); a large maximum of vorticity extends from New York to Florida to Louisiana (Figure 3.28c). At the downstream side of the vorticity maximum, vorticity contours align with isoheights, thus while the vorticity is strong, vorticity advection is weak (i.e. an area of strong vorticity advected into a similarly strong area of vorticity yields little vorticity advection). So, vertical motion is actually weak. However, as term omega uses a finite differencing technique that is dependent on trough wavelength but not dependent on trough orientation, the grid space smoothing is detrimental. A wider cartesian grid spacing compares values that cut across isoheights in a strictly east-west, north-south direction, while the flow follows a more northwest to southeast pattern, so term omega picks up on vorticity advection where there is actually none.

To the west, pieces of energy are riding over the top of a strong ridge (Figure 3.28a). Both term omega (Figure 3.30d) and model omega (Figure 3.30c) show this and are in agreement on the general height, location and coverage of vertical velocities; however, once again orography plays a key role in the shape of vertical velocities in model omega. Term omega provides dynamical smoothing and is of better coverage in the location of precipitation.

The six panel pressure plots show that term omega places the strongest vertical motion at the upper levels (Figure 3.29d-f). The strongest vertical motion occurs at 300 hPa (Figure 3.29d) and is associated with the aforementioned vorticity advection over the Gulf of Mexico. At 500 hPa (Figure 3.29e), the strongest forcing is over Florida, which is caused by the cold front. Vertical motion at 700 hPa (Figure 3.29f) is uniform and fairly weak.

108

Model omega (Figure 3.29a-c) shows evenly distributed vertical motion between 300 hPa, 500 hPa, and 700 hPa. As is the case with previous study days, vertical motion is clearly influenced by the northern Rocky Mountains with model omega and is the cause of the resultant noisiness of the vertical motion data.

Pearson's R correlations at 300 hPa, 500 hPa, 700 hPa, and the atmospheric column from 1000 hPa to 50 hPa for model omega to term omega with sigma and term omega without sigma for December 12, 2010 are shown in Table 3.23. Pearson's R correlations at 300 hPa, 500 hPa, 700 hPa, and the atmospheric column from 1000 hPa to 50 hPa for vorticity advection to thickness advection, vorticity advection to model omega, and thickness advection to model omega for December 12, 2010 are shown in Table 3.24. Correlations between term omega with sigma and model omega remain weak (Table 3.23) but is strongest for the 700 hPa level on the order of 10^{-2} The correlations for the middle and upper levels is an order of magnitude weaker while the column correlation is weakest at 10^{-4}. Term omega without sigma is of equal magnitude for each level and for the column at 10^{-1}

Table 3.23

Correlations for model omega to term omega for Dec. 12, 2010.

	With Sigma	Without Sigma
300 hPa	0.0084	0.1437
500 hPa	0.0021	0.2226
700 hPa	0.0219	0.1885
Column	0.0009	0.1155

a.) 300 hPa

c.) 500 hPa

b.) Surface

d.) Radar

e.) IR Satellite
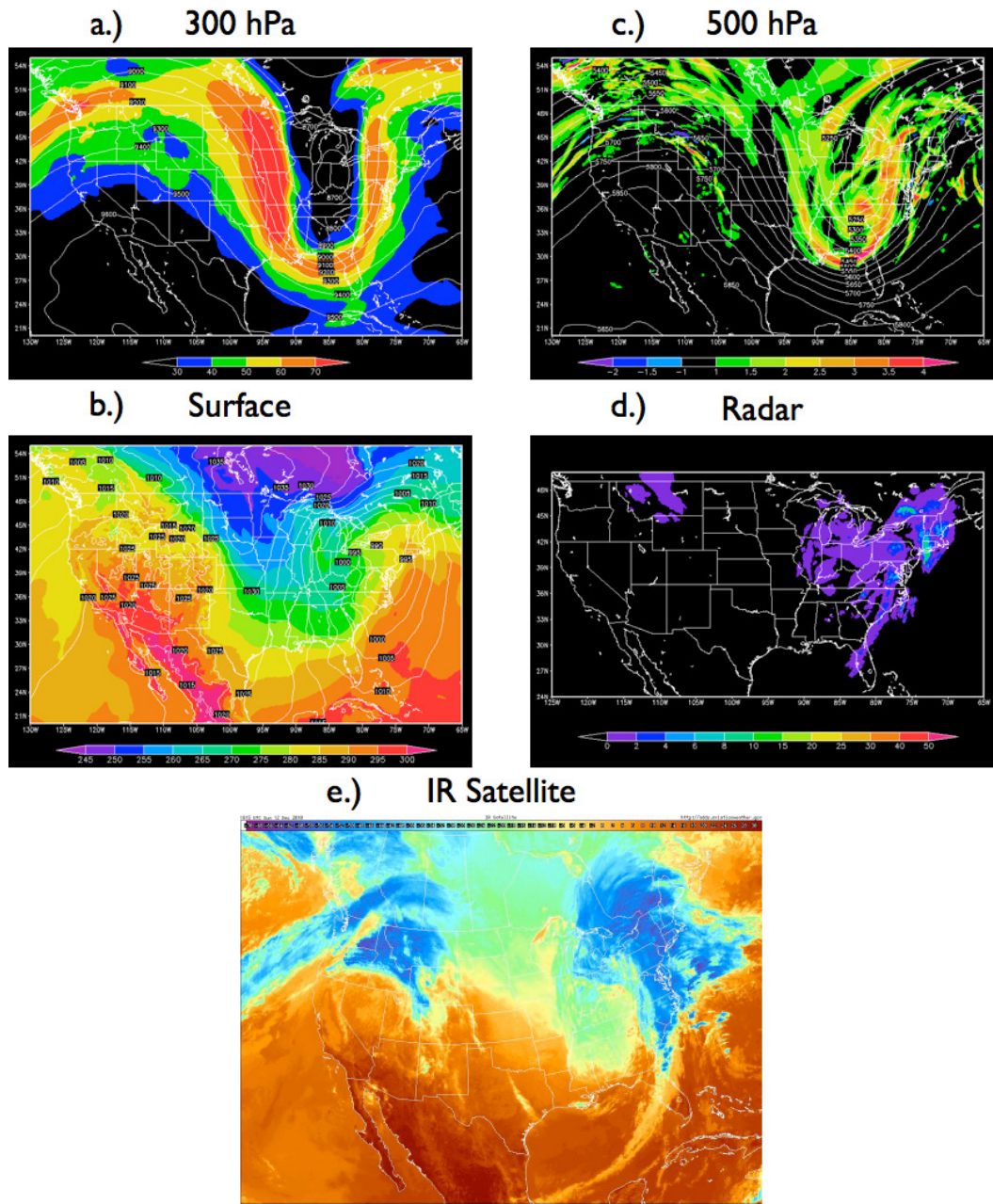
Figure 3.28

December 12, 2011 0z observations

110
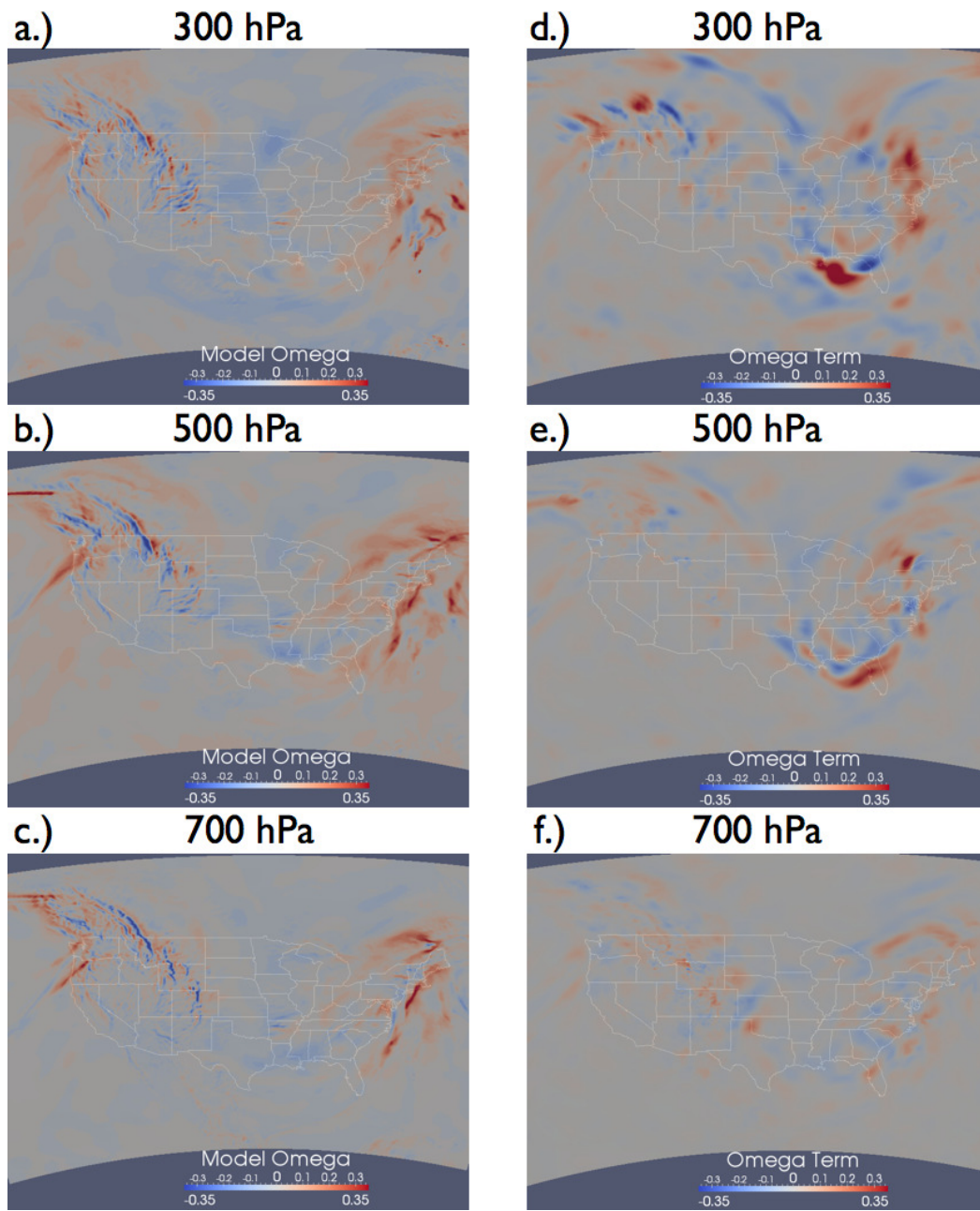
Figure 3.29

Isobars shaded by model omega or term omega without sigma on Dec. 12, 2010

a.) Omega with Sigma   d.) Omega without Sigma

Pressure (hPa)

b.) Vorticity Advection   e.) Thickness Advection

Pressure (hPa)

c.) Model Omega   f.) Divergence

Pressure (hPa)
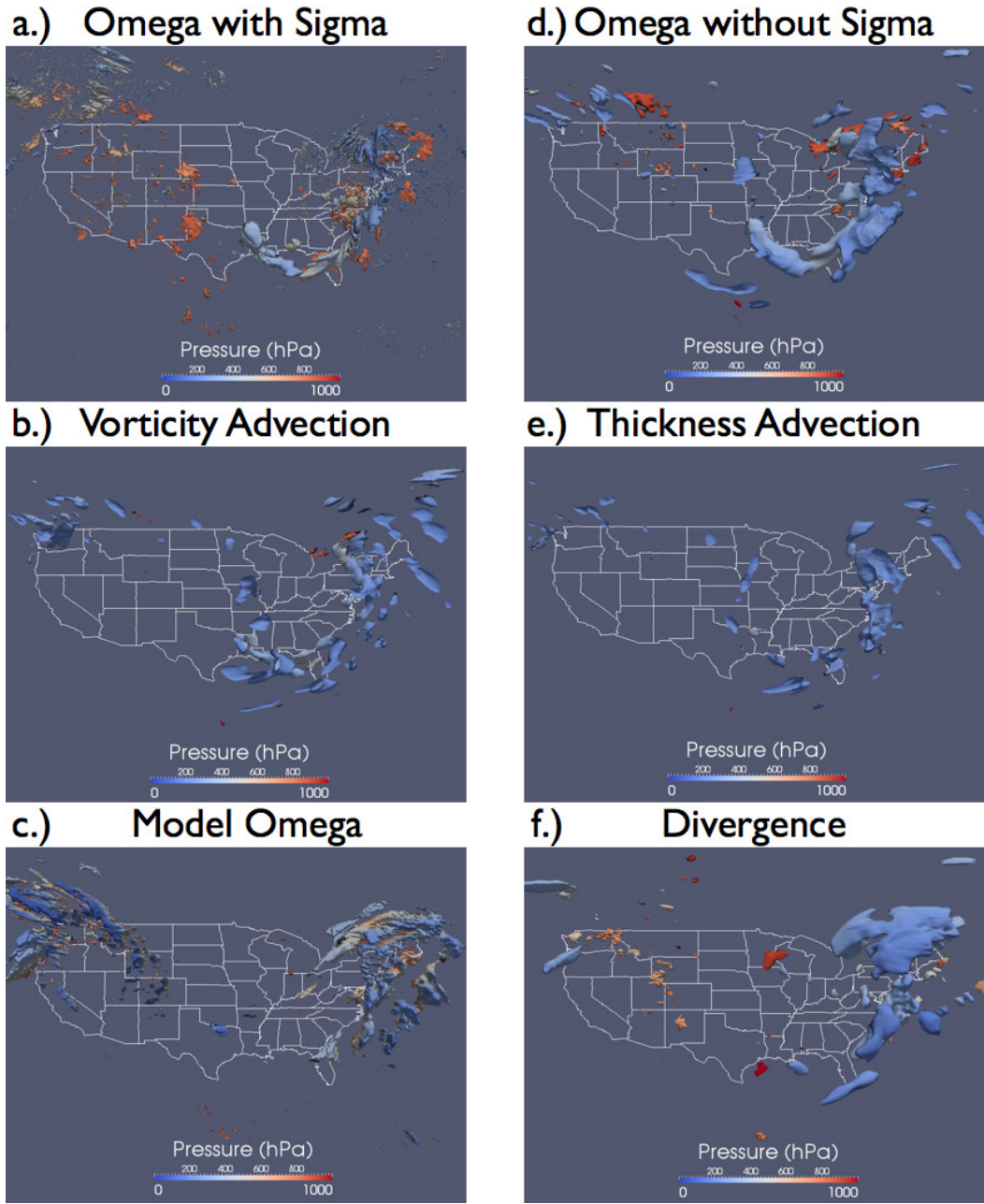
Figure 3.30

Six panel contours for December 12, 2011.

a.) Negative Omega without Sigma
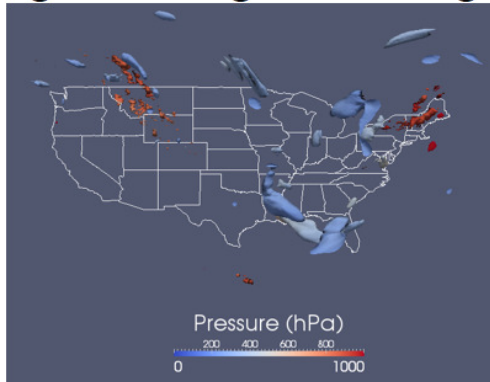
b.) Negative Model Omega
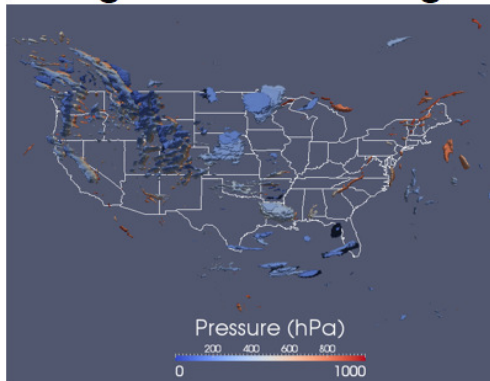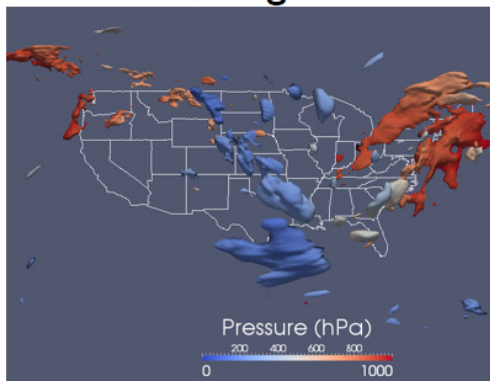
c.) Convergence

Figure 3.31

Three panel downward velocities and convergence for December 12, 2010.

Table 3.24

Correlations between terms for Dec. 12, 2010.

	Vorticity Advection to Thickness Advection	Vorticity Advection to Model Omega	Thickness Advection to Model Omega
300 hPa	-0.7708	0.5505	0.1075
500 hPa	-0.6753	0.5255	0.2727
700 hPa	-0.7047	0.3526	0.4154
Column	-0.8422	0.3002	0.2614

3.2 Correlation Statistics

Pearson's R correlations between term omega and model omega uniformly show that term omega calculated without sigma (Table 3.26) is approximately an order of magnitude more strongly correlated to model omega than term omega calculated with sigma (Table 3.25). Term omega with sigma has correlations ranging from 10^{-2} to 10^{-6}. Term omega without sigma has uniform correlations ranging from 10^{-1} to 10^{-2}.

Term omega calculated with sigma shows great variability between seasons. For the atmospheric column, the smallest correlations were shown to be during the warmer months with the smallest correlation at any time for any variable to be during May for the entire atmospheric column. The cooler months are more strongly correlated to model omega with correlations an order of magnitude greater than during the summer for the entire column. A similar pattern followed for the 300 hPa level with the exception of July which showed a similar correlation to the cooler months. Correlations for the 500 hPa level were more uniform across the seasons. For 700 hPa, there is little pattern, but 700 hPa has stronger

correlations than the 300 hPa level; however, May is weakly correlated negatively. Of the eight case study days, the month of May has the lowest overall correlations.

The lower correlations for the entire column for term omega calculated with sigma result from the inclusion of the boundary layer. As sigma is influenced by the change in logarithmic potential temperature with height, sigma is small in the boundary layer as potential temperature is constant with height. The larger values for 500 hPa and 700 hPa can be explained by sigma as well. Sigma is larger higher in the troposphere and so minimizes upper level vertical motion. It is in the mid and lower levels where sigma is smaller that correlations follow dynamical forced patterns.

Term omega calculated without sigma is more uniform across seasons and levels. Correlations for the entire column are the weakest, with the correlations for the summer months, July and August, being the weakest. This can be explained due the lack of dynamical forcing features during the summer months. Most convection during the summer is a result of thermodynamically driven, air mass thunderstorms. Term omega calculated without sigma has no way of finding thermodynamic properties or thermodynamic forcing and so performs poorly during the summer months.

For each of the levels, the highest correlations are by far on the 500 hPa level with the summer months again having the lowest correlations. The 300 hPa and 700 hPa levels are roughly the same order of magnitude correlation with the general pattern of cooler season cases having stronger correlations than warmer case study days with a few notable exceptions. The April case has low correlation at 300 hPa, and the January case has low correlation at 700 hPa.

Table 3.25

Correlation between model omega and term omega calculated with sigma.

	300 hPa	500 hPa	700 hPa	Column
January	0.0004	0.0072	0.0018	0.0002
March	0.0207	0.0022	0.0052	0.0013
April	0.0002	0.0069	0.0005	0.0006
May	0.0002	0.0150	-0.0032	0.000002
July	0.0034	0.0008	0.0094	0.00007
August	0.0033	0.0061	0.0302	0.0001
October	0.0040	0.0034	0.0306	0.0007
December	0.0084	0.0022	0.0219	0.0009

Table 3.26

Correlation between model omega and term omega calculated without sigma.

	300 hPa	500 hPa	700 hPa	Column
January	0.1690	0.2795	0.0800	0.0915
March	0.2741	0.2538	0.3384	0.1505
April	0.0668	0.2596	0.1510	0.1010
May	0.2461	0.3286	0.2215	0.1477
July	0.1554	0.1898	0.1605	0.0858
August	0.1599	0.1484	0.1323	0.0910
October	0.2764	0.2557	0.2202	0.1718
December	0.1437	0.2227	0.1886	0.1156

CHAPTER 4

DISCUSSION

4.1   The placement of forcing

In general, model omega and term omega agree in the placement of vertical forcing;
however, term omega has demonstrated considerable prowess in correctly placing vertical
forcing at times when model omega had difficulty in placing vertical motion. For exam-
ple, in the January case study day, model omega shows few upward vertical velocities
near the upper level low in Michigan (Figure 3.3c) or with the associated told front, while
term omega depicts scattered motion around the upper lever low and concentrated forcing
over the Great Lakes (Figure 3.3d). The satellite image for that day (Figure 3.1e) shows
widespread low level cloud cover across Michigan and westward to Minnesota. A second
example is the March 7 case where term omega places vertical forcing along the cold front
through southern Florida (Figure 3.7d), although model omega pushes the forcing much
further off the coast (Figure 3.7c). Again, the satellite image (Figure 3.5e) corroborates
term omega as a line of clouds extends across central Florida. In the April 4, 2011 case
study model, omega places the forcing further east of the front (Figure 3.10c), while term
omega correctly places the forcing (Figure 3.10d) along an axis of vorticity advection (Fig-
ure 3.8c). This positioning is accompanied by higher rainfall rates (Figure 3.8d) and colder
cloud tops (Figure 3.8e). In May, a large squall line over southeastern Texas is placed in

the Gulf of Mexico, several hundred miles too far east by model omega (Figure 3.14a-c), but term omega shows forcing over central Texas which is the correct location of the highest rainfall rates (Figure 3.12d). Lastly, in the October case study term omega places the exiting Northeast trough too far downstream from the coast of Maine (Figure 3.27c), while term omega (Figure 3.27d) places the forcing from the system correctly along the cast of Maine (Figure 3.25e).

When model omega is incorrect in the placement of vertical forcing, it is due to the placement of forcing too far downstream of the dynamic forcing mechanism. Though difficult to attribute a single reason for the poor placement of forcing by model omega in those cases, some possible explanations include the addition of thermodynamic forcing in model omega and the influence of orographic effects. As model omega relies on thermodynamic instability to place vertical motion, and thermodynamically favorable environments can exist far ahead of dynamic forcing, model omega can express large forcing well ahead of the primary dynamic forcing mechanism. Mountain terrain can heavily influence the structure and placement of vertical motion, driving vertical motion where dynamically there should be none, as can be seen over the mountain west in any case study day.

Though term omega does correctly place most vertical forcing, there are areas of forcing that are not at all associated with clouds or precipitation. For example, in the January 2, 2012 case study term omega places areas of vertical motion behind the trough (Figure 3.3d); however, there are no large areas of clouds or precipitation associated with those areas of forcing. Another example is during the October 5, 2011 case study where a strong vorticity maximum is in place over southern Arizona (Figure 3.25c), and forcing

due to vorticity advection is shown by both term omega (Figure 3.27d) and model omega (Figure 3.27c). However, there is no precipitation or even cloud cover shown in that region. In fact, there is a marked lack of cloud cover directly above the area of strongest forcing. An explanation for a lack of cloud cover in areas of forcing behind the trough could be a lack of moisture to develop clouds, but there is currently no reliable way to verify this assertion. A possible but expensive verification method could be using a series of regularly placed microwave sounders. A faster though more limited method of verification might be to examine the nearest sounding data for the given time period to assess the presence of moisture in the layers of vertical forcing.

4.2   Term Omega calculated with Sigma

Notwithstanding that term omega calculated with sigma is poorly correlated to model omega (Table 3.25), term omega with sigma does provide some additional information. Term omega with sigma shows low level forcing over the Mississippi delta, central Tennessee, and southern Ohio (Figure 3.10a) that is associated with colder cloud tops (Figure 3.8e) and thus stronger convection. Unfortunately, there is no way to discriminate between boundary layer noise and these larger pockets of low level forcing.

A second way term omega with sigma provides improvement is showing where the boundary layer is capped. On the May 12, 2011 study day, term omega with sigma shows upward vertical forcing in the low levels over eastern Nebraska and Kansas (Figure 3.17d); however, no cloud cover is present despite an abundance of moisture in the warm sector of the mid-latitude cyclone. Advancing six hours ahead shows widespread thunderstorm

activity over the area (Figure 3.13). It is possible that the reason for the strong low-level forcing without any apparent cloud cover at the 18z hour is the indication of a strong cap over the region that is quashing and delaying any potential development. It is only after the cap is broken that convection as a result of the low level thermodynamic forcing can reach the lifted condensation level to form clouds and storms.

Term omega with sigma does poorly in handling desert convection. In the August study day there is convection across the desert Southwest, and term omega with sigma shows forcing around the convection but not associated with the convection. The reason for this might be attributed to the geography in the desert regions of the continental US. Most desert terrain is elevated or otherwise near mountains. This mountainous terrain induces enhanced convergence and storms caused by outflow boundaries. Additional issues might stem from the poor parameterizations of the boundary layer in the desert Southwest and poor resolution of moisture transport from the Gulf of California.

Term omega with sigma is so biased towards instability in the low levels that visualizations of the boundary layer in the southeastern US are blanketed by low level thermodynamic forcing (Figure 3.21). This is not unexpected as the lowest levels of the atmosphere are unstable throughout the southeast on any given summer day, and the location of air mass thunderstorms is dependent on mesoscale boundaries such as outflow boundaries, diabatic thermal boundaries, and land-type boundaries that cannot be resolved by the NAM and certainly not by a dynamic methodology as is described in this project. As a result, the boundary layer is removed for all other visualizations besides Figure 3.21.

When viewed two-dimensionally, term omega with sigma demonstrates tight gradients in areas of strong vertical motion (Figure 3.17a,b,f). For example, for the May case study at 300 hPa (Figure 3.17a), a line of strong downward forcing is flanked on either side by strong upward motion. This tight gradient is collocated with convection along a warm front, but the exact cause of such a pattern is unknown. It is possible within small regions that because potential temperature is a conserved quantity, static stability is forced to be conserved as well, thus regions of strong positive vertical forcing must be balanced by nearby negative regions of forcing. Other similar patterns occur for 300 hPa in the August case study (Figure 3.17b) and 500 hPa in December (Figure 3.17f). The December study shows an arrow shaped structure over New York that aligns with the moisture gradient over the area and could also arise from the proximity of Lake Ontario. In the south, the gradients are not aligned side-by-side and are more widely distributed, similar to term omega calculated without sigma. This circumstance could be a result of the scale of forcing. When larger scale forcing occurs the requirement of conservation of potential temperature is across a larger area, and so forcing gradients are not tight. At the mesoscale, opposite signs of forcing must be adjacent to conserve static stability.

The disposition of term omega calculated with sigma to emphasize forcing in the boundary layer required the removal of the boundary layer when looking at sigma. However, by doing this, air mass convective thunderstorms, which are a primary weather feature for the southern US in summer, are completely removed from the domain. A simple solution to balance the proclivity for term omega with sigma to accentuate boundary layer convection with the necessity to represent boundary layer convection is not evident. At

121

this juncture it must be stated that term omega with or without sigma cannot well represent a summer case and should only be taken as a reference for any dynamically forced features.

4.3   Effects from Quasi-Geostrophic Theory

As calculated omega forcing relies completely on the tenets of QG theory, many effects from the theory manifest themselves within the visualization of omega forcing. The interplay between forcing from vorticity advection (Term B from Equation 1.6) and thickness advection (Term C from Equation 1.6) is quite evident. The January case study is a prime example of the interaction, cancelation, and reenforcement of vorticity and thickness advection forcing. For areas upstream of the primary forcing feature, a trough over the Great Lakes, negative vorticity advection and positive thickness advection overlap (Figure 3.4a, b) and are highly correlated (Table 3.3). In these areas the atmosphere is working to compensate between dynamic forcings of opposite sign. Negative thickness advection, that is lowered thickness as a result of cold air advection, compensates for limited values of positive vorticity advection that result from speed sheer from the jet stream. However, ahead of the trough, dynamic forcings align and reenforce each other. Here, the atmosphere must express those dynamic forcing features as vertical motion. The October case study also presented similar values for negative correlation between terms B and C of the omega equation (Table 3.21).

However, the May case study shows an example of relatively weak forcing from individual terms leading to strong overall forcing if the separate terms are additive. A QLCS is

departing the Texas coast, and vorticity advection (Figure 3.15b) and thickness advection (Figure 3.15e) are both weak; however, combined omega forcing (Figure 3.15d) is strong enough to support the movement of the squall line towards the Gulf of Mexico. This shows that while calculated omega forcing can properly combine the unique forcings, individual analysis of the vorticity advection forcing term and the thickness advection forcing term warrants the placement of total forcing.

The speed of horizontal winds plays a large role in determining the strength of dynamic vertical forcing. With strong horizontal winds, even small changes in the vorticity or thickness fields lead to strong dynamic forcing as the jet stream advects these small changes over brief time periods. So a small change in an atmospheric field that is accompanied by strong winds can yield advection and thus dynamic forcing that is as strong as what would be caused by a tight gradient advected through weak horizontal winds. This phenomenon might be at play in areas of large vorticity advection behind troughs as in the January study day (Figure 3.3b) and the December day (Figure 3.30c) where weak vorticity translates into strong vorticity advection.

Conversely, even strong vorticity can in some circumstances yield weak vorticity advection. Consider a scenario where an area of strong vorticity aligns with the jet stream. Only at the exit region of the area of strong vorticity does strong positive vorticity advection occur. Within the area of vorticity, even though vorticity is being advected, the vorticity is moving into a region of equally strong vorticity, so vorticity advection is small or even zero. This effect is clear in the December day where an area of strong vorticity aligns with the base of the trough over the southeast (Figure 3.28c). Here vorticity is

123

strong, but vorticity advection (Figure 3.30b) is weak. Nevertheless, in that same area total omega forcing is also strong. A second circumstance contributes to this phenomenon such that errors could result from the orientation of the coordinate system.

The axes of the cartesian coordinate system are by definition arranged horizontally and vertically. These directions do lend themselves to the easiest implementation of the finite differencing method used to evaluate partial derivates in the QG omega equation. However, at large enough scales, the placement of a cartesian coordinate system on a spherical surface (e.g. the Earth) is not orthogonal in the horizontal. That is as lines of longitude converge toward the poles, the intersection between latitude and longitude becomes increasingly skewed so that the positive y half of the coordinate system takes a smaller and smaller percentage of the total coordinate system. The difference between the latitude, longitude system and the cartesian coordinate system changes with latitude. Figure 4.1a shows the difference, in blue, between a tangent cartesian coordinate system and longitude at the equator. Figure 4.1b shows a smaller difference between longitude at a higher latitude and a cartesian coordinate system. This effect must be considered when comparing differences in latitude.

A more important effect is the change in orientation of a system through the jet stream. Since the cartesian coordinate system does not change with the orientation of the synoptic system, the cartesian difference between two points will be different than the difference if a natural coordinate system were used. Figure 4.2 shows the difference in position between a natural coordinate system, top, and a cartesian coordinate system, bottom along a curved trough. Values contributing to finite differencing calculations are different. A point at the

124

center of a vorticity maximum that is oriented southeast to northwest may experience a false positive of positive vorticity advection due to finite differencing of points due east and west, north and south that are not in the vorticity maximum. The natural coordinate system should not experience such a difficulty. This issue might be responsible for some of the abnormally high term omega forcing at the base of the trough for the December case study day (Figure 3.30d).
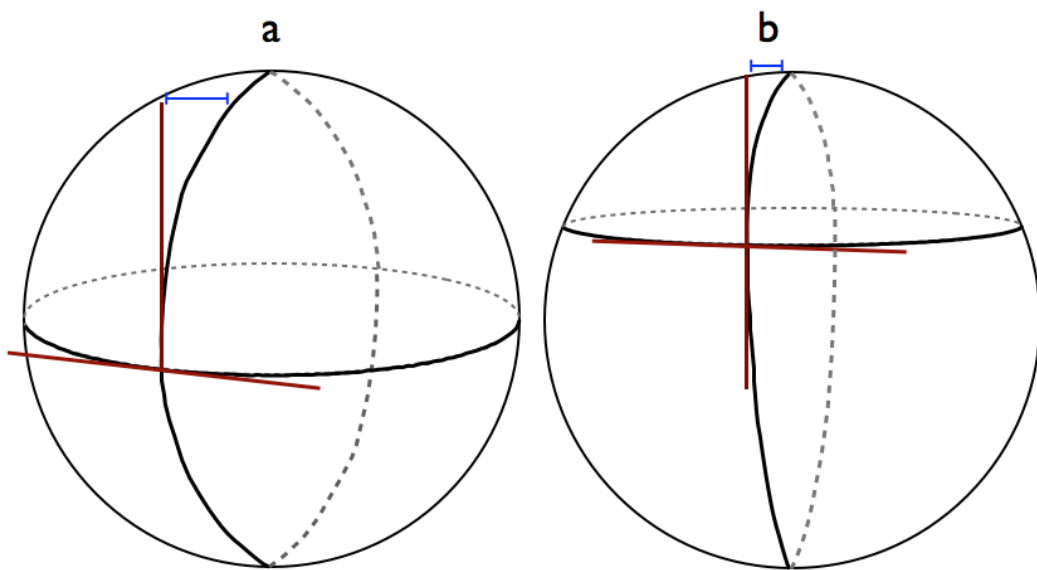
Figure 4.1

Difference, in blue, between orthonormal coordinates and latitude, longitude.

Analysis of the individual dynamic forcing terms of the omega equation agrees with QG theory. Thickness advection is more widespread ahead of the front and contributes to the development of the baroclinic leaf structure. This can be seen on the April case study where there is widespread thickness forcing over the Great Lakes (Figure 3.10e),
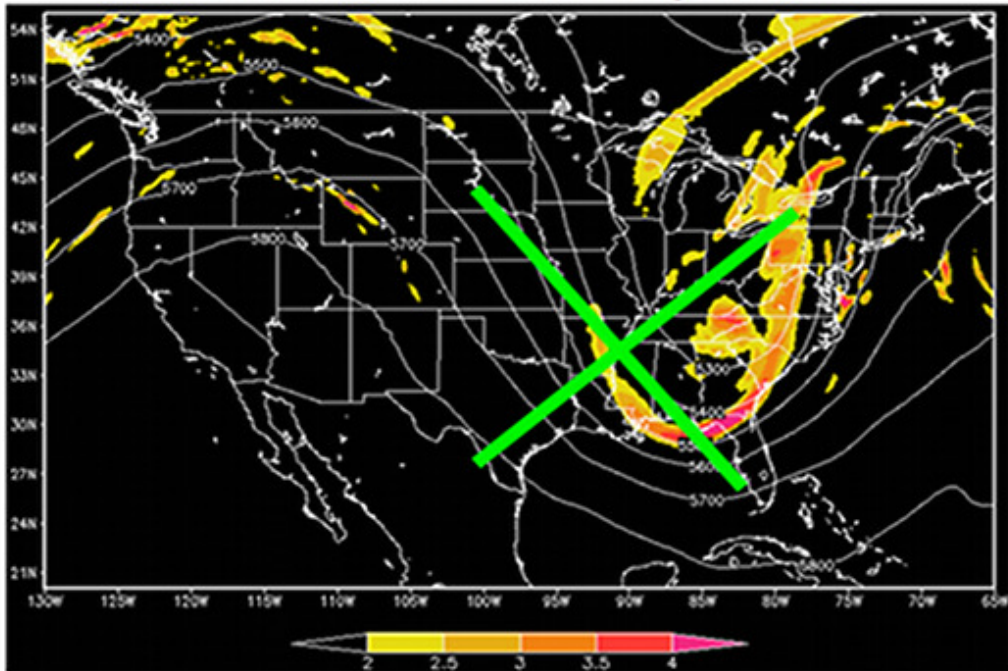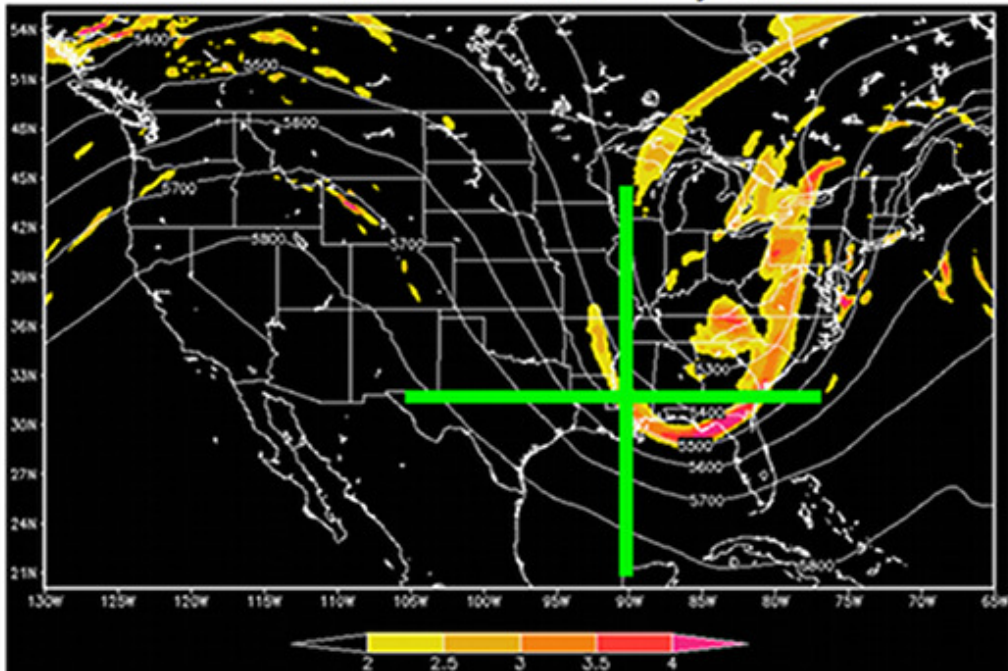
Figure 4.2

Natural coordinate system, top, and a cartesian coordinate system, bottom.

and vorticity forcing is relegated along the front. This is to be expected from a qualitative analysis of dynamic forcing. Strong thickness forcing is the result of warm air being advected ahead of an approaching trough. Thickness forcing can occur well ahead of the front and trough and is instigated by the exit of a ridge where return flow begins drawing warm air from the Gulf of Mexico. Vorticity forcing is the result of wind shear, either speed shear or directional shear. Strong shear is generally restricted to areas of stronger winds which usually do not occur well ahead of the trough. Thus, vorticity advection plays a role in dynamic forcing much closer to the jet stream and trough.

It has been established that thickness advection is strongest below 500 hPa while vorticity advection is strongest above 500 hPa. This is corroborated by term omega forcing. Term omega calculated with sigma for the December case study day (Figure 3.30a) shows the strongest low level vertical velocities towards the north, near the baroclinic leaf. The thickness advection term shows the largest areas of thickness advection (Figure 3.30e) also to the north. As term omega with sigma is based out of the boundary layer, those dynamic forcings occur below 500 hPa.

4.4   Three-dimensional Visualizations

Three-dimensional visualization is limited in its representation on a static 2D surface. The volume cannot be actively rotated, zoomed, or panned. This greatly reduces the ability of the viewer to perceive the model domain as a 3D volume. Also, only one view may be chosen to be displayed at a time on a static 2D surface. For the present study, a viewpoint normal to the Earth's surface and centered over the domain was used, but with realtime 3D

127

rendering any viewpoint may be chosen for optimal comparison of variables or to resolve small changes in a variable field.

As a consequence of the orientation chosen to view the 3D volume, the perspective of images of the same variable can be skewed when viewed from a 2D surface and a 3D view rendered as a 2D surface. Upward dynamic forcing is placed incorrectly in the term omega 3D view for the March case study day (Figure 3.7d) when compared to observations, but the 2D view (Figure 3.6d-f) displaces the forcing so that the term omega forcing lines up with the precipitation and cloud cover. One possible explanation for this is the angle at which the 3D view is shown.

4.5   Model Omega

It was shown that for each case study day model omega discretizes larger dynamically forced vertical motion across individual mountains and mountain ranges. This produces a difficult to read, noisy vertical motion field, particularly over the interior Rocky Mountains. Term omega does not show the discrete mountain forcing as geography is not programed into the finite differencing model, thus term omega provides dynamical smoothing for the vertical velocity field.

Thermodynamically driven days are handled poorly by term omega both with and without sigma. Model omega also performs poorly in the placement of individual storms or storm complexes (Figure 3.20c, Figure 3.24c); however, the coverage of thunderstorm activity is more realistic with model omega. Term omega without sigma shows little coverage, and term omega with sigma greatly overdoes thunderstorm coverage.

4.6 Correlations

For all case study days and at all levels term omega calculated without sigma was more highly correlated to model omega than was term omega calculated with sigma. In most cases term omega without sigma was one or more orders of magnitude more strongly correlated than term omega with sigma.

In general, the summer months expressed the weakest correlations, and this is to be expected. Term omega is driven by synoptic scale dynamic forcing, but the primary forcing feature during the summer is thermodynamic forcing caused by mesoscale features.

Term omega with sigma correlations are low but lowest when correlating the entire column. This might be a result of the inclusion of the boundary layer in finding column correlations. As sigma is influenced by the change in logarithmic potential temperature with height, and potential temperature changes little within the boundary layer, sigma is small. As sigma is small in the boundary layer, term omega forcing becomes large and broadens the base of the normally distributed values.

It was found, as was posited by Trenberth [50], that vorticity advection forcing and thickness advection forcing are not independent of one another. Correlations between terms B and C of the omega equation were found to be highly negative with values of up to -0.75. This occurs because terms B and C have common canceling components in the differentiating of geopotential height. Though the result of the differentiations are used differently within each term, the reliance on the geopotential height field induces a connection between terms.

4.7   Applications

The techniques developed to visualize QG omega can be extended to view other meteorological variables. Analogs can be developed from each 2D forecasting technique to a related 3D technique with each map yielding new 3D forecasting tools and indices. Three-dimensional visualization can be applied to many other forecasting issues. For example, plotting two-meter temperature shows horizontal temperature changes, but several maps must be viewed to locate vertical temperature changes. By only looking at individual levels in the atmosphere, important changes could be overlooked, such as a weakness in an inversion. Three-dimensional visualization could display upward or downward vertical velocities within a storm, isentropic upglide, or a multitude of other parameters.

The main application is two fold: one, the calculation of each term of the QG omega equation allows for direct comparison between vorticity advection and thickness advection. The separate terms of the omega equation, differential vorticity advection and thickness advection, interact and can cancel one another, thus the individual terms must be compared contemporaneously during qualitative visual analysis.

The second application is the ability to present a comprehensive view of synoptic scale forcings with 3D visual analysis. As current visual analysis using QG theory can be quite time consuming, 3D visualization provides a faster visualization method. Additionally, 3D visualization allows the viewer to see all levels of the atmosphere instead of having to pick and choose from the mandatory levels.

CHAPTER 5

CONCLUSIONS

Due to the difficulty in measuring vertical motion, quasi-geostrophic theory has been used for a century to diagnose and forecast atmospheric vertical winds from the height, pressure, temperature, and moisture fields. One of the fundamental equations used is the QG omega equation. Qualitatively, it states that positive differential vorticity advection and warm air advection lead to rising air. However, there is a complex interplay between these two terms, and there can be considerable cancelation. A case by case comparison of these two terms is necessary to reliably diagnose the atmosphere. Unfortunately, two problems exist when attempting to compare the two terms. First, there are no sources of model data which show the individual terms of QG omega. Secondly, model calculated QG omega is very noisy and difficult to interpret. The calculation of QG omega on the analysis fields of the NAM can solve both problems.

To achieve a reliable method of comparing the vorticity forcing term and the thickness forcing term, the Quasi-geostrophic omega equation has been calculated though finite differencing techniques using analysis fields from the NAM. With these calculations, the individual vorticity advection forcing, thickness advection forcing, and total forcing are separated for individual diagnoses and can be compared to one another to qualitatively assess the strength of each component. These fields are then visualized three-dimensionally

131

to display data in a more coherent, unified way. With 3D visualization, the QG variables can be viewed at any level or layer desired, thus helping remove some assumptions when applying QG theory in two dimensions.

5.1   Findings

Eight case studies, two from each season, are analyzed viewing both model omega and calculated term omega. It was found that term omega and model omega are somewhat correlated and that the strongest correlations occur when static stability is not considered. When static stability is not incorporated into the calculation of term omega, the smoothing technique removed noisy and convoluted vertical forcing visualizations and replaced them with connected, continuous areas of vertical forcing that are easier to interpret. Unfortunately, such a smoothing technique utilizing the omega equation itself will only work on occasions where vertical forcing is dynamically driven, as in the cooler season months. For the summer case study days, the technique handled vertical motion poorly, as thermodynamic forcing is the primary forcer.

Term omega was effective in discriminating between differing types of dynamic forcing such as vorticity advection and thickness advection. Additionally, term omega compensates when one term acts to counter another term, only showing areas of overall forcing. As term omega relies on QG theory, it demonstrates many of the principles used in QG forecasting. Thickness advection is strongest below 500 hPa ahead of fronts and aids in development of the baroclinic leaf. Vorticity advection is strongest above 500 hPa through the trough and along the jet stream.

Three-dimensional visualization aided in the interpretation of the vertical motion fields. Viewing the atmosphere in three dimensions reduces the number of different levels required to diagnose the atmosphere and can remove assumptions inherent in 2D analysis. For example, as the level of non-divergence is not a continuous entity, the requirement that vorticity only be viewed on the 500 hPa level need not be followed. Thusly, vorticity, its advection, and the forcing caused by it can be viewed three-dimensionally, showing areas of forcing throughout the troposphere.

5.2   Future Research

Several issues require future investigation and most issues relate to either visualization techniques, verification methods, or development of the QG system of equations.

1.) Geopotential tendency is not studied here as there is no reliable source of data to compare calculated values from the QG geopotential tendency equation (appendix A shows a sample of calculated results using the QG geopotential tendency equation). Further research would involve developing a geopotential tendency dataset from observations and model data to compare to calculated values of geopotential tendency to determine the usefulness of a geopotential tendency index.

2.) The visualization methods in this study were limited to various methods of contouring. Many other 3D visualization methods exist, such as volume rendering, stream tracers, and glyphs. Any of these methods could show additional information not shown by simple contouring.

3.) A topic of continued inquiry is the improvement of verification methods for calculated term omega. As the NAM itself runs the same equations as the indices described here, a more independent and observationally true method of verification needs to be pursued. Though implementation would be difficult, various observations could be used in the verification of term omega. Satellite or radar imagery could be quantified to connect the coldest cloud tops or highest dBz value to the strongest upward vertical motion. Sounding data could be used, but only with large errors as the horizontal wind is more easily measured than the vertical. Microwave or other types of sounders could be used, but they only provide point references. Another possible implementation of radar data is to use the higher tilts of velocity data from WSR-88D radars and calculate vertical and horizontal velocity vector components to give values for vertical motion. A large problem with velocity data is that there is no way to differentiate between upward vertical velocities and downward vertical velocities.

4.) Despite the improvement of term omega calculations over model omega, the comparison must also be made between term omega and a simple Gaussian smoothing function that could be applied to each domain point. Such a smoothing function would require far less computational resources and could be performed much faster than the calculation of forcing from model omega.

5.) Term omega is only forcing caused by dynamic instigators; as such, term omega does not describe actual vertical motion, only the strength and direction of forcing. To fully solve the QG omega equation, the right-hand-side operators involved with omega must be inverted. This involves the use of spherical harmonics [53],[35], which is outside the

scope of this study. Improved calculation methods should also be implemented. Though it greatly increases calculation time, third-order and higher finite differencing [5] could be used instead of the presently used first and second order differencing methods. This would reduce round-off error imposed by the wider differencing methodology.

5.3 Merit and importance

Not just operational forecasters stand to see the benefits of improving forecasting techniques. Of importance to the general public is the possible economic benefit of improved forecasting indices. Thompson [48] found the economic benefit of operational research at 5-10% improvement of weather-related economic losses. Given the billions of dollars that are lost from the GNP annually as a function of weather-related events, the impact of improved, standardized forecasts could be measurable in millions of dollars.

Also of importance is the timeliness and precision of forecasts. Root [39] found that forecasters tend to be overconfident in forecasts. A standardized method of finding total vertical forcing and its separate components reduces forecaster subjectivity. Quantitative, standardized, and objective tools allow forecasters to determine the most probable areas of vertical motion so that effort and time can be applied to developing a forecast as opposed to locating areas of development.

It has been shown, with eight case studies, that a vertical forcing quantification technique using the QG omega equation can provide for data smoothing without great loss of data resolution. The technique also quantifies the individual components of the QG omega equation which have been shown to be highly negatively correlated. This tech-

nique will allow for a faster, less subjective diagnosis routine for operational forecasters. The ultimate goal is the development of a new, singular QG forcing index. Such an index would incorporate vorticity advection forcing, thickness advection forcing, the geopotential tendency equation, and thermodynamics (including isentropic analysis and diabatic processes). Once this index is developed, the total forcing for the atmospheric column can be described layer by layer such that the exact position and strength of forcing can be quantitatively analyzed.

REFERENCES

[1] D. K. Arthur, S. Lasher-Trapp, A. Abdel-Haleem, N. Klosterman, and D. S. Ebert, "A New Three-Dimensional Visualization System for Combining Aircraft and Radar Data and Its Application to RICO Observations," *Journal of Atmospheric and Oceanic Technology*, vol. 27, no. 5, May 2010, pp. 811–828.

[2] D. B. Barjenbruch, E. Thaler, and E. J. Szoke, "Operational Applications of Three Dimensional Air Parcel Trajectories Using AWIPS D3D," *18th International Conference on IIPS Interactive Symposium on AWIPS*. 2002, p. J5.5, American Meteorological Society.

[3] S. L. Barnes, "On the Accuracy of Omega Diagnostic Computations," *Monthly Weather Review*, vol. 114, no. 9, 1986, pp. 1664–1680.

[4] A. F. Bennett and P. E. Kloeden, "The quasi-geostrophic equations: Approximation, predictability and equilibrium spectra of solutions," *Quarterly Journal of the Royal Meteorological Society*, vol. 107, no. 451, July 1981, pp. 121–136.

[5] K. A. Campana, "Higher Order Finite-Differencing Experiments with a Semi-Implicit Model at the National Meteorological Center," *Monthly Weather Review*, vol. 107, no. 4, 1979, pp. 363–376.

[6] T. Carlson, *Mid-latitude Weather Systems*, Harper Collins Academic, 1991.

[7] R. B. Cattell, " The Scree Test for the Number of Factors," *Multivariate Behavioral Research*, vol. 1, no. 2, 1966, pp. 245–276.

[8] H.-R. Chang and H. N. Shirer, "Compact Spatial Differencing Techniques in Numerical Modeling," *Monthly Weather Review*, vol. 113, no. 4, 1985, pp. 409–423.

[9] J. Charney, "The Use of the Primitive Equations of Motion in Numerical Prediction," *Tellus*, vol. 7, no. 1, Feb. 1955, pp. 22–26.

[10] J. Charney and J. von Neumann, "Numerical Integration of the Barotropic Vorticity Equation," *Tellus*, vol. 2, no. 4, 1950.

[11] J. G. Charney, "The Dynamics of Long Waves in a Baroclinic Westerly Current," *Journal of Meteorology*, vol. 4, no. 5, 1947.

[12] J. G. Charney, "On the Scale of Atmospheric Motions," *Geof. Publ. (Oslo)*, vol. 17, no. 2, 1948, pp. 3–17.

[13] J. G. Charney and M. E. Stern, "On the Stability of Internal Baroclinic Jets in a Rotating Atmosphere," *Journal of the Atmospheric Sciences*, vol. 19, 1962, pp. 159–172.

[14] G. P. Cressman, "A Diagnostic Study of Mid-Tropospheric Development," *Monthly Weather Review*, vol. 89, no. 3, Mar. 1961, pp. 74–82.

[15] D. R. Durran and L. W. Snellman, "The Diagnosis of Synoptic-Scale Vertical Motion in an Operational Environment," *Weather and Forecasting*, vol. 2, 1987.

[16] J. L. Dyer and E. P. Amburn, "Desktop visualization of meteorological data using ParaView," *Kitware Source*, vol. 14, 2010, pp. 7–10.

[17] B. E. T. Eady, "Long Waves and Cyclone Waves," *Tellus*, vol. 1, no. 3, 1949, pp. 33–52.

[18] A. Eliassen, "Geostrophy," *Quarterly Journal of the Royal Meteorological Society*, vol. 110, no. 463, Mar. 1984, pp. 1–12.

[19] U. C. for Atmospheric Research, "Image Archive, Meteorological case study selection kit," February 2012.

[20] T. Geyer, Nicholas; Konor, Celal; Cram, "Visualization and Model Intercomparisons of the Vector Vorticity Model," 2011.

[21] J. Holton, *An Introduction to Dynamic Meteorology*, 3 edition, Academic Press, 1992.

[22] B. Hoskins, M. Pedder, and D. W. Jones, "The omega equation and potential vorticity," *Quarterly Journal of the Royal Meteorological Society*, vol. 129, no. 595, Oct. 2003, pp. 3277–3303.

[23] B. J. Hoskins, "Sutcliffe and his development theory," *The life cycles of extratropical cyclones*, M. A. Shapiro and S. Gronas, eds., American Meteorological Society, Boston, MA, 1975, pp. 81–86.

[24] B. J. Hoskins, I. Draghici, and H. C. Davies, "A new look at the ω-equation," *Quarterly Journal of the Royal Meteorological Society*, vol. 104, no. 439, Jan. 1978, pp. 31–38.

[25] B. J. Hoskins, M. E. McIntyre, and A. W. Robertson, "On the use and significance of isentropic potential vorticity maps," *Quarterly Journal of the Royal Meteorological Society*, vol. 111, no. 470, 1985, pp. 877–946.

[26] B. J. Hoskins and M. A. Pedder, "The diagnosis of middle latitude synoptic development," *Quarterly Journal of the Royal Meteorological Society*, vol. 106, no. 450, Oct. 1980, pp. 707–719.

[27] J. C. Jusen and R. Atlas, "Diagnostic Evaluation of Numerical Model Simulations Using the Tendency Equation," *Monthly Weather Review*, vol. 119, no. 12, 1991, pp. 2936–2955.

[28] Kitware, "Advantages of Paraview," January 2012.

[29] S. A. A. Kulie, Mark S. and R. Bennartz, "Utilizing UNIDATA's Integrated Data Viewer as an undergraduate meteorology classroom tool," *17th Symposium on Education, 24th Conference on IIPS*. 2008, American Meteorological Society.

[30] O. A. M., "Adiabatic invariants of atmospheric processes," *Meteorologiya i gidrologiya*, vol. 2, 1964, pp. 3–9.

[31] D. J. Muraki, C. Snyder, and R. Rotunno, "The Next-Order Corrections to Quasi-geostrophic Theory," *Journal of the Atmospheric Sciences*, vol. 56, no. 11, June 1999, pp. 1547–1560.

[32] E. A. O'Lenic and R. E. Livezey, "Practical Considerations in the Use of Rotated Principal Component Analysis (RPCA)in Diagnostic Studies of Upper-Air Height Fields," *Monthly Weather Review*, vol. 116, no. 8, 1988, pp. 1682–1689.

[33] J. Pedlosky, "The Stability of Currents in the Atmospehre and the Ocean: Part I," *Journal of the Atmospheric Sciences*, vol. 21, 1964, pp. 201–219.

[34] N. A. Phillips, " Geostrophic Motion," *Reviews of Geophysic*, vol. 1, 1963, pp. 123–176.

[35] J. Raisanen, "Height Tendency Diagnostics Using a Generalized Omega Equation, the Vorticity Equation, and a Nonlinear Balance Equation," *Monthly Weather Review*, vol. 125, no. 7, 1997, pp. 1577–1597.

[36] R. J. Reed and F. Sanders, "An investigation of the development of a mid-tropospheric frontal zone and its associated vorticity field," *Journal of Meteorology*, vol. 10, no. 10, 1953, pp. 338–349.

[37] C. Rogers and J. Mchugh, "On the separability of the North Atlantic oscillation and Arctic oscillation," *Climate Dynamics*, 2002, pp. 599–608.

[38] J. C. Rogers, "Patterns of Low-Frequency Monthly Sea Level Pressure Variability (1899-1986) and Associated Wave Cyclone Frequencies," *Journal of Climate*, vol. 3, no. 12, 1990, pp. 1364–1379.

[39] H. E. Root, "Probability Statements in Weather Forecasting," *Journal of Applied Meteorology*, vol. 1, no. 2, June 1962, pp. 163–168.

[40] C. G. Rossby, "Relation between variations in the intensity of the zonal circulation of the atmosphere and the displacements of the semi-permanent centers of action," *Journal of Marine Research*, vol. 2, no. 1, 1939, pp. 38–55.

[41] C. G. Rossby, "Planetary Flow Patterns in the Atmosphere," *Quarterly Journal of the Royal Meteorological Society*, vol. 66, 1940, pp. 68–87.

[42] P. L. Spencer, D. J. Stensrud, and J. M. Fritsch, "A Method for Improved Analyses of Scalars and Their Derivatives," *Monthly Weather Review*, vol. 131, no. 3, 2003, pp. 2555–2576.

[43] W. J. Steenburgh and J. R. Holton, "On the Interpretation of Geopotential Height Tendency Equations," *Monthly Weather Review*, vol. 121, no. 9, 1993, pp. 2642–2645.

[44] R. B. Stull, "Static stability-An update.," *Bulletin of the American Meteorological Society*, vol. 72, no. 10, 1991, pp. 1521–1529.

[45] R. C. Sutcliffe, "Cyclonic and Anticyclonic Development," *Quarterly Journal of the Royal Meteorological Society*, vol. 65, no. 282, 1939, pp. 518–524.

[46] R. C. Sutcliffe, "A contribution to the problem of development," *Quarterly Journal of the Royal Meteorological Society*, vol. 73, 1947, pp. 370–383.

[47] R. C. Sutcliffe and a. G. Forsdyke, "The theory and use of upper air thickness patterns in forecasting," *Quarterly Journal of the Royal Meteorological Society*, vol. 76, no. 328, Apr. 1950, pp. 189–217.

[48] J. Thompson, "Economic Gains from Scientific Advances and Operational Improvements in Meteorological Prediction," *Journal of Applied Meteorology*, vol. 1, no. 1, Mar. 1962, pp. 13–17.

[49] L. A. Treinish, "Interactive, Web-based Three-Dimensional Visualizations of Operational Mesoscale Weather Models," *Proceedings of the IEEE*, 1999.

[50] K. E. Trenberth, "On the Interpretation of the Diagnostic Quasi-Geostropic Omega Equation.pdf," *Monthly Weather Review*, vol. 106, 1978.

[51] L. W. Uccellini and P. J. Kocin, "The Interaction of Jet Streak Circulations during Heavy Snow Events along the East Coast of the United States," *Weather and Forecasting*, vol. 2, no. 12, 1987, pp. 289–308.

[52] A. Viudez and L. Haney, Robert, "On the Shear and Curvature Vorticity Equations," *Journal of the Atmospheric Sciences*, vol. 53, no. 22, 1996, pp. 3384–3394.

[53] a. Wiin-Nielsen, "On the motion of various vertical modes of transient, very long waves: Part I. Beta Plane Approximation," *Tellus*, vol. 23, no. 1, Feb. 1971, pp. 87–98.

[54] M. Wiin-Nielsen, a., Drake, "The Contribution of divergent wind components to the energy exchange between the baroclinic and barotropic components," *Monthly Weather Review*, vol. 94, no. 1, 1966, pp. 1–8.

[55] M. Wiin-Nielsen, a., Drake, "NOAA/National Model Archive and Distribution System," October 2011.

[56] H. Zhang, P. Shu, Y. Liu, and Y. Li, "Some Techniques for Three-dimensional Doppler Weather Radar Data Processing," *International Conference on Geoscience and Remote Sensing Symposium*, Denver, CO, USA, 2006, pp. 2884 – 2887, IEEE.

[57] S. Ziegeler, R. J. Moorhead, P. J. Croft, and D. Lu, "The MetVR Case Study : Meteorological Visualization in an Immersive Virtual Environment Categories and Subject Descriptors," *IEEE Symposium on Information Visualization*, 2001, pp. 1–5.

APPENDIX A A

GEOPOTENTIAL TENDENCY

As there is no direct comparison for geopotential tendency in model data, the evaluated geopotential tendency equation was not used in the case studies in this study. Images with geopotential tendency are only presented here for reference (Figure A.1, Figure A.2, Figure A.3). Two images for each case study are shown; one is of contoured 3D geopotential tendency colored by pressure. The second image is of the 500 hPa pressure level colored by geopotential tendency.

Figure A.1 shows geopotential tendency for January 2, 2012, March 7, 2011, and April 4, 2011: Panel a.) Contoured geopotential tendency for January 2, 2012 at 8.0×10^{-8}. Panel b.) Contoured geopotential tendency for March 7, 2011 at 9.0×10^{-8}. Panel c.) Contoured geopotential tendency for April 4, 2011 at 1.2×10^{-7}. Panel d.) 500 hPa pressure level shaded by geopotential tendency at 4.0×10^{-7} to -4.0×10^{-7} for January 2, 2012. Panel e.) 500 hPa pressure level shaded by geopotential tendency at 4.2×10^{-7} to -4.2×10^{-7} for March 7, 2011. Panel f.) 500 hPa pressure level shaded by geopotential tendency at 5.0×10^{-7} to -5.0×10^{-7} for April 4, 2011. Figure A.2 shows geopotential tendency for May 12, 2011, July 17, 2011, and August 21, 2011: Panel a.) Contoured geopotential tendency for May 12, 2011 at 1.0×10^{-7}. Panel b.) Contoured geopotential tendency for July 17, 2011 at 8.0×10^{-8}. Panel c.) Contoured geopotential tendency for August 21, 2011 at 1.0×10^{-7}. Panel d.) 500 hPa pressure level shaded by geopotential tendency at 2.0×10^{-7} to -2.0×10^{-7} for May 12, 2011. Panel e.) 500 hPa pressure level shaded by geopotential tendency at 2.8×10^{-7} to -2.8×10^{-7} for July 17, 2011. Panel f.) 500 hPa pressure level shaded by geopotential tendency at 1.8×10^{-7} to -1.8×10^{-7} for August 21, 2011. Figure A.3 shows geopotential tendency for October 5, 2011 and

December 12, 2010: Panel a.) Contoured geopotential tendency for October 5, 2011 at 1.0×10^{-0}. Panel b.) Contoured geopotential tendency for December 12, 2010 at 1.0×10^{-6}. Panel c.) 500 hPa pressure level shaded by geopotential tendency at 6.0×10^{-7} to -6.0×10^{-7} for October 5, 2011. Panel d.) 500 hPa pressure level shaded by geopotential tendency at 6.0×10^{-7} to -6.0×10^{-7} for December 12, 2010.
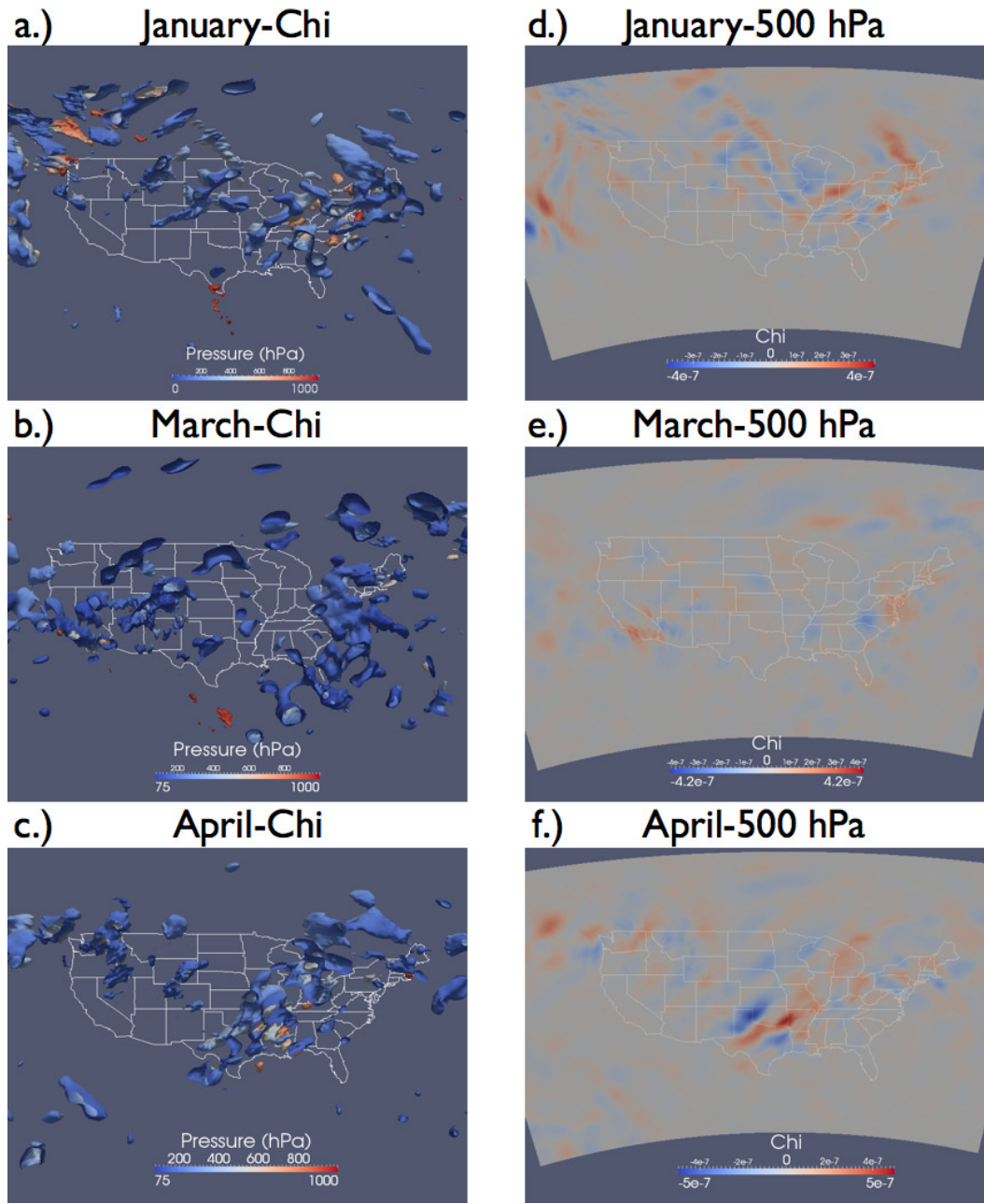
Figure A.1

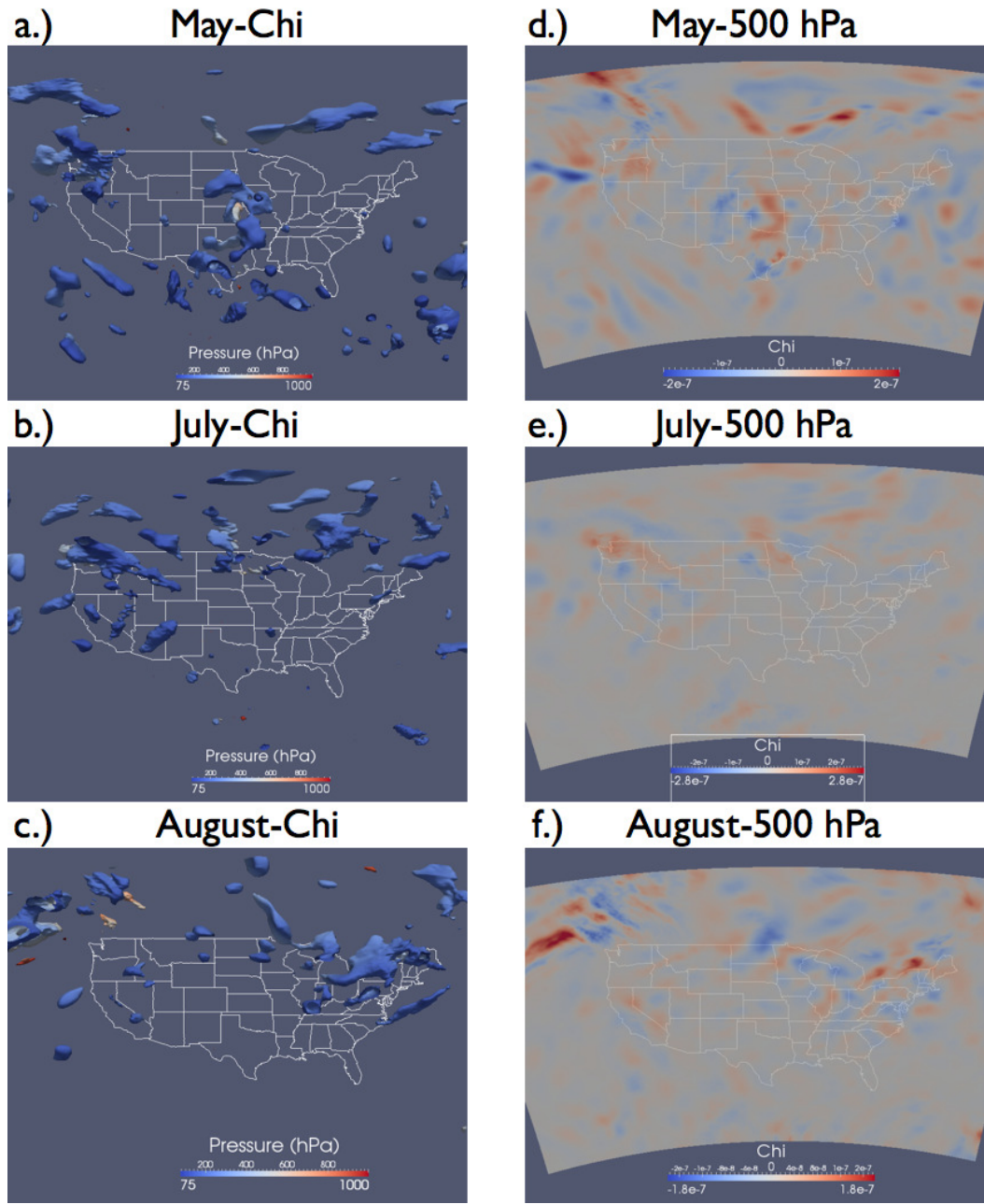Geopotential tendency for Jan. 2, 2012, Mar. 7, 2011, Apr. 4, 2011

Figure A.2

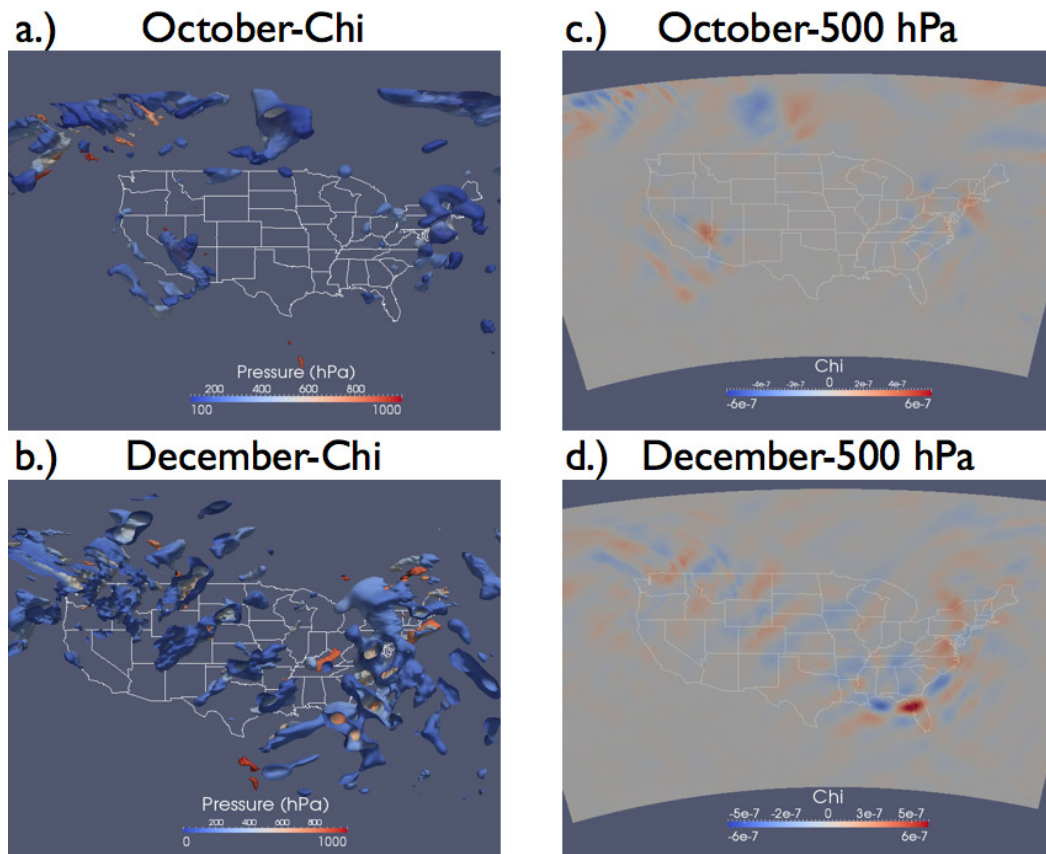Geopotential tendency for May 12, 2011, Jul. 17, 2011, Aug. 21, 2011

Figure A.3

Geopotential tendency for Oct. 5, 2011, Dec. 12, 2010